MASTER THESIS

Erasmus Mundus Master in Advanced Material Sciences and Engineering (AMASE)

STATISTICAL SIMULATION OF NANOINDENTATION ON HARDMETALS

Report and Annexes

Author: Gonzalo Zuviría María
Director: Dr. Emilio Jiménez Piqué
Co-Director: Dr. Ferhun Caner
Delivery: June 2021

Abstract

Hardmetals combine high hardness and wear resistance with fair fracture toughness and fatigue resistance. Such a unique combination has made this material ubiquitous in tooling and other applications where demanding tribological properties are required. However, the microstructural aspects that give rise to these properties are complex and have not been adapted for modelling in engineering software with precision. Therefore, the main purpose of this master thesis is to join experimentation and numerical modelling.

A typical test used for studying the mechanical properties of hardmetals is nanoindentation, as it allows to measure at the nanometric scale. The objective of this work is to simulate nanoindentation in a commercial software (ABAQUS) that solves Multiphysics problems through the Finite Element Method (FEM). Moreover, the sample under study is a real portion of a hardmetal microstructure attained with a Focused Ion Beam (FIB) tomography. This aspect is actually novel because traditional approaches use artificial microstructures.

The model was successfully developed and its results agree with experimental results. Three different material models for the binder phase were tested and the compared. In addition, a stiffening effect related to boundary constraints was found. Such effect has discouraged some modelling strategies found in literature regarding their application to model the reinforcing phase.

UNIVERSITAT POLITÈCNICA DE CATALUNYA
BARCELONATECH
Escola d'Enginyeria de Barcelona Est

Resumen

El metal duro es un material que combina alta dureza y resistencia al desgaste con buena tenacidad a la fractura y resistencia a la fatiga. Esta combinación única ha hecho que este material sea esencial en herramientas de corte y otras aplicaciones donde se requieran excelentes propiedades tribólogicas. Sin embargo, las características microestructurales que dan lugar a estas propiedades son complejas y no han sido aún adaptadas para su correcto modelado en softwares de diseño. Por tanto, el objetivo principal del presente trabajo final de maestría es unir la experimentación con el modelado numérico.

Un ensayo típico para el estudio de las propiedades mecánicas del metal duro es la nanoindentación, pues permite la medición a escala nanométrica. Luego, este estudio es simulado en un software comercial (ABAQUS) que resuelve problemas físicos a través del método de elementos finitos (FEM, por sus siglas en inglés). Además, la muestra de estudio será una porción de una microestructura real, la cual fue obtenida previamente a través de tomografía por haz de iones (FIB). Este aspecto es especialmente novedoso, ya que normalmente se usan microestructuras artificiales.

El modelo numérico fue desarrollado con éxito y los resultados obtenidos se ajustan razonablemente bien con los datos experimentales hallados en bibliografía. Por otro lado, se probaron y contrastaron entre sí tres modelos de plasticidad distintos para la fase ligante. También se encontró un incremento en la rigidez producido por la proximidad de las condiciones de contorno, lo cual desalienta el uso de algunas estrategias de modelado halladas en literatura que aplican dichas condiciones para simular el efecto del material de refuerzo sobre la matriz metálica.

UNIVERSITAT POLITÈCNICA DE CATALUNYA
BARCELONATECH
Escola d'Enginyeria de Barcelona Est

Resum

El metall dur és un material que combina alta duresa i resistència al desgast amb bona tenacitat a la fractura i resistència a la fatiga. Gràcies a aquesta combinació única, que aquest material sigui essencial és en eines de tall i altres aplicacions on es requereixin excel·lents propietats tribològiques . Tot i així, les característiques microestructurals de les quals deriven aquestes propietats són complexes i encara no han sigut adaptades per fer un modelat adequat en software de disseny. Per tant, el principal objectiu del present Treball Final de Màster es unir l'experimentació amb el modelat numèric.

Un assaig típic per estudiar les propietats mecàniques del metall dur és la nanoindentación, ja que permet el mesurament a escala nanomètrica. Així, doncs, aquest estudi es simula en un software comercial (ABAQUS) que resol problemes físics a través del mètode d'elements finits (en anglès, FEM). A més, la mostra de l'estudi és una porció d'una microestructura real que ha estat obtinguda prèviament a través de tomografia per feix de ions (en anglès, FIB). Aquest aspecte és especialment innovador perquè normalment es fan servir microestructures artificials.

Durant el transcurs del treball, el modelat numèric s'ha desenvolupat amb èxit i els resultats obtinguts s'ajusten raonablement bé amb les dades experimentals trobades a la bibliografia. D'altra banda, s'han provat i contrastat entre si tres models de plasticitat diferents per el cobalt. També s'ha identificat un increment de rigidesa produït per la proximitat de les condicions de contorn, la qual cosa desaconsella l'ús d'estratègies de modelat trobades a la literatura, on es fan servir per simular l'efecte del material de reforç sobre la matriu metàl·lica.

UNIVERSITAT POLITÈCNICA DE CATALUNYA
BARCELONA**TECH**
Escola d'Enginyeria de Barcelona Est

Acknowledgements

I would like to use this space to express my gratitude to some of my colleagues and professors that have helped me throughout this project. Pedro Machado deserves a special thanks due to his constant assistance and the fruitful conversations about the numerical model. I am also grateful to Dr. Emilio Jiménez-Piqué and Dr. Ferhun Caner for their guidance and useful advice. My colleagues Laia Ortiz Membrado and Sandra García have supplied me with some experimental data that has been much valuable in order to evaluate the simulation results, therefore I am thankful to them too.

UNIVERSITAT POLITÈCNICA DE CATALUNYA
BARCELONA**TECH**
Escola d'Enginyeria de Barcelona Est

UNIVERSITAT POLITÈCNICA DE CATALUNYA
BARCELONATECH
Escola d'Enginyeria de Barcelona Est

Index

UNIVERSITAT POLITÈCNICA DE CATALUNYA
BARCELONA**TECH**
Escola d'Enginyeria de Barcelona Est

1. Introduction

Hardmetals are an essential material in tooling and tribo-mechanical surfaces, due to their optimal combination of hardness, wear resistance and toughness. However, the fundamental mechanisms behind these properties are complex. Reason for this is the intricated geometry of the reinforcing phase at the microstructural scale, especially when compared to other multiphase materials such as polymer matrix composites. Therefore, gaining better understanding of the microstructural mechanisms involved in the deformation and fracture of hardmetals has been crucial.

Much has been done to analyze the behavior of hardmetals in the microscale. Novel characterization techniques such as nanoindentation and tomography have enabled the study of the microstructural mechanisms in these complex composites. However, there is still a limited connection between this experimental approach and the implementation of the discoveries in numerical models. In particular, the use of the Finite Element Analysis (FEA) would be highly beneficial because it would consider complex geometries as the ones in the microstructural scale of hardmetals. Moreover, there are plenty of commercial software based on the Finite Element Method (FEM), hence making it easier to implement in the industrial world the ultimate results of the integration between the experimental discoveries and the numerical modelling.

These constitutional models applied in a typical environment provided by a software that is already wide-spread would enable the companies to improve their estimations when defining critical product characteristics, such as coating thickness, wear rate, cycles to failure, etc. Some research and development costs could also be spared by reducing trial and error approaches, while improving the quality of the resulting products. Consequently, an overall improvement in the product at lower costs would result in greater competitivity, allowing companies to take greater market shares.

The present master's thesis intends to join the increasing trend of binding the experimental and numerical worlds in the field of hardmetals. In this sense, a numerical model of nanoindentation on a microstructural domain attained by a previously-measured tomography is developed. In order to accomplish this task, the following objectives will be pursued:

- Develop a numerical model of nanoindentation using ABAQUS.

- Test the model to assess the accuracy of the results.

- Apply the model on a portion of real microstructure obtained by tomography.

- Perform a statistical analysis of the results and compare them to experimental data in literature.

UNIVERSITAT POLITÈCNICA DE CATALUNYA
BARCELONA**TECH**
Escola d'Enginyeria de Barcelona Est

2. Literature review

The following chapter is comprised of a review of concepts that are crucial for understanding the present project. It is divided in four sections, each corresponding to a particular theorical aspect. First, a review on hardmetals is given, as it is the ultimate object of study. Second, two relevant characterization techniques that were directly involved in the project are explained. Then, a brief introduction to the finite element method and its historical development is provided. The fourth section gives a general scope of the current state of the art and presents a complex material model that was used at an advanced stage of the project. Lastly, the most novel advances in the simulation of nanoindentation on hardmetals is introduced in the State of the Art.

2.1. Hardmetals: The tungsten carbide and cobalt system

Hardmetals (also called cemented carbides) are composite materials comprised of one or more hard and wear-resistant phases embedded in a metallic matrix. In most cases, the hard phase is tungsten carbide, while the ductile and metallic phase is cobalt and its alloys.[1] This material has a perfect balance between abrasive properties and toughness.

2.1.1. Brief comment on nomenclature

The initial steps into hardmetal bibliography can be quite tricky due to the use of two terms that are completely equivalent: 'hardmetals' and 'cemented carbides'. There is no difference in the concept behind these terms, but their use depends rather on the author's background. This is because in Europe it is more common to call them hardmetals, especially in the German-speaking countries as in that language there is only the term '*Hartmetall*'. On the other hand, 'cemented carbides' is more usual in the USA but also in European English literature.[2]

Misunderstandings may also occur when using the '*cermet*' term. This concept was introduced after the end of World War II by joining the terms *ceramic* and *metal*, thus referring to metal matrix composites (MMCs) in which the reinforcing phase was ceramic. Nevertheless, this term is nowadays reserved for sintered hardmetals containing only face-centered cubic phases (fcc), namely titanium carbide (TiC) or nitride (TiN) with the exclusion of tungsten carbide systems. [2]

2.1.2. History and development

The electrical incandescent lamp was devolped in the 1870s[3] and revolutionized the lighting systems, mainly due to its safety when compared to the artificial lighting used until

UNIVERSITAT POLITÈCNICA DE CATALUNYA
BARCELONA**TECH**
Escola d'Enginyeria de Barcelona Est

then, which consisted of flames obtained by burning fossil fuels, wax, etc. However, the production of these lighting bulbs required the production of tungsten filaments. The drawing of these coils is considerably abrasive, thus demanding proper materials for the drawing dies. During some time, these dies were made out of diamond, but after World War I it became significantly expensive. Given the high economic sanctions that were placed on Germany after the Treaty of Versailles, the use of diamond as drawing dies became prohibitive for the German manufacturers.

As a result, many different groups were attempting to develop new hard materials for tungsten drawing dies. Among these groups was the Auer Society, which was a subsidiary of the company OSRAM. They tried to develop an alternative by seeking to transform the brittle tungsten carbide into a ductile material similarly to tungsten. After many unsuccessful attempts, it was proposed to mix add some iron or nickel powder to the WC powder as it was customary at the time for the production of tungsten. However, the outcomes of these experiments were not conclusive, which motivated the researchers to use cobalt instead. This worked perfectly as it could be used in the construction of drawing dies for coarse tungsten wires. As a result, the invention was patented in 1923 under label DRP 420.689, although it was only enforced in England and the USA.[2]

OSRAM would sell the patent to the Krupp Company in 1926[4] that started a low-volume production of the new material. They decided to commercialize it under the trade name 'WIDIA', which is a conjunction of the words 'wie' and 'Diamant' ('like diamond' in German). This name became famous and is still in use today. In fact, as soon as 1929 it was found that not only were hardmetal properties defined by the properties of the phases that composed it and the degree of carburization, but also that the grain size of the tungsten carbide played an essential role. Therefore, Krupp AG. released a new product labeled as WIDIA H1 that featured these characteristics, i.e. it exhibited a high hardness without having changed its composition.

Despite the initial low production volumes (ten tons per year from 1928 to 1932)[2], many companies were established throughout the world, among which were Plansee Titanit in Austria (founded by Dr. Paul Schwartzkopf in 1930) and Kennametal in the USA (founded by Philip McKenna in 1938), which remain major players within the field up to now. World War II had a huge impact in the hardmetal industry, since this material was used to build projectiles. When the Allied forces occupied Germany after the war, Krupp AG was forced to publish all details of its products (hardmetal compositions, techniques of production, quality control methods, etc.). The document became a popular book on how to produce hardmetals and was used worldwide for almost ten years.

Sandvik began to produce cemented-carbide cutting tools in 1942. As a result of the introduction of chemical vapor deposition, the company revolutionized the machining of materials with continuous chip with its release in 1969 of surface-coated hardmetal inserts.

UNIVERSITAT POLITÈCNICA DE CATALUNYA
BARCELONATECH
Escola d'Enginyeria de Barcelona Est

Nowadays, more than 80% of all turning inserts and about 70% of milling inserts are coated. The newest generation are multi-layer coatings with exactly tailored properties for the respective application (material), including true nanocrystalline layer sequences.[2] A timeline with this and further milestones is shown in Table 1.

A significant current trend in the industry is towards the progressive replacement of cobalt as binder material. Reason for this shift is mainly related to the toxicity problems when WC-Co particles are chronically inhaled, which can produce lung diseases. Besides, although cobalt is quite a relevant component of Earth's crust, it tends to be concentrated at remote locations that are less accessible to the companies that process it, thus resulting in high prices. Consequently, more economic and less toxic alloys such as Fe-Ni and Fe-Cr-Ni alloys are regarded as possible candidates to replace cobalt.[4]

Table 1. Timeline of hardmetal development with industry-related milestones.[2], [5]

1923	WC-Co combination is developed.
1927	Tools with WIDIA-hardmetal are shown to the international public for the first time.
1929	WIDIA H1 with a fine-grained tungsten carbide.
1930	Plansee Titanit is established in Austria.
1932	Introduction of TiC-containing hardmetals with the designation "WIDIA X".
1938	Philip McKenna founds Kennametal in Latrobe, Pennsylvania, USA.
1939	WIDIA H2 was introduced with even finer grains.
1942	Sandvik begins to produce cemented-carbide tools. Coromant trade name is established.
1945	Allied Forces intervene Krupp-WIDIA and forces the company to publish all details of its products.
1969	Sandvik was the first in the world with its surface-coated cemented carbide inserts.
1974-1977	Polycrystalline diamond on WC–based hardmetal.
1981-2015	Functionally graded cemented carbides.
1993	Plansee group now comprises of 24 companies worldwide.
1994	WIDIA was sold to the US Company "Cincinnati Milacron".

UNIVERSITAT POLITÈCNICA DE CATALUNYA
BARCELONA**TECH**
Escola d'Enginyeria de Barcelona Est

2002	The US Company Kennametal Inc. bought WIDIA from Milacron for 188 million Euros.
2005	PMG division: joint venture between the Plansee Group and Mitsubishi Materials Group.
2012 - Present	Hardmetals produced by additive manufacturing

2.1.3.   Microstructure and properties

Hardmetals chemical composition consists mainly of three components: carbon, tungsten and the metallic binder. The latter has traditionally been cobalt due to its superior wettability of the tungsten carbide, comminution characteristics (i.e. its ability to be turned into powder) during milling, higher solubility of WC in cobalt at sintering temperatures, its good adhesion to the carbide and excellent mechanical properties.[6], [7] However, iron and nickel alloys have also been used as binder materials and are likely to become more frequent, due to the toxicity of cobalt[4] and its supply issues that arise from the location of economically exploitable mines.[7]

The reinforcing phase is comprised of a line compound (Dalton intermetallic) with little to no deviation from the 1-1 stoichiometric composition, which is a key difference to other metallic carbides that exist in a wider composition range (Berthollide or Kurnakov intermetallics). However, there is also a secondary carbide with composition WC_2.[4], [6] In both carbides, the tungsten atoms are arranged in a hexagonal unit cell, while the carbon atoms partially occupy the octahedral interstices (see Figure 1 a). The WC grains generate three types of facets: two types of prismatic $\{10\bar{1}0\}$ facets and two basal (0 0 0 1) facets that delimit the flat triangular prism with truncated corners,[6], [8] as shown in Figure 1 b).
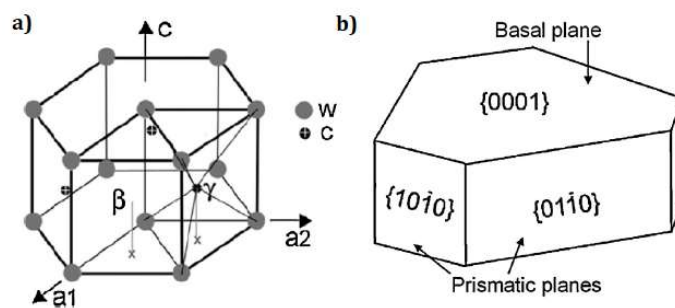

Figure 1. a) Tungsten atoms arranged in a hcp cell with carbon atoms occupying half of the octahedral positions. **b)** Schema of the shape of a WC grain within the cobalt matrix.[9]

Cobalt atoms also arrange themselves in a hexagonal-close-packed unit cell at room temperature. However, it undergoes a phase transition from hcp to fcc structure at 450 °C. Moreover, in the W-C-Co system, there is a significant amount of fcc phase at room temperature,

which is related to the dissolution of both tungsten and carbon in the metallic binder.[6], [10] Cobalt grains tend to be large in size as a result of the sintering process, being able to reach sizes of up to 1 mm.[6] As a consequence, single binder grains generally enclose several WC particle, resulting in a fully interconnected matrix.[5]

Hardmetal green parts are predominantly densified by liquid phase sintering, thus yielding pore-free parts with high fracture resistance. Therefore, both the sintering temperature and the chemical composition must be selected so that there is at least one phase in the solid state. In Figure 2 a vertical section of the W-C-Co phase diagram at 10% w/w Co is shown. Notice that there is a short composition window for the formation of a monocarbide WC without graphite precipitation around 5.5% w/w C. Hence, sintering temperatures are selected between 1300-1500 °C so that the cobalt-rich liquid is present.
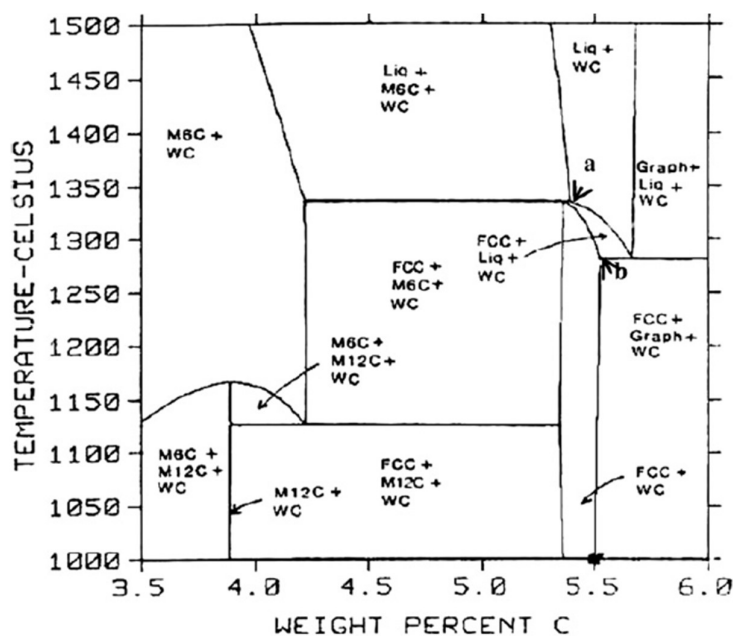

Figure 2. Vertical section of the W-C-Co phase diagram at 10% Co.[4]

Cemented carbides cannot be just described by means of the carbide grain size (d_{WC}) and volumetric fraction of reinforcing phase (V_{WC}), as these values are normally changing together. Then, extra parameters are needed to provide a proper characterization of a particular hardmetal sample: contiguity of the tungsten carbide (C_{WC}) and cobalt mean free path (λ_{Co}). The former accounts for the degree to which a continuous skeleton of the carbide phase exists in the hardmetal piece under study.[6] This parameter is traditionally defined quantitively by the ratio of grain-boundary area to total interface of the carbide grains. The cobalt mean-free path accounts for the spacing between the carbide crystals. Given that there is no well-defined cobalt layer, but a continuous network with changing branches width instead, it is not possible to define a cobalt layer thickness. Both parameters (C_{WC} and λ_{Co}) and can be readily measured on proper

UNIVERSITAT POLITÈCNICA DE CATALUNYA
BARCELONA**TECH**
Escola d'Enginyeria de Barcelona Est

7

micrographies by the typical linear intercept method, although more efficient methods have been recently developed.[11]

As for hardmetals microstructure, it is well accepted that it consists of two intertwined skeletons of the hard tungsten carbide and the softer cobalt binder.[1], [12], [13] A typical micrography of this type of structure is shown in Figure 3, while a 3D tomography reconstruction with skeletonization of the cobalt binder is depicted in Figure 4. Then, the strength of the composite depends on the individual strength of the reinforcement and binder phases, as well as on the properties of the carbide-cobalt and carbide-carbide interfaces.
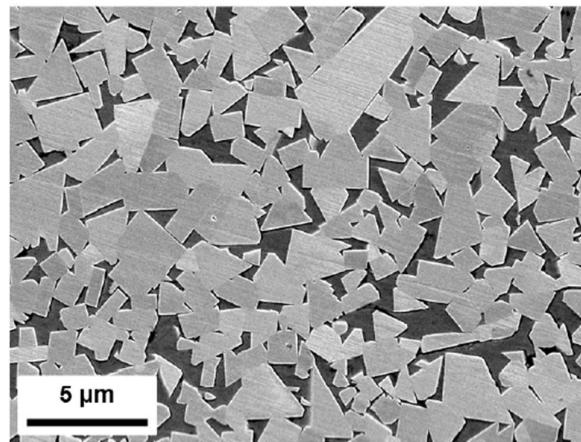

Figure 3. Typical microstructure of a coarse-grained 10% Co hardmetal.[5]
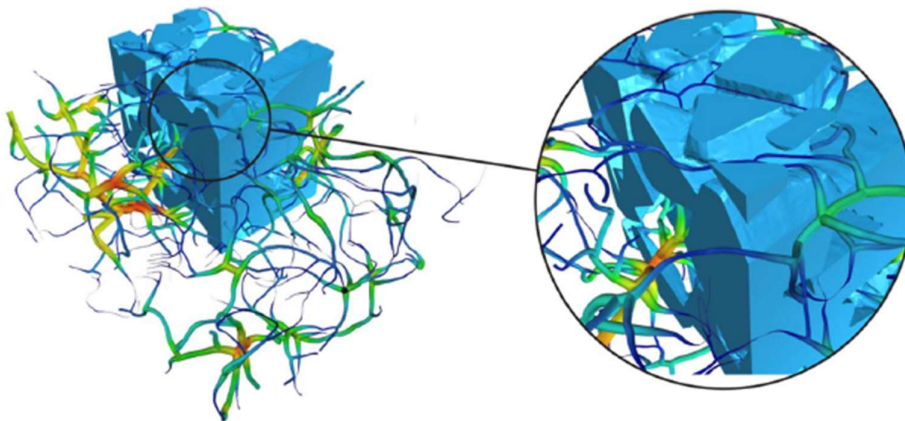

Figure 4. Skeleton of the cobalt binder surrounded by the carbide structure. The different colors are related to the local binder thickness.[14]

The strength of the tungsten carbide skeleton is not only dependent on the chemical composition, but also on the grain size. This was surprisingly learned at the dawn of the development of cemented carbides and has been a major field of development ever since. As a result, carbide grain size in itself is a way of classifying hardmetals as it can be seen in Figure 5.
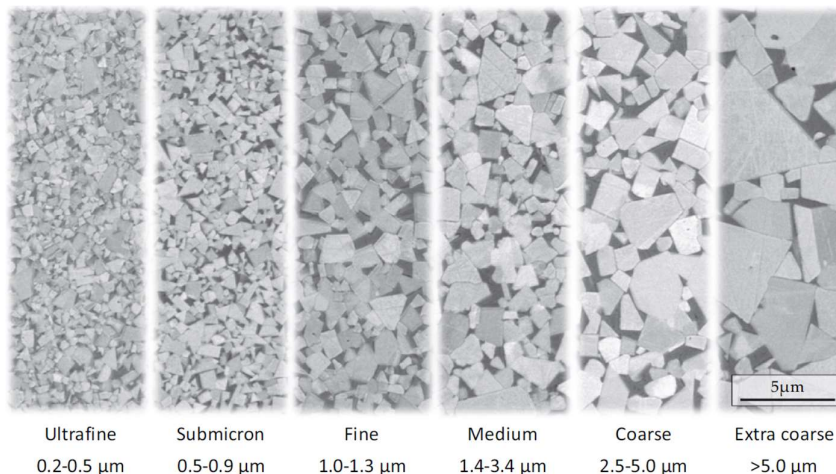
UNIVERSITAT POLITÈCNICA DE CATALUNYA
BARCELONATECH
Escola d'Enginyeria de Barcelona Est

Ultrafine	Submicron	Fine	Medium	Coarse	Extra coarse
0.2-0.5 μm	0.5-0.9 μm	1.0-1.3 μm	1.4-3.4 μm	2.5-5.0 μm	>5.0 μm

Figure 5. Hardmetals classification regarding carbide size.[15]

The increase in strength due to smaller grain size is traditionally referred as Hall-Petch effect, and it can be related to dislocation glide. Grain boundaries act as barriers that hinder dislocation glide, thus producing a dislocation pile-up, which in turn will produce a stress that makes it more difficult for incoming dislocations to keep on approaching. Given that the finer the grain structure the greater is the grain boundary surface, the strain hardening will be much more efficient in a finer microstructure. Nonetheless, grain boundaries in ceramic materials such as WC may also break under load. Consequently, this aspect must be taken into account when using the Hall-Petch model[16]. What is more, the use of finer hardmetal materials implies a substantial reduction in toughness (see Figure 6), hence meaning that a compromise must be found for every application.
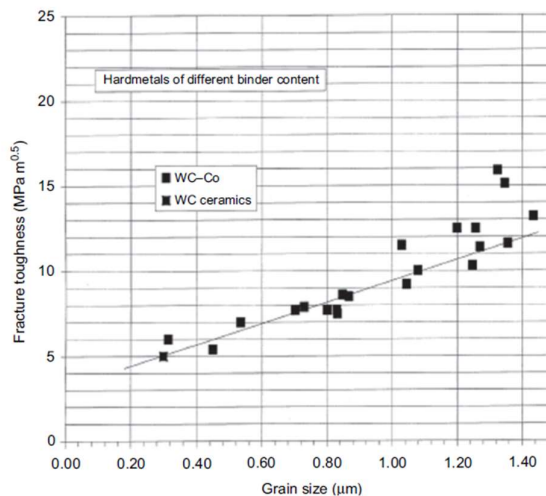

Figure 6. Fracture toughness (K_{IC}) as a function of carbide grain size.[16]
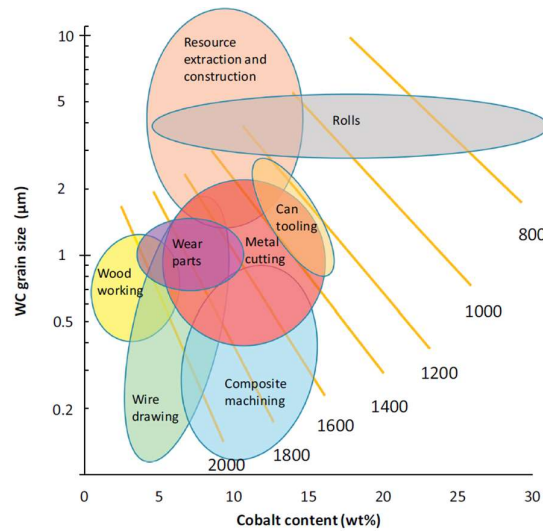
Figure 7. Combination of carbide grain size and cobalt content for different applications.[15]

As regards the strength of the binder, the amount of dissolved tungsten is key to determine the strength and ductility of the cobalt matrix. The degree of tungsten dissolution in the binder is heavily dependent on the carbon content: the lower the carbon content, the higher tungsten content is found in the matrix and vice versa. Moreover, the solubility of tungsten in the cobalt phase is higher in fine-grained hardmetals than in coarse-grained ones.[1] Co-W-C can be heavily work-hardened due to their low stacking-fault energy,[13] meaning that dislocations will tend to split into two Shockley partials with a large stacking fault in between. Dislocation sliding will thus be restricted to a limited number of gliding systems, which favors dislocation pile-up and entanglements. Cross-slip to other crystallographic planes will be limited, as the large stacking fault energy prevents the Friedel-Escaig mechanism from happening.[17] The transformation from hcp to fcc is martensitic in character and is also a relevant strengthening mechanism, although it is not the dominant one.[13]

A major strengthening mechanism of the binder phase is the constraining effect exerted by the tungsten carbide skeleton. It is now accepted that the lesser the cobalt mean free path (λ_{Co}) the greater is the cobalt yield stress. This may be because dislocation glide is stopped at the WC-Co interface, hence giving rise to a dislocation pile up at these boundaries. Researchers have decided to model this behavior by means of an adapted Hall-Petch hardening model that uses the cobalt mean free path instead of the grain size, which was originally used when the model was developed for single-phase metallic crystals.[13] This model is shown in Equation 1, where σ_y^0 is specified as the friction for the displacement of dislocation within the polycrystalline grains.

UNIVERSITAT POLITÈCNICA DE CATALUNYA
BARCELONA**TECH**
Escola d'Enginyeria de Barcelona Est

10

<div align="right">**Equation 1.**</div>

$$\sigma_y = \sigma_y^0 + \frac{k}{\lambda_{Co}^{1/2}}$$

A major issue when modelling the mechanical response of a hardmetal comes from their composite nature, as the stress and strain level estimation and how they partition among the constituent phases are difficult to predict because of the complex phase geometry. Nevertheless, some empirical models such as the one shown in Equation 2 (which is basically a mixture rule but with a factor C that accounts for the shape of carbide skeleton) have been developed to estimate either hardness or yield stress. These models rely on accurate property values of the binder and reinforcement phases, but their measurement is not trivial, since they require precise experiments and a large number of samples that allow hardness or strength value deconvolution.[13] Such a series of tests have been recently performed by Roa et al.,[18]–[20] which has allowed them to find precise values of binder hardness from large nanoindentation testing. In fact, they have developed a Hall-Petch model that relates the hardening effect due to cobalt constraining using λ_{Co},[19] which would allow the use of a model like the one from Equation 2 to make quick estimations.

<div align="right">**Equation 2.**</div>

$$H = H_{WC} \cdot C \cdot V_{WC} + H_{Co} \cdot (1 - C \cdot V_{WC})$$

Last but not least, it is key to highlight that one must be wary when using hardness or strength values obtained from pure component testing for these models. A cobalt alloy with no tungsten carbide may lack of the solute atoms dissolved and their hardening effect. What is more, the absence of the WC skeleton implies that there is no constrainment, which has a significant impact on binder hardness as explained before. The stress distribution may also be different, as the confined matrix is mainly subjected to triaxial loading,[10] hence changing the straining mechanisms that rely on shear stress.

2.2. Related characterization techniques

2.2.1. Nanoindentation

One of the most frequent ways to measure the mechanical properties of thin coatings is through its straining at a small scale. This can be achieved by means of nanoindentation, which consist of an instrumented indenter tip that penetrates the sample surface, while data of load and tip displacement are gathered. Therefore, the load can be plotted as a function of tip displacement, which in turn allows the user to calculate elastic modulus and hardness. An example of the typical result of a nanoindentation experiment is shown in Figure 8. A Berkovich indenter tip

is also depicted, as it is one of the most used indentation probes. This is because it is easier to produce than the Vickers tip, while retaining the same surface-to-depth relationship.
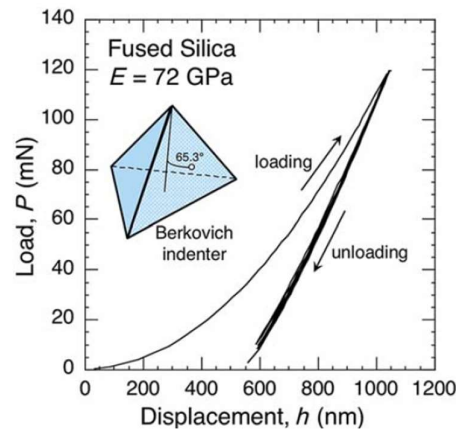

Figure 8. Typical outcome of the nanoindentation procedure: the load-displacement curve.[21]

In the early 1980s, great improvements in wear resistance were achieved by many scientists through ion implantation. The low thickness of this novel surface treatment made it impossible to study it using the surface characterization techniques that were available at the time. Consequently, a small group of scientists working at Brown Boveri Company (Switzerland) started to develop a new technique that could measure superficial properties without substrate influence. The resulting equipment consisted of a cabinet for vibration isolation, an x-y-z table, and an indentation or measurement head, which was controlled with a computer.[21] As this equipment can penetrate from a few nanometers to a few micrometers in depth, the technique was called *nanoindentation*. In 1992, G.M. Pharr, who was involved in the creation of the nanoindenter, joined W.C. Oliver to develop a procedure to obtain both the elastic modulus and hardness from load-displacement data[22], which has actually become the standard among the users of this technique.

In the early days of the method, its main field of application was in the study of thin films, especially among the semiconductor researchers. However, scientists working in many different fields have made good use of the nanoindentation technique and its principles since then. For example, it has aided several investigations in the biomedical research, as it has allowed the measurement of mechanical properties in thin body parts, such as the cell-walls of the sponge-like part of bones (*trabecular*) or the hematoma calcification process that leads to atherosclerotic plaques. Nanoindentation has also been used to study animal teeth in order to assess possible reasons behind anomalies in human migration behavior in the Stone Age.[21] All in all, this technique is crucial for the mechanical characterization regardless the actual research field in which the general analysis is performed.

UNIVERSITAT POLITÈCNICA DE CATALUNYA
BARCELONA**TECH**
Escola d'Enginyeria de Barcelona Est

As for the application of nanoindentation in the study of hardmetals, the first recorded test was done in 1996 by Gee et al.,[23] who found the technique to be a useful asset to obtain valuable data about the in-situ properties of the composing phases. Some years later, Bonache et al.[24] drove a depth-controlled experiment with shallow nanoindentations (30 nm depth) and reported a hardness and indentation modulus for the prismatic planes of the tungsten carbide. Shortly after that, Cuadrado et al.[25] used a Berkovich diamond indenter with loads up to 0.25 N to measure the hardness of individual crystals of WC in a WC–Co system.[9] In 2015, Roa et al.[18] conducted a statistical analysis after large amounts of nanoindentation data that allowed them to derive hardness and elastic modulus values of the cobalt matrix, the prismatic and basal planes in the reinforcing phase.

2.2.2.   Tomography

The most traditional approach to microstructural study in materials science has been the two-dimensional analysis of images taken with different equipment, namely by means of optical microscope, scanning electron microscope, etc. However, the major drawback of this method is the loss of the phase arrangement in the third dimension, thus making the sample an incomplete portion of the actual material under study. In fact, there are several cases in which the microstructure may change dramatically in the third dimension. Microstructures of bulk materials such as dendrites formed from liquids, crack distributions in deformation zones, reinforcement shape and orientation in composite materials, among others illustrate some clear examples.[26] Hence, material characterization techniques that provide three-dimensional information are particularly beneficial in the study of a wide range of systems.

Techniques that allow the study of samples in three dimensions are known as tomography. There are many methods under this denomination that are mainly divided in two groups: *projection-based* and *section-based* tomographies (see Figure 9). The first group is comprised of techniques that are typically non-destructive,[26] as they normally involve the incidence of radiation on the sample, which yields a projected 2-D image of it. This procedure is repeated at different distances or angles to the sample, thus providing a large number of projections that are afterwards subjected to three-dimensional reconstruction. Meanwhile, section-based methods use a series of 2D images taken at different positions along the orthogonal direction to rebuild the 3D microstructure. Therefore, these techniques are destructive in nature, as the 2D images require sample cutting and polishing, ion milling, etc. Once the experimental data acquisition is finished, the structure is reconstructed and analyzed using image processing and visualization software.[27]

An example of a projection-based tomography method is X-ray tomography. This technique records X-ray attenuation as a function of angle of rotation to produce a two-dimensional image. A series of these images are collected as a function of distance along an object and concatenated

UNIVERSITAT POLITÈCNICA DE CATALUNYA
BARCELONA**TECH**
Escola d'Enginyeria de Barcelona Est

into a three-dimensional volume. Spectroscopic and X-Ray diffraction techniques typically measure the average properties of relatively large volumes of material. X-Ray micro-tomography has a resolution on the order of a micron, but has limited chemical sensitivity.[28]
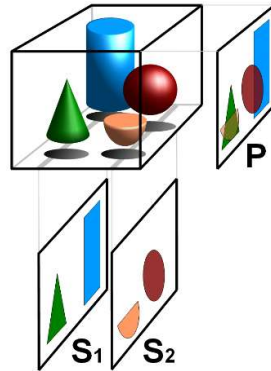

Figure 9. Differences between projection- (P) and section-based (S$_{1,2}$) imaging.

As regards serial sectioning, a major issue is the depth of removal between sections i.e., the distance between each micrograph. This depth must be a fairly reduced fraction of the features of interest, so that their representation in the out-of-plane direction is accurate enough. In fact, the sectioning depth has to be of similar size to the in-plane spatial resolution of the image, so that three-dimensional distortions are minimized. Consequently, the better the spatial resolution in plane, the more precise the sectioning has to be.[27]

As such, making tomographies out of SEM images requires high precision sectioning, because the spatial resolution is in the order of the nanometers. This is why the focused-ion beam (FIB) microscope has aroused as the most used tool for this type of tomographies.[26], [27] These microscopes are able to focus highly energetic ions to extremely small spot sizes (in the order of 5–20 nm). This minor spot size together with a finely-controlled movement of the ion beam allows the precise removal of material at the nanoscale via ion sputtering milling.[27] Besides, FIB microscopes enable both sectioning and data collection to occur in the same chamber. The sectioning is pursued by first milling a flat surface and then rotating the sample to image the newly formed surface. This process is subsequently repeated to obtain images at various depths in the sample.[28] Once the volume of interest is covered by the sectioning, the resulting sections are processed by a computer software that digitally reconstructs the sample. An example taken from actual experiments on tungsten carbide is shown in Figure 10.
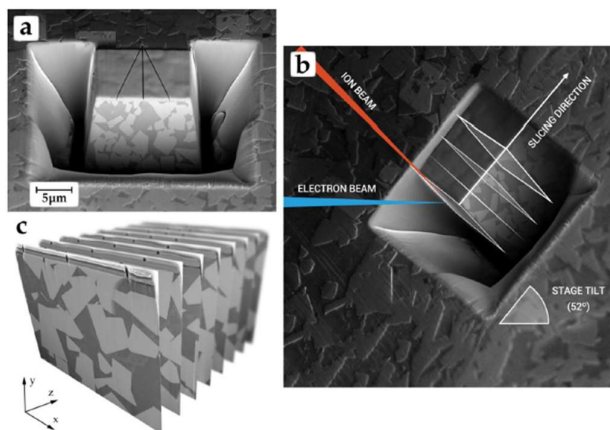
Figure 10. Stages of a FIB tomography: a) surface preparation with reference marks; b) schematic view of FIB sectioning; c) resulting images that will be the input for the reconstructing software.[14]

Given the complex geometry of the interconnected carbide-cobalt skeletons in hardmetals, tomography seems to be a proper technique to their study. For instance, Jiménez-Piqué et al.[14] performed such an analysis over three grades of WC-Co with different carbide grain size and binder content. They obtained conventional microstructural parameters (mean free path, grain size, contiguity and phase percentages), which were in good agreement to the analogs estimated by 2D measurements. An improvement in the understanding of binder distribution was achieved, as it was possible to observe its actual percolation through the carbide reinforcement by means of a skeletonization algorithm (see Figure 4). Finally, they meshed the 3D model and ran finite element simulations that allowed them to evaluate the residual thermal stresses that were present in the structure. They have proposed to perform similar studies including grain orientation, which can be achieved my using EBSD (Electron Backscattered Diffraction) instead of secondary electrons.

2.3. The Finite Element Method

As jet propulsion was being improved at giant steps in the 1950s, there was a greater necessity to develop more aerodynamic fuselages to reduce drag. This led to the introduction of delta wing shapes that made it quite challenging to calculate stresses analytically. As a result, a group of researchers working at Boeing's Structural Dynamics division developed a method to perform these calculations by means of dividing the wing skin in triangular plates.[29] The research was published in an article in 1956 that established the procedures of element matrix assembly and element formulations.[30] However, it was not until 1960 that the term 'finite element' was coined by Ray Clough, who was one of the authors of the 1956 publication. Mathematicians would later on discover a publication released in 1943 by R. Courant, in which he used triangular elements with variational principles to solve vibration problems, that at the time had gone unnoticed.

The Finite Element Method lacked of a theoretical basis for many years, which made it unacceptable in many academic circles. Nonetheless, this did not prevent the method from being applied in engineering design. The American National Aeronautics and Space Administration (NASA) funded with $3.000.000 (around of $41.000.000 in 2021) the development of a finite element software tool, which would later on be known as NASTRAN. It was not until the late 1960s that the FEM caught the interest of mathematicians, who would in turn demonstrate that in linear problems, the solution given by the numerical method converges to the correct solution of the partial differential equation.[31]

The 1970s is known as the golden age of FEM, as numerous companies that developed novel software tools were established, many of which remain until our days. For example, John Swanson, an engineer at Westinghouse Electric Corp. that had been developing a finite element program for analysis in nuclear power plants, established his own company in 1969, which led to the release of ANSYS in 1971. On the other hand, a company known as HKS launched the first version of its ABAQUS software in 1978. This program was initially focused on nonlinear applications, but gradually linear capabilities were also added. In fact, ABAQUS had a great reception among researchers due to the introduction of gateways to the software, which allowed the users to add new material models and elements.

The major constraint to the further use of FEM has always been the processing capabilities of the computing equipment. For instance, the most powerful processor in 1966, the Control Data 6600, could process a maximum size of 10,000 elements and the analyses would take several hours. Nowadays, this type of analysis can be done in a matter of seconds and the size upper boundary has exponentially grown.

The computer assisted engineering (CAE) industry has grown exponentially since those early days. ANSYS went public in 1996 and was worth $1800 M by 2005, while HKS was sold to Dassault Systemes in the same year for $ 413 M. The use of this method was also regulated by the American Society of Mechanical Engineers (ASME) in 2006.[31] Figure 11 shows a timeline with several milestones in the development of the Finite Element Method.

Current FEM software offer a wide range of analysis capabilities: stress and strain analysis in mechanical load cases, flow behavior, thermal analyses, etc. It is even possible to assess electromagnetic field distributions, which is useful in microelectronics. Therefore, FEM programs are extremely versatile and allow the user to study complex scenarios in which there are numerous conditions affecting the system. For example, the component temperatures within an electronic microdevice can be assessed through a combination of fluid and heat conduction analysis, in order to analyze the cooling effect of the air flowing around them. The temperature profiles in the electronic components can be used in turn to evaluate the thermal stresses, which are critical for a long-term life of the microdevice.[31]

UNIVERSITAT POLITÈCNICA DE CATALUNYA
BARCELONATECH
Escola d'Enginyeria de Barcelona Est

Last but not least, numerical simulations do not replace experimentation. Their main use is to find a proper set of conditions that reduce the experimentation times and the subsequent costs. Besides, successful FEM models undergo a series of validation procedures before they can be trusted as prediction models, i.e. their results are to be contrasted with a number of experimental results, so that the model is both validated and calibrated.
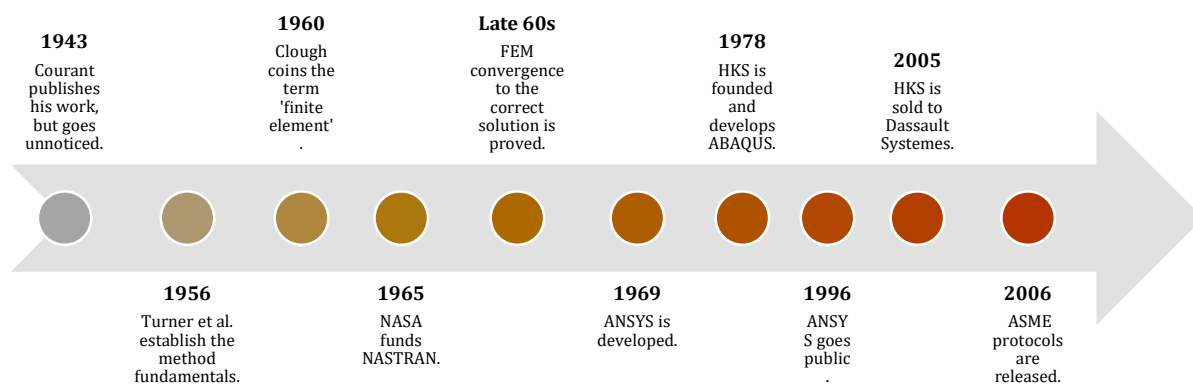
1943
Courant publishes his work, but goes unnoticed.

1960
Clough coins the term 'finite element'.

Late 60s
FEM convergence to the correct solution is proved.

1978
HKS is founded and develops ABAQUS.

2005
HKS is sold to Dassault Systemes.

1956
Turner et al. establish the method fundamentals.

1965
NASA funds NASTRAN.

1969
ANSYS is developed.

1996
ANSYS goes public.

2006
ASME protocols are released.

Figure 11. A timeline depicting several milestones in the development of the FEM analysis.

2.4. State of the art

2.4.1. Simulations of nanoindentation

The simulation of nanoindentation experiments started shortly after the presentation of Oliver and Pharr's work on the method. In 1997, Lichinchi et al.[32] developed an axisymmetric two-dimensional model of nanoindentation over TiN-coated high speed steel (HSS) using ABAQUS, in which the indenter was conical in shape but with the same contact area as a Berkovich tip. They also created a three-dimensional version using an actual Berkovich geometry, in order to assess whether the planar case yielded proper results. In both cases a perfect elasto-plastic model was used. Besides, the influence of the substrate was also evaluated by modelling indentations at different depths.

An early outcome of the comparison between the 2D and 3D models was that the results were similar, which in essence is a good result as the planar model is more computationally efficient. Then, they contrasted the results with experimental data and found that there was a good match, particularly in the first part of the unloading curve where the elastic modulus is calculated. However, it was noticed that the loading stage showed a larger deviation, which they claim that

could be due to differences in the assumed yield strength or the lack of a hardening rate. As for the substrate influence, the both the strain fields and the calculated hardness and elastic modulus showed that the there was no substrate effect when indenting up to 15% of film thickness. This result agrees with the general criterion of indentation depth limit of 10-20% of film thickness that is experimentally applied.

In 2009, Sakharova et al.[33] performed three-dimensional simulations of Berkovich, Vickers and conical nanoindentation tests to investigate the influence of the tip geometry on the results of materials with and without coatings. The ratios between the indenter projected area and the square of the indentation depth were equal to 24.5 regardless the indenter type. Meanwhile, 22 different bulk materials (whose yield stress oscillated from 1 to 20 GPa) plus 9 coating combinations were studied. A Swift model for plastic behavior was used, hence introducing a hardening effect. Furthermore, the effect of friction on the simulation results was assessed by varying it from 0.04 to 0.3. The model was run in an in-house software that was developed to simulate processes including severe plastic strains.

In cases where the ratio between the residual indentation depth (h_f) and the maximum depth (h_{max}) was large, it was established that there was almost no difference between the loading and unloading curves for the different indenter geometries when testing bulk materials. Nevertheless, there were differences among the indenters when the h_f/h_{max} ratio was low (i.e. hard samples). Moreover, it was observed that strain distributions are dependent on indenter geometry. This is the case of the Berkovich indenter, which shows higher strains than for the Vickers and conical tips. As for the study of coatings, the researchers established that the results differed noticeably when using different indenters and the ratios between the film and substrate hardness were greater than 2. Lastly, the model seems to be insensitive to the variation of the friction coefficient.

Csanádi et al.[34] simulated nanoindentation tests over a WC-coated steel substrate using both FEM and extended FEM (XFEM) in 2017. The latter is a numerical method that allows effective description, both in quantitative and qualitative terms, of individual stages of material damage in microstructure under load.[35] In fact, it enables spontaneous crack nucleation, which is quite useful when dealing with complex geometries where it is not evident where exactly the cracks may form. They have tested both the substrate and the coated system and proposed a method to enhance the simulation of plastic pile-up that is observed when indenting ductile materials. Coating delamination was modeled using the XFEM method at the film-substrate interface. However, the materials were modelled using an isotropic perfectly plastic model.

The FEM simulations performed by this group could successfully emulate both the pile-up formation and the coating delamination in a realistic way. They could also develop a method that accounts for this pile-up and avoids the overestimation of hardness that comes along the pile-ups. The damage criterion and its application in the frame of the model made it was possible to

UNIVERSITAT POLITÈCNICA DE CATALUNYA
BARCELONA**TECH**
Escola d'Enginyeria de Barcelona Est

determine the fracture energy (G) and the fracture toughness (K_{Ic}), through the combination of the data yielded by the XFEM and the Griffith-Irwin relationships.

The most recently and related approach to the topic of this project was taken by Lindner et al.[36] in a paper published in 2020. They used the finite element method to study the interplay between geometric constraints in the binder phase in hardmetals. Thus, the binder geometry was obtained from a 3D reconstruction that was performed following the method developed by Borgh et al.,[37] which in turn enabled the authors to ponder the geometrical effects that occur in real microstructures. The plastic behavior was introduced by means of a Hollomon model, hence accounting for hardening. In fact, they have used the hardening coefficient of this model (i.e. the strain-hardening exponent n) as a fitting parameter that has allowed the authors to represent the constraining effect that is experimentally encountered. Lastly, friction was introduced with a friction coefficient of 0.1, which Lindner et al. state yields proper results that lay in between taking no coefficient and taking high friction conditions.

The authors have been careful with the development of the model, as they have started modelling bulk materials in 2D, followed by three-dimensional representations of coated substrates with different coating dimensions and a reconstructed binder volume. However, the effect of the carbide skeleton was introduced by means of boundary conditions i.e., the tungsten carbide phase is not strictly modeled. This is because modelling an elastic reinforcing phase or even an analytically rigid one would result in a higher computational time. Given that the researchers acknowledge that this approximation is only valid when the indentation is performed far away of the carbide, a second set of simulations of cobalt-coated WC were performed. Nonetheless, the geometry used for these models is simplified, hence losing the stress-concentrator effects that are likely to occur in a real microstructural geometry. Meanwhile, the use of the strain-hardening exponent as a fitting parameter proved to be useful for calibrating the simulation. As a result, the authors propose to perform a similar analysis applying more complex models over a real microstructure, while keeping the same model architecture, in order to reduce the discrepancies between the simulation results and the experimental ones.

To conclude, these four publications attempt to show a progression of the concrete topic of this project. More articles[38]–[44] were consulted but their summary here is avoided as they do not actually provide much further information on the subject. Instead, they could be taken rather as a validation of some of the other works presented here. There are many lessons that can be learned for these scientific works. Firstly, it is possible to accurately simulate nanoindentation by means of the finite element method. Secondly, 2D models are broadly used, despite the fact that many authors explicitly acknowledge that strains resulting from indenter anisotropy is lost. Then, simple elasto-plastic constitutive models are used for ductile materials. Some works do not even consider the hardening effect. Besides, there is no clear agreement among the researchers on whether the indenter-sample contact is to be modelled with friction or not. Last but not least, there

UNIVERSITAT POLITÈCNICA DE CATALUNYA
BARCELONA**TECH**
Escola d'Enginyeria de Barcelona Est

are no works where nanoindentation is simulated on real 3D microstructures accounting for both binder and reinforcement phases.

2.4.2. Crystal plasticity

As explained above, a major field where research is yet to be conducted within the simulation of nanoindentation tests is the application of complex constitutive models for the phases involved, especially when it comes to modeling ductile materials such as the cobalt binder in cemented carbides. There is a set of constitutive laws that are especially suitable for fitting the behavior of ductile polycrystalline metals that are subjected to anisotropic and large deformations under isothermal conditions. These models are known as *crystal plasticity models*, since they explicitly represent discrete grains and slip systems, which account both for the anisotropy of single crystal properties and texture effects. However, these theories require a large number of internal state variables at every numerical increment, resulting in a higher computational cost.

Although there is a considerable number of crystal plasticity models available, only the model developed by Marin[45] will be used in the present project. In this model, crystallographic dislocation slip is assumed to be the only deformation mechanism. Moreover, the strain gradient is divided into two components: an elastic and a plastic one, which accounts for dislocation motion on distinct slip planes leaving the crystal lattice unchanged. The theory of thermally activated dislocation motion is used for describing the kinetics of slip. In other words, the resolved shear stress on the slip system is decomposed in two components, one accounting for short-range glide (thermally activated) and a long-range slip that does not depend on temperature. Meanwhile, the competition of storage and annihilation of dislocations is assumed to control the hardening process through variations in the dislocation density. As regards the numerical solver, the time integration of the model is implicit.

UNIVERSITAT POLITÈCNICA DE CATALUNYA
BARCELONA**TECH**
Escola d'Enginyeria de Barcelona Est

3. Methodology

The ultimate development of the nanoindentation simulation followed a step-by-step procedure. Firstly, fundamental aspects of the model were studied, namely the contact properties, solver type, sample size, etc. Secondly, the simulation was tested on three different models whose geometry was increasingly complex: homogeneous materials, coated substrates and particles embedded in a greater matrix. Finally, three-dimensional tomography domains were indented and a statistically analyzed.

3.1. Development of the numerical model

3.1.1. Nanoindentation simulation on tridimensional homogeneous samples

Firstly, a Berkovich tip was drawn according to the dimensions shown in Figure 12, which were also checked in different sources,[33], [46], [47] although the tip radius was actually set as 50nm. The geometry was drawn in Solidworks, starting from a 3-faced pyramid that was cut at the upper tip by means of a revolution-cut. This operation resulted in a geometrical instability in the meshing module within Abaqus. Therefore, the meshing of this part was done in Solidworks using second-order tetragonal elements. The resulting mesh (see Figure 13) consisted of 2554 nodes and 1352 elements, with a size refinement towards the rounded tip, making thus sure that its curvature radius is correctly modeled.
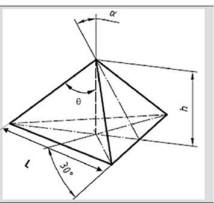
Feature	Size	Berkovich indenter
Semi-angle (α)	65.3 (Degree)	
Apex half angle (θ)	76.9 (Degree)	
Tip radius	200 (nm)	
Height (h)	1 (μm)	
Base length (L)	7.52 (μm)	

Figure 12. Berkovich indenter probe dimensions.[46]
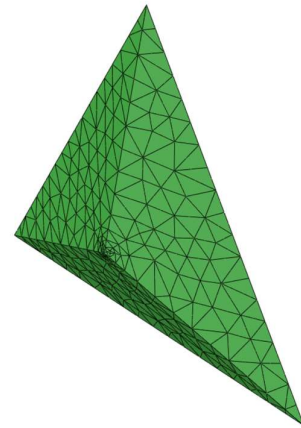
Figure 13. Mesh of the Berkovich indenter.

In contact simulation, there is a rule of thumb which states that the elements in the master surface (in this case, the indenter) must be considerably coarser than their counterparts in the slave surface, thus reducing notably the degree of master surface interpenetration into the slave

surface (*overclosure*). Given that the elements in the indenter tip cannot be furtherly increased in size without compromising the correct representation of the tip radius, reducing the element size in the contact surface is the only option left to comply with this rule of thumb. The mesh refinement in the contact area implies higher computational cost, thus requiring great efficiency in the selection of the different solving methods.

A set of simulations on simple cobalt blocks was launched to test both the element size that ensured a proper contact interaction and the contact solving method. Two "Hard Contact" conditions were tested: the direct or Lagrange method and the Penalty algorithm. The first of these forbids the interpenetration between the meshes of the surface pair, although it requires the system to solve several equations for each node in contact, resulting in an increased computational cost. The Penalty algorithm allows a limited degree overclosure to occur, thus allowing faster simulations. In addition, both contact properties were defined as frictionless as a first approach, which is also the common practice as found in literature.[42], [44] The contact interaction was set as 'General contact', which ensures there is a contact condition whenever a pair of nodes belonging to a free surface meet each other.

These two methods were tested by nanoindentation simulations controlled by displacement up to 200 nm, using the meshes shown in Figure 14. These meshes differed in the average element size: 110 nm and 220 nm. The finer mesh (see Figure 14.a) consisted of 72,558 nodes and 50,571 elements, whereas the coarser one involved 20,391 nodes and 13,784 elements. Tetrahedral elements of second order were used in both cases. The elastic properties of cobalt chosen for the simulation are shown in Table 2, whereas for the plastic properties an experimental curve was inserted (see Figure 15). Boundary conditions in the sample mesh were applied to the nodes on the base and prevented them from moving in any direction and/or twisting. The indenter used was the one shown in Figure 13 and the boundary conditions were applied to the nodes at its top surface, allowing them to move only in the vertical direction. On the same set of nodes, a displacement of 200 nm was set, although this magnitude would be reached following a linear amplitude depending on the solver time, as shown in Figure 16. The indenter tip was defined as diamond using the elastic properties also shown in Table 2.
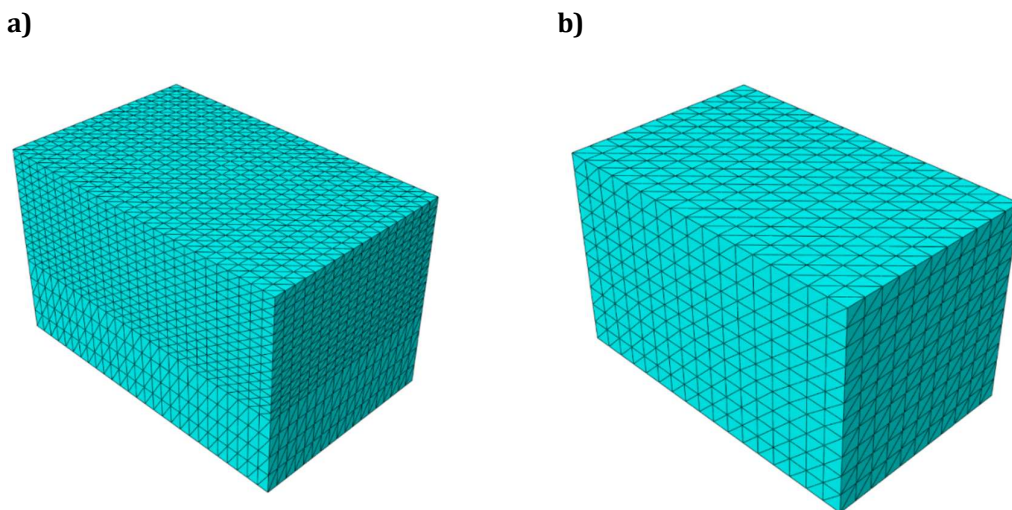
a)   **b)**

Figure 14. **a)** Finer (110 nm) and **b)** coarser (220 nm) meshes for contact property evaluation.
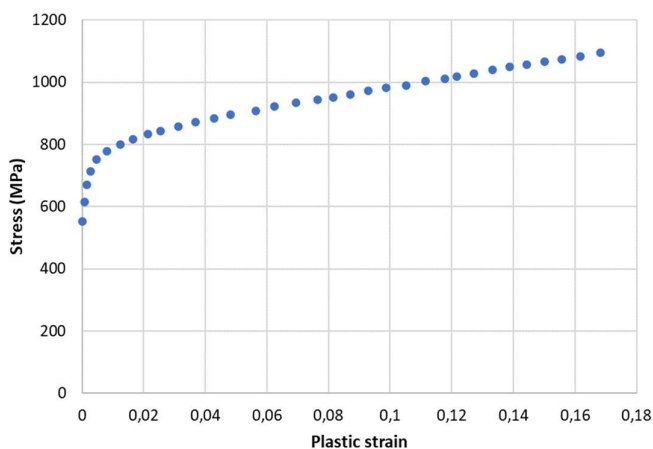

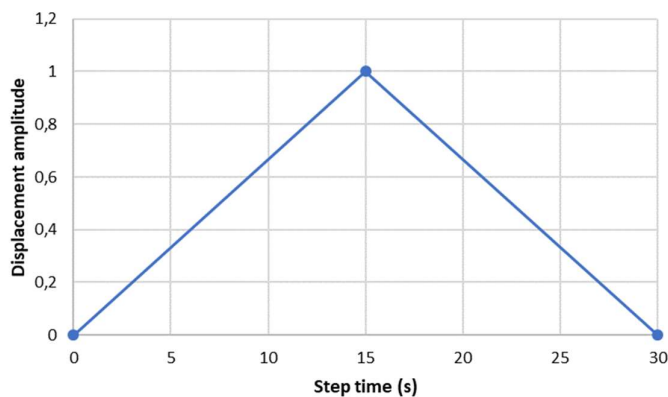**Figure 15.** Plastic curve used for modeling cobalt plasticity.

Figure 16. Amplitude of the indenter displacement as a function of solver time.

UNIVERSITAT POLITÈCNICA DE CATALUNYA
BARCELONA**TECH**
Escola d'Enginyeria de Barcelona Est

Table 2. Elastic material properties used in the simulations.

	Co	WC	Diamond
Elastic modulus (GPa)	230	600	1140
Poisson's coefficient	0.3	0.2	0.07

Once the contact solving method and the appropriate element size were established, the first simulations were performed over large cylinders made out of either pure cobalt or carbon tungsten, in order to assess if the simulation arrangement was indeed working properly and make the appropriate corrections if needed. This allows the comparison between the elastic modulus obtained using the simulation data (i.e. indentation load as a function of displacement) with the parameter originally inserted in the model. The meshes were created in such a way that they were significantly finer in the indentation area on the sample (see Figure 17b), as found in some simulations in the literature[40], [42]. The main reason behind this element arrangement is the above-mentioned rule of thumb that ensures little overclosure.

In Figure 17a, the model assembly consisting of the sample and the indenter is shown, while the sample mesh is depicted in Figure 17b. The cylinders had a diameter of 20 μm and were 10μm in height. Several partitions were performed on the sample block that would allow a better control on the seeding of element size when it came to meshing it (straight longitudinal lines in Figure 17a). This resulted in 98,969 nodes arranged among 70,994 tetrahedral elements, that were also defined using a second order form functions. Other model parameters such as boundary conditions and displacement amplitude remained the same as the ones used in the optimization of the contact model. As for the material definition, the properties in Table 2 were used, as well as the experimental plastic curve used in the analysis mentioned above. However, the tungsten carbide was modeled as an ideal elasto-plastic material, using the Tabor rule for its yield strength, i.e. a third of its hardness. Taking this property as approximately 24 GPa[18], the resulting yield stress was 8000 MPa. The only difference between the nanoindentation simulations performed on pure carbon tungsten and cobalt alloy laid on the material property that was applied on the sample, which can be easily toggled in the software by means of sets definitions.
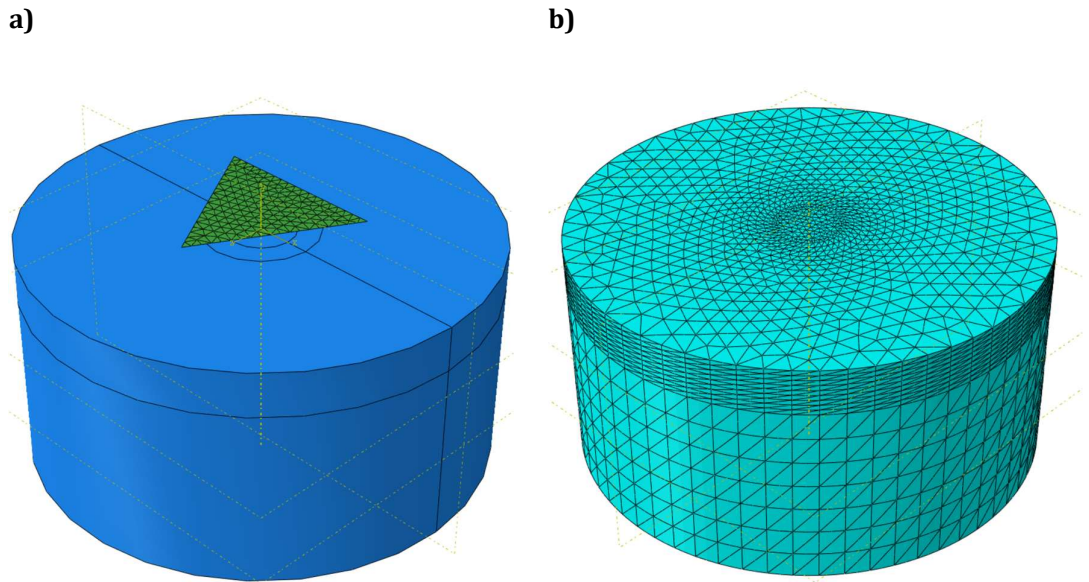
a)   **b)**

Figure 17. a) The assembly of the model used for the homogeneous indentation tests and **b)** its mesh.

Using the results obtained with this simulation, i.e. reaction force and displacement values in the nodes located at the indenter base, a typical nanoindentation analysis following the method developed by Oliver and Pharr[22] was done. To pursue this, the reaction force nodal values were added in order to obtain the total magnitude of the indentation force at each displacement, while the corresponding displacement data were averaged. Moreover, the unloading stiffness (*S*) was obtained using a self-made MATLAB subroutine (see 'function_Nano_properties' in Annex A1) that would linearly adjust the unloading data until a R-squared value of 0.99 was reached, thus ensuring an optimal adjustment. The contact area was estimated using Equation 3, considering the maximum depth value with the correction due to elastic effects in the surroundings (h_c).

Equation 3.

$$A = 24.5 \cdot h_c^2$$

3.1.2.   Initial tridimensional approach to the tomography simulation

The group had already created two meshes out of the tomographies performed on WC-Co samples that differed in the size of the cobalt matrix. The tomography was 13.6 μm in length, 7.2 μm wide and 11,48 μm high. The corresponding mesh consisted of between 2.7 and 3.5 million of nodes with an average element size of 220 nm (see Figure 18). Consequently, the large number of nodes results in an enormous computational cost for the equipment, which could be clearly appreciated during the model preparation. For example, simple and usual operations for model assembly such as part rotation were surprisingly slow, which could be explained by the large graphic rendering needed.
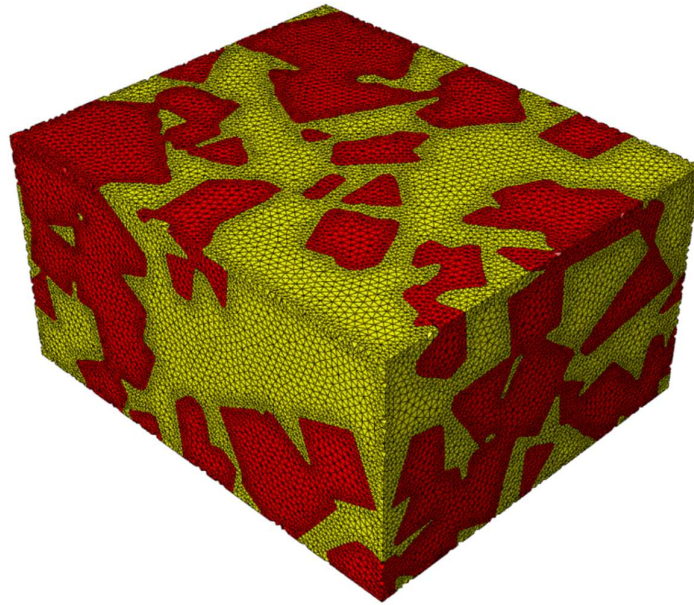
Figure 18. Mesh of a tomography of a coarse-cobalt WC-Co sample. Tungsten carbide phase is in red, while the cobalt matrix is in yellow.

Despite the above-mentioned difficulties, a model was prepared using both a tomography mesh and the already meshed indenter. Cobalt was considered as an elasto-plastic material with an elastic modulus of 230 GPa and Poisson coefficient of 0.3. For the plastic model an experimental curve was used (see Figure 15). On the other hand, both the tungsten carbide and the indenter tip were considered as elastic solids. The elastic modulus used for tungsten was 600 GPa and a Poisson coefficient of 0.2, whereas the Berkovich tip was modeled as diamond (E=1140 GPa and v=0.07).

A 'Static General' solver with non-linear deformation was used to perform the different calculi involved within the model. The contact interaction was defined as "Surface-to-Surface", in which the slave surface, i.e. the WC-Co tomography, was set as a superficial node region. In addition, the contact property definition consisted of a "Hard contact" solved by the direct or Lagrangean method. Similar studies but using dynamic solvers (Implicit and Explicit) were also performed.

3.1.3. Sample global volume analysis

Meshes built with large number of nodes tend to be computationally expensive and sometimes cannot converge to a solution. Consequently, it was proposed to study different strategies to reduce the number of elements in the mesh. A first approach was to reduce the thickness of the tomography to one half, since it would have a similar impact on the node number. However, this would result in around a million elements, which is still a large number. Therefore, it was proposed to study portions of the already reduced sample: it could be cut in further halves or

UNIVERSITAT POLITÈCNICA DE CATALUNYA
BARCELONA**TECH**
Escola d'Enginyeria de Barcelona Est

even fourths. Nevertheless, it was crucial to check if the stress distribution during the indentation reached the edges, because this would introduce an edge effect on the results, which would be highly undesirable.

Taking these principles into account, new tridimensional simulations on a homogeneous cobalt sample were performed. These analyses differed in the size of the sample, which was defined according to the original tomography size. The different models with their corresponding meshes are shown in Figure 19, Figure 20 and Figure 21. Notice the higher element density in the middle, as it was already done in the model shown in Figure 17. This higher-density domain was cylindrical in shape and went all through the sample thickness, while its diameter was set either 2 or 3 µm. Then, a combination of 6 models with different global and domain size was studied. The elements out of the finer domain were 350 nm in size in all cases. All in all, the main target of this analysis was the definition of a sample size that ensure no border effect in the results.
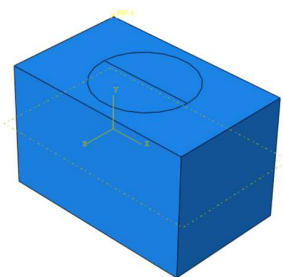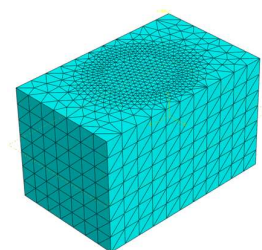
Figure 19. Equivalent to an eight of the original tomography.
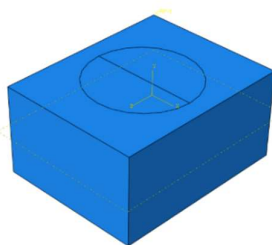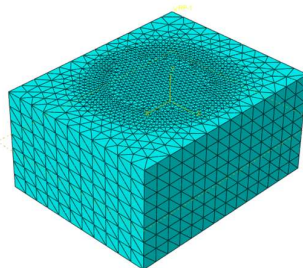
Figure 20. Equivalent to a fourth of the original tomography.
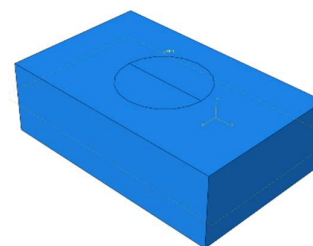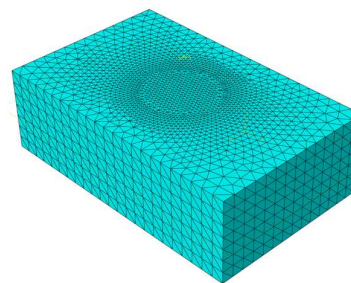
Figure 21. Equivalent to a halve of the original tomography.

3.2. Definition of substrate influence on the results

3.2.1. Coating simulation at different indentation depths

Nanoindentation on films was simulated using the mesh shown in Figure 17, in which the upper finer domain was defined as the coating (2 µm thick), while the region beneath was naturally the substrate. Then, both cobalt and tungsten carbide were defined as either coating or substrate, resulting in two combinations: a soft film deposited over a hard substrate and vice versa. Parameters regarding solver technique, step time, material properties and contact definitions remained unchanged from the homogeneous material simulations explained above. However, the indentation depth varied from 100 to 700 nm in steps of 50 nm, so that the onset of substrate influence on the nanoindentation results could be found.

3.2.2. Particle simulation at different indentation depths

A further model verification consisted of indenting a homogeneous particle embedded in a matrix made out of either cobalt or tungsten carbide. The particles were hemispherical in shape with a diameter of 4 µm, as it would yield a maximum depth of 2 µm, thus following the same trend as for the coatings. In addition, two models with different height were created: a 'large' one that was 11.48 µm height and a 'shorter' one that was 5,74 µm. This was done to seek a lower computational cost that may be useful in more complex systems. Moreover, the models were square in section with a side of 13.6 µm.

The meshes were built using the Avizo software (see Figure 22), as it was not possible to draw a hemisphere with the limited CAD assistant that is incorporated in ABAQUS. A series of pictures were generated using MATLAB in which a circle of decreasing diameter was drawn in the center. Then, a three-dimensional volume was reconstructed out of these pictures by means of Avizo, which enabled the distinction between the particle and the embedded matrix. After the reconstruction, the meshes were generated using the built-in meshing environment in Avizo. A major advantage of this environment is the possibility of defining different element sizes in distinct regions of the volume. Consequently, the resulting meshes are computationally efficient, while allowing to attain accurate information in the zones of interest. The parameters used to build the meshes are shown in Table 3. Lastly, the 'shorter' meshes comprised of 93,249 nodes arranged in 65,637 second-order tetrahedral elements, while the 'large' mesh was made up of 104,790 nodes arranged in 74,382 elements of the same type.
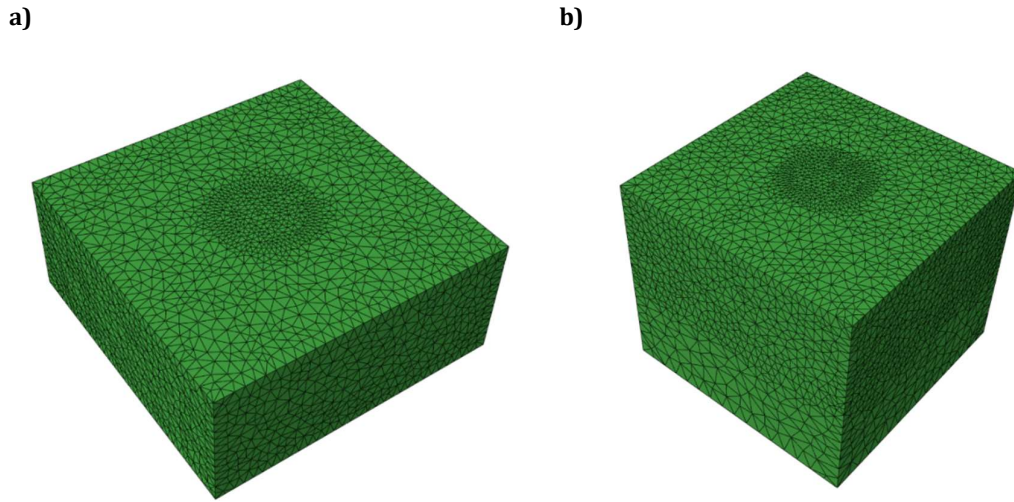
UNIVERSITAT POLITÈCNICA DE CATALUNYA
BARCELONATECH
Escola d'Enginyeria de Barcelona Est

a)   b)

Figure 22. Meshes of the homogeneous particle embedded in an average-property matrix.

Table 3. Meshing parameters in Avizo environment.

Parameter	Particle	Outer matrix	Lower matrix
Boundary layer thickness	220	440	880
Boundary layer cell size	110	220	440
Facet size	220	440	880
Facet distance	11	22	44
Cell size	220	440	880

Once in ABAQUS, the procedures followed with these two matrixes were the same as detailed before. The particles were assigned as either cobalt or tungsten carbide using the above-explained material properties, while the surrounding matrix was defined as the other component. The system was subjected to different penetration depths to assess the onset of substrate influence.

3.3. Adjustment of material models to the microstructure

3.3.1.   Mesh formation on the tomography

The tomography consisted of a series of images at different depths (also named *slices*) as it was explained in the corresponding section of the Literature Review. These slices were processed with a MATLAB script (see Annex A1) in order to obtain new images consisting of a central circular portion of the tomography surrounded by a homogeneous matrix that was square in shape with a side of 13.6 μm. The diameter of the tomography domain was initially set as 4 μm,

but decreased with increasing depth (which was tracked by slice number) until it became zero. From that slice on, there was only matrix, i.e. the pictures were defined as monochromatic. However, the last third of the volume was set with a different color, so that a different element size could be locally defined.

The above-mentioned procedure was performed 12 times on the upper and lower surfaces of the tomography, thus yielding a total of 24 embedded cells. In order to maximize the number of samples, the tomography domains were overlapped with each other, although their centers were separated 2 μm from one another. Therefore, the three-dimensional phase arrangement between two neighboring domains is different enough so as to consider them as separate samples.

Once all 24 slice-groups were defined, they were imported in Avizo considering the dimensions shown in Table 4. Then, the slices were subjected to a segmentation step that enabled the association between pixel color and a particular material or region set, namely WC, Co, outer and lower matrixes, plus the 3D reconstruction. During this step, the pixel regions were smoothed using a built-in algorithm so that no rough edges were present, which can be detrimental for a proper meshing. Furthermore, isolated regions or voids resulting from the three-dimensional reconstruction were merged with the surroundings using another algorithm included in the software. Lastly, meshes were created from the 3D volume applying the same parameters shown in Table 3, while in this case the 'Particle' parameters were applied to the whole tomography domain. An example of a meshed sample is presented in Figure 23

Table 4. Dimensional parameters required when importing slices in Avizo.
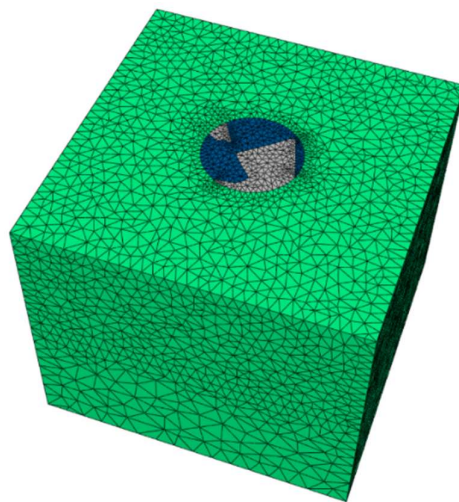
Height (μm)	Width (μm)	Length (μm)
11.48	13.6	13.6

Figure 23. Example of an embedded portion of the tomography surrounded by the matrix with two distinct element sizes.

UNIVERSITAT POLITÈCNICA DE CATALUNYA
BARCELONATECH
Escola d'Enginyeria de Barcelona Est

30

3.3.2. Simulation of embedded cells

The meshes were exported to ABAQUS in a NASTRAN format, as other formats do not keep the material sets defined in Avizo, which are actually crucial for assigning material properties to the different phases involved. Once the mesh was imported, the element type was changed from linear to second-order tetrahedral type by means of the mesh environment available in ABAQUS, because these elements are better suited for non-linear simulations involving contact and plasticity. The same Berkovich indenter used in the previous simulations was placed in the middle of the sample so that it was in contact with its surface. In addition, the same solver (Static General) was used, although the maximum step size was decreased from 0.5 s to 0.1 s, so that more data points were collected. Meanwhile, the contact interaction and the boundary conditions remained unchanged. The indenter was displacement-controlled and its maximum penetration depth was 200 nm following an amplitude like the one shown in Figure 16.

Given that in this case there was a large number of samples to model, the process was automatized through the use of the .rpy file that is automatically created by ABAQUS. This file collects all commands given by the user through the regular interface and translates them into Python sentences. Consequently, this file could be easily turned into an .py file (Python code) and edited with the software Notepad ++, so that the resulting code can be executed on a new NASTRAN file, i.e. the mesh created in Avizo. The .py file can be later on run by calling it with a proper command written in a batch file (.bat), which in turn allows to run many such sentences in sequence. As a result, one can generate whole models in a short period of time. Not only is this method a fast way of creating complex simulation arrangements, but it also assures that all of the resulting models share the same conditions, avoiding user mistakes that may occur when creating these models manually. After running the .bat file, the only aspect to correct is the assignment of boundary conditions in the sample to the proper node sets, as they vary with every sample given that the nodes themselves are named differently.

3.3.3. Material models used

The material sections were created using the same material properties that were already explained in the homogeneous material, coating and particle analysis. However, cobalt properties were introduced using three different models. The first one was the experimental plastic curve that was used in the previous models and is shown in Figure 15. Then, this curve was used to create a new one by shifting the values with a Hall-Petch model developed by Roa et al.[19], who have calibrated a model like the one shown in Equation 1., obtaining value of σ_y^0 of 480 MPa and a k_y of 0.98 MPa·m$^{1/2}$. As a result, a shift of 800 MPa due to Hall-Petch strengthening was obtained when considering a binder mean free path (λ_{Co}) of 1.26 μm.[14] The resulting curve is shown in Figure 24 together with the original one.

UNIVERSITAT POLITÈCNICA DE CATALUNYA
BARCELONA**TECH**
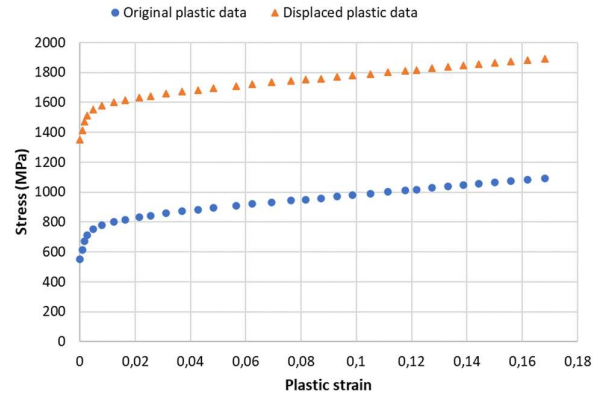Escola d'Enginyeria de Barcelona Est

Figure 24. Original plastic curve and the one obtained through Hall-Petch modelling.

Finally, a crystal plasticity model was also used to simulate the plastic behavior of the cobalt phase. This model was introduced through user subroutine (UMAT) that had been previously created by a member of the research group, who had calibrated it by using the original plastic data shown in Figure 15. One of the model parameters was changed so that it accounted for the Hall-Petch hardening.

4. Results and discussion

4.1. Development of the numerical model

4.1.1. Nanoindentation simulation on homogeneous materials

The results of the initial contact calibration are shown in Figure 25 and Figure 26 as a cross-section of the model at the maximum displacement. There is little overclosure in Figure 25, despite using a larger element size in the sample than the ones in the indenter tip. Therefore, this element size could be used in future simulations, which results in lower computing times. In fact, the simulation time was reduced in around 50% (from 4 to 2 hours). Moreover, these results were obtained using the penalty method for 'Hard contact' resolution, thus further increasing the computing efficiency. However, the use of the finer mesh shows little to none overclosure, although some elements seem to be severely distorted, as it can be seen in Figure 26.
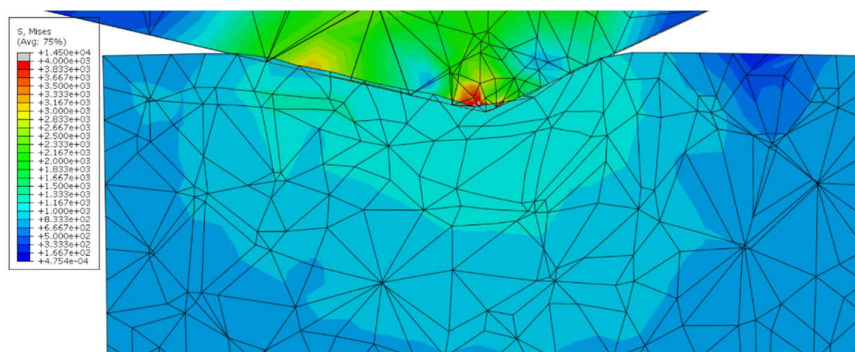
Figure 25. Cross-section of the nanoindentation simulation with an average element size of 220nm.
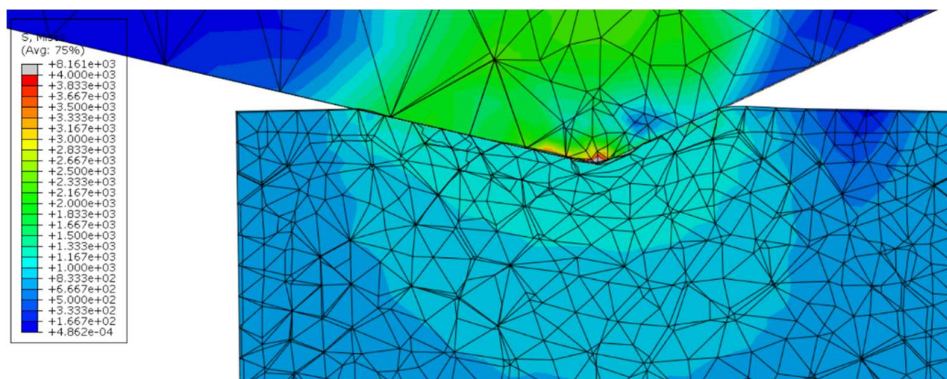
Figure 26. Cross-section of simulation results in a mesh with an average element size of 110 nm.

UNIVERSITAT POLITÈCNICA DE CATALUNYA
BARCELONA**TECH**
Escola d'Enginyeria de Barcelona Est

The successful representation of the contact problem allowed the evaluation of the overall simulation by means of an indentation simulation on both pure carbon tungsten and cobalt alloy separately, using the same contact definition as in the previous analysis. In Figure 27 the indentation print left after the test is shown. The shape of it seems similar to what could be expected in reality. Moreover, the stress field around the print is a perfect circle, which could also be obtained in a homogeneous material. The stress magnitude in color green is around 1000 MPa, which is quite high but still expected in an intensively plastified area, as shown by the curve in Figure 15.
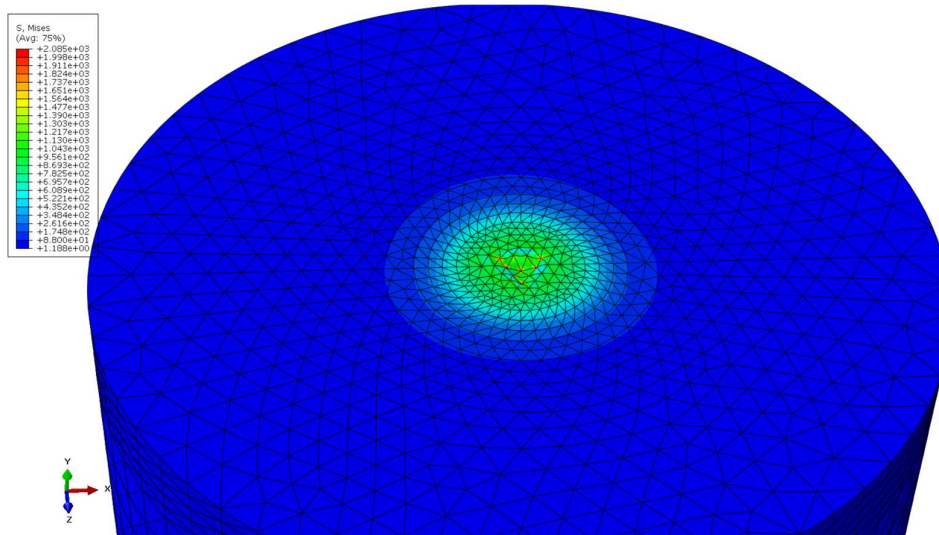
Figure 27. Indentation print left in the cobalt surface once the indenter is lift.

Figure 28 depicts a cross-sectional view of both pure tungsten carbide and the cobalt alloy at the maximum displacement of the indenter probe, since at that point the stresses reach their peak values. As for their magnitude, it is clearly seen that the values between the two models differ in approximately an order of magnitude, which is also expected as the elastic modulus of the carbide is considerably higher. In these images it is also possible to appreciate the differences in the print size, being it larger in the cobalt alloy, what seems coherent when pondering its lower yield stress (around 500 MPa in cobalt vs. 8000 MPa in WC). Finally, the stress distribution in both models was also correct due to the maximum values being in the contact area, plus the progressive stress reduction in isostress-spherical fronts. Nevertheless, the stress fronts are more spherical in the tungsten carbide case than in the cobalt alloy, which could be a consequence of the greater plasticity in the latter case.

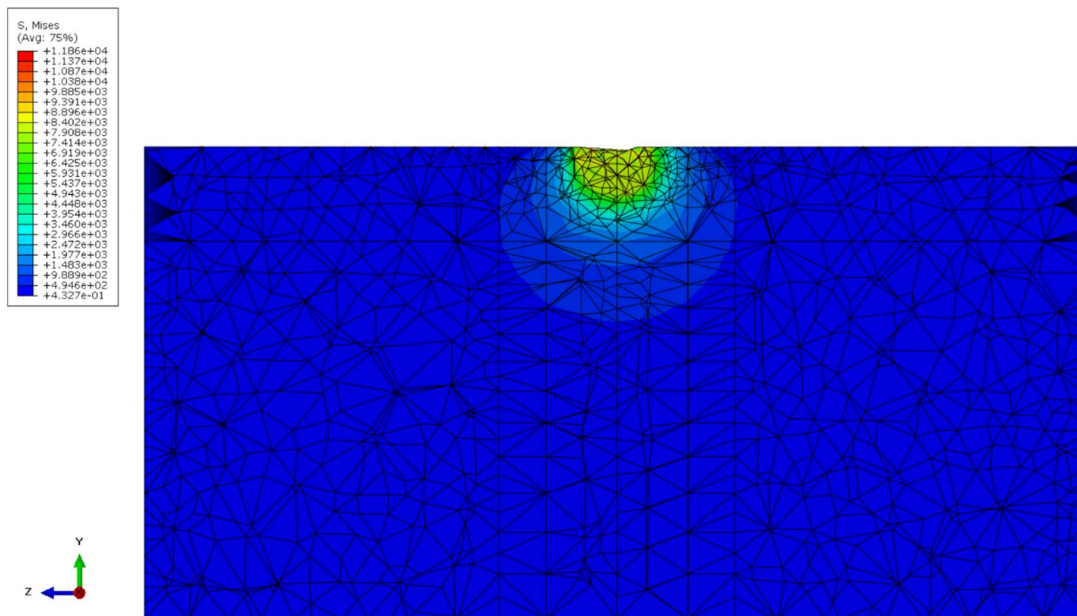UNIVERSITAT POLITÈCNICA DE CATALUNYA
BARCELONA**TECH**
Escola d'Enginyeria de Barcelona Est

a)
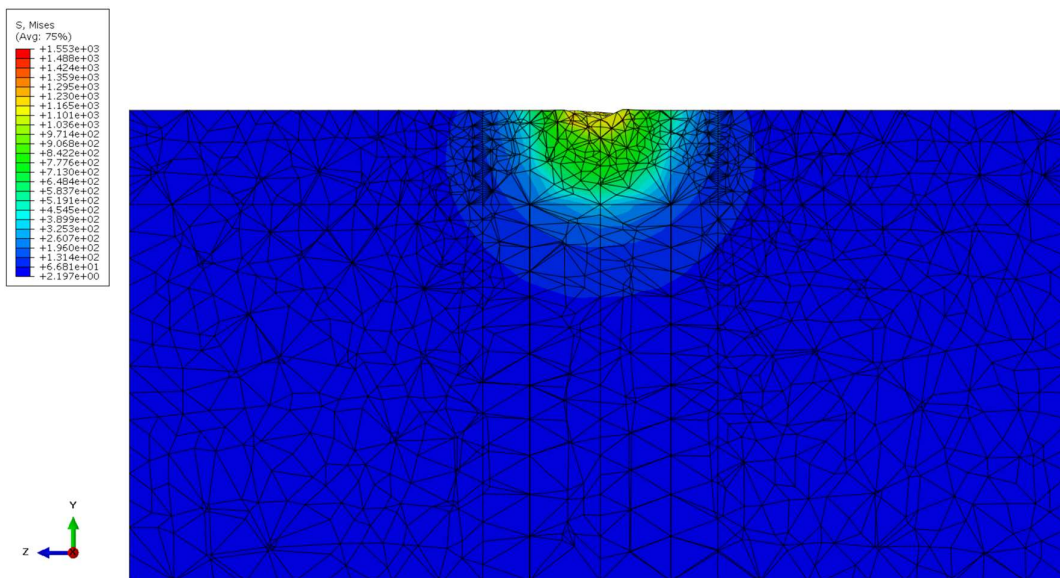
b)

Figure 28. a) Cross-section of the cobalt surface showing the Von Mises stress profile at the maximum displacement. **b)** Same results for the tungsten carbide.

Reaction force and displacement values in the nodes located at the indenter base were taken, aiming to plot the curves of load as a function of displacement that are the typical outcome of nanoindentation tests. The reaction force nodal values were added in order to obtain the total

magnitude of the indentation force at each displacement, while the corresponding displacement data were averaged. The results of this processing can be seen in Figure 29 for both cobalt and tungsten carbide (WC). These curves have at a glance a similar shape to their experimental counterparts (see Figure 8): a curved loading step up to a peak, followed by a linear unloading step. However, there is a wavy behavior in the loading part, which can be better appreciated in the tungsten carbide curve. Indeed, this behavior seems to be an artifact of the numerical model, which may be due to the low number of data points taken. However, taking more points implies more calculation steps and a greater computation time.

The nanoindentation results were also processed following the method developed by Oliver and Pharr.[22] The outcome of this analysis done in both models is given in Table 5. In the case of the cobalt alloy, the elastic modulus obtained was 244 GPa, which is an acceptable value when compared to the input modulus (230 GPa). The same goes for the tungsten carbide, as it resulted in 619 GPa while the elastic model was set using a Young's modulus of 600 GPa. As for the hardness values, they lie within experimental range (see the bottom of Table 5).
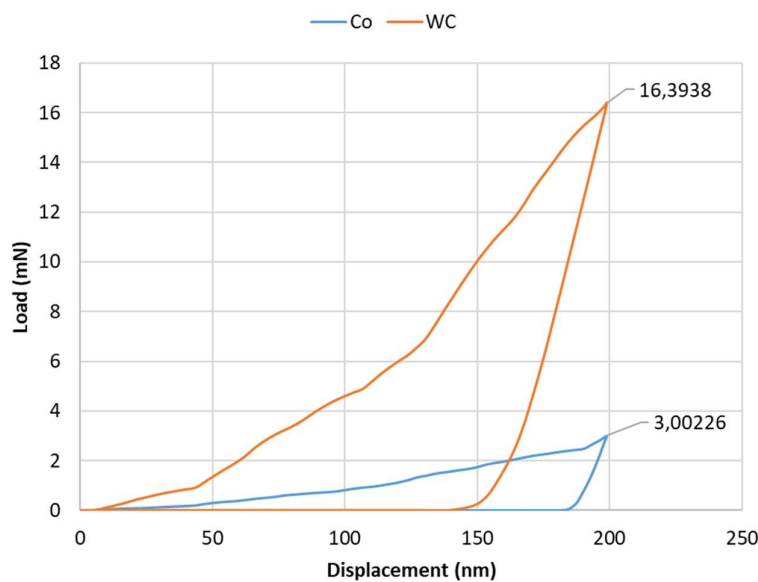
Figure 29. Nanoindentation simulation results obtained over cobalt alloy (Co) and carbon tungsten (WC) respectively.

In conclusion, the model developed in this section seems to give correct predictions of the experimental behavior of homogeneous materials. Consequently, the model configuration used in it can be applied in subsequent models to check whether it allows to correctly simulate the behavior of multi-material samples. A summary of the model parameters as inserted in the Abaqus software is provided in Figure 30.

UNIVERSITAT POLITÈCNICA DE CATALUNYA
BARCELONA**TECH**
Escola d'Enginyeria de Barcelona Est

Table 5. Results of nanoindentation on homogeneous materials.

	Co	WC
S (N/m)	229.700	384.300
P_{max} (mN)	3,00	16,39
h_{max} (nm)	198,99	198,83
h_c (nm)	189,18	166,84
A (m2)	8,77E-13	6,82E-13
E_{ff} (Pa)	2,17E+11	4,12E+11
E (GPa)	244	619
H (GPa)	3,42	24,04
E_{model} (GPa)	230	600
$E_{experimental}$ (GPa)[20]	200 ± 75	475 ± 80
$H_{experimental}$ (GPa)[20]	8 ± 5,5	25,5 ± 5
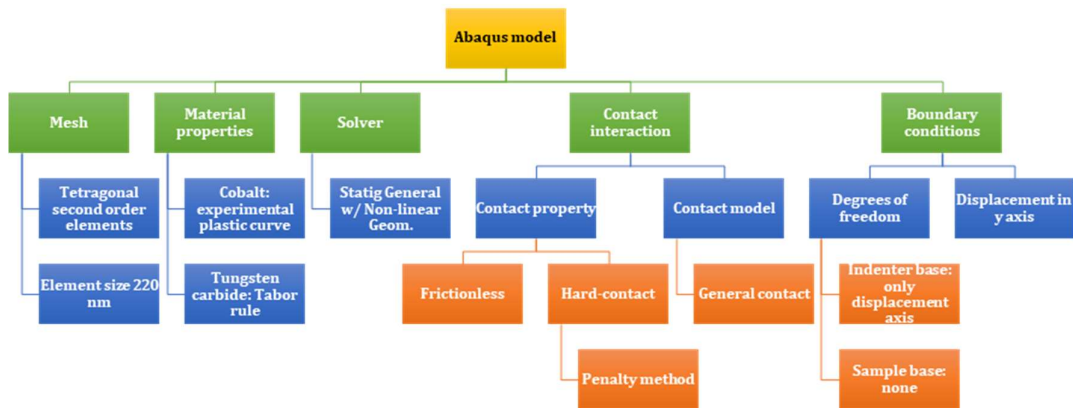
Figure 30. Parameters of the numerical model used as inserted in the Abaqus CAE.

4.1.2. Initial tridimensional approach to the tomography simulation

Despite trying different combinations of contact solving methods, time step solvers, displacement or load control, material properties, etc., it was impossible to obtain any result from the simulations on the mesh generated out of the tomography. For instance, the software could not perform a single time step increment using the 'Dynamic Implicit' solver after processing during 16 hours. A possible explanation to this issue could be that the large node number implies the creation of big solving matrixes, which in turn demand such a large portion of memory space that exceed the space that is actually available. However, the software should compensate this lack of memory by using hard-drive space, but it does not do so. In fact, monitoring the system activity during the simulation showed little processor usage.

As for the explicit methods, Abaqus could obtain some little time increments, although this took such a long computation time that the convergence in a reasonable time is at least doubtful. Besides, a simple compression simulation was performed using both implicit and explicit solvers in order to assess whether the problem was related to contact issues. This simulation was also unsuccessful, which has led to believe that the convergence problem is essentially related to the mesh itself.

Even though there are precedents in three-dimensional simulation of microstructures,[14] it is likely that the numerical instabilities occurred in this case because of the complex stresses developed under the indenter tip. In addition, the large node number results in an equally great quantity of equations to solve. Due to these issues, it was decided that the number of nodes in the WC-Co sample should not exceed 500.000. This limit results from previous experience within the group in the analysis of micropillars that have a similar node quantity.

4.1.3. Sample global volume analysis

The nanoindentation footprint over the sample corresponding to an eighth of the original tomography size is shown at the maximum loading in Figure 31. Given that this was a first approach, no discretization domain was used so that the simulation was quicker. Notice the curvature on the upper and lower edges, meaning that there is a boundary effect on the sample. The analysis was repeated now with a finer domain of 3 μm yielding similar results. Consequently, using a model of this size was discarded.

The same analysis for a sample corresponding to a fourth of the original tomography size is shown in Figure 32. No curvature is seen in any edge, although the stress distribution shows a certain degree of boundary effects on the sides, especially in the direction of lower length. Finally, Figure 33 depicts the results of the analysis when performed on a sample consisting of a half of

the original tomography size. In this case, there is only a slight influence on stress distribution at the upper and lower edges.
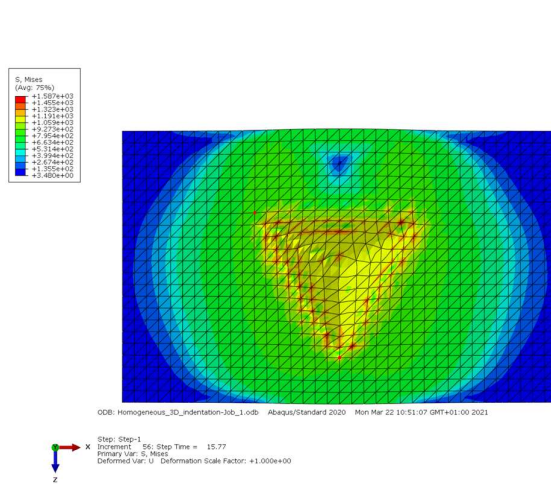

Figure 31. Nanoindentation print left over the sample from corresponding to an eighth of the original tomography size.
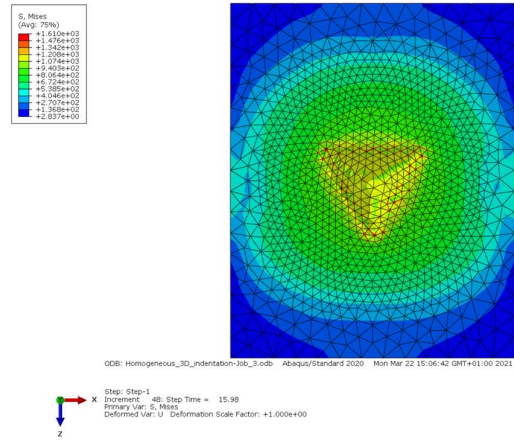

Figure 32. Nanoindentation footprint and superficial stress distribution on a sample corresponding to a fourth of the original tomography size.
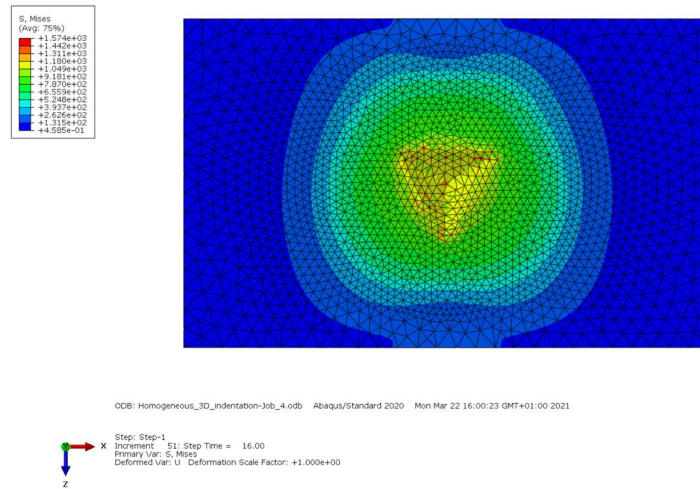

Figure 33. Nanoindentation footprint and stress distribution on a sample corresponding to a halve of the original size.

Indentation load and penetration depth data were extracted for each of the above-presented cases in order to evaluate quantitatively the conclusions obtained by mere observation. These results were plotted in the typical load-penetration depth curves that are shown in Figure 34. It is now clear that the results obtained over the eighth portion of the original sample are substantially different to the other cases, hence confirming that the boundary effects have a relevant impact in the simulation results. Besides that, the difference between simulating a fourth of the original tomography with respect to a halve of it is not as relevant as it was initially thought, thus making

UNIVERSITAT POLITÈCNICA DE CATALUNYA
BARCELONA**TECH**
Escola d'Enginyeria de Barcelona Est

it a possible path for mesh size reduction. Moreover, in all cases the reduction of the domain size from 3 to 2 μm does not produce significant variations. This would allow to work with smaller domains, which results in a lower number of elements in the global model.
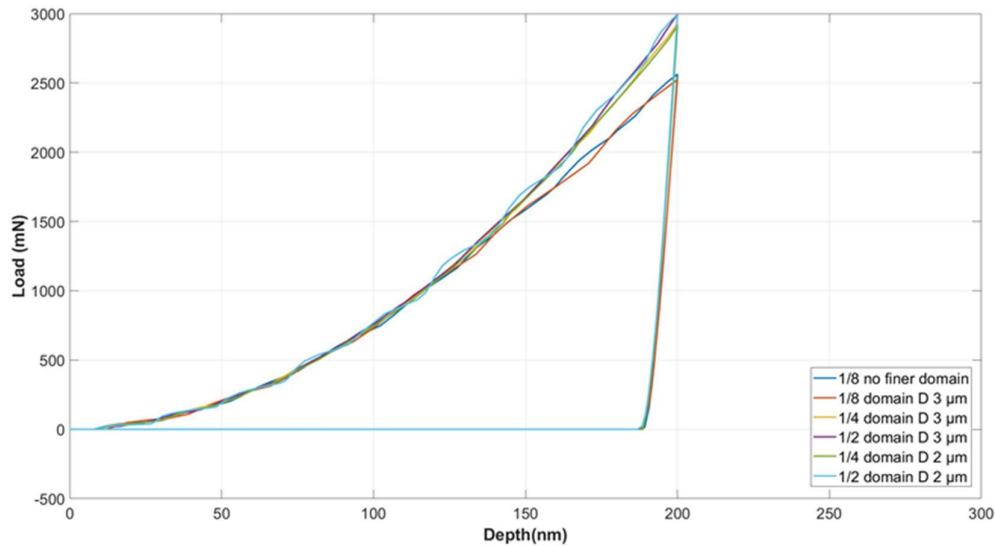

Figure 34. Indentation load as a function of penetration depth for the different simulations.

To conclude, the sample should have the same length as the original tomography, since it ensures that there are absolutely no boundary effects on the results. In fact, the sample should be square in shape owing to both symmetry and boundary effect concerns. As a result, the sample should have a squared-shape surface with a side of 13.6 μm and height of 5,74 μm. Given that applying this approach to the tomography implies still a large computational demand, a different approach was proposed. The tomography could be cut in semispherical domains, which would be subsequently embedded in a matrix of the above-mentioned dimensions. The material properties of the matrix could be an average of both tungsten carbide and cobalt. As the matrix is of no interest, it could be coarsely meshed, thus yielding in a lower number of elements in the global model.

4.2. Definition of substrate influence on the results

4.2.1. Coating simulation at different indentation depths

The load curves as a function of indenter displacement at different maximum indentation depths on the cobalt film are shown in Figure 35. The curves' shape agrees with what was expected, since the loading part is non-linear until a clear peak, after which it decreases following a linear trend until the final unloading stage, where it returns to be curved. Both elastic modulus and hardness were calculated using similar calculations in MATLAB as used

UNIVERSITAT POLITÈCNICA DE CATALUNYA
BARCELONA**TECH**
Escola d'Enginyeria de Barcelona Est

before. The outcome of these calculi is shown as two corresponding curves in Figure 36. The elastic modulus increases from around 200 GPa to 650 GPa, although the increasing rate varies with the indentation depth: the changes between 150 and 250 nm are quite low and remain around 300 GPa within the error margin, while after 300 nm the rise is much steeper. On the other hand, hardness remains more or less unchanged around 3.5 GPa.

Considering that the input elastic moduli for the binder and reinforcement phases were 230 and 600 GPa respectively, the depicted values seem to be quite off-chart. This could be due to the calculation criteria used, as it was verified that changing the R-squared condition in the MATLAB function from 0.99 to 0.98 resulted in values that actually agreed with the input parameters. For example, indentations with a maximum depth of 200 nm resulted in an elastic modulus of 300 GPa when using a R-squared of 0.99, but shifted to 244 GPa when the fore-mentioned condition was set as 0.98. The code is built in such a way that it discards values from the lower part of the curve in order to get a better linear fitting. Therefore, estimations with higher R-squared use less data points, which at some point could result in poorer estimations.
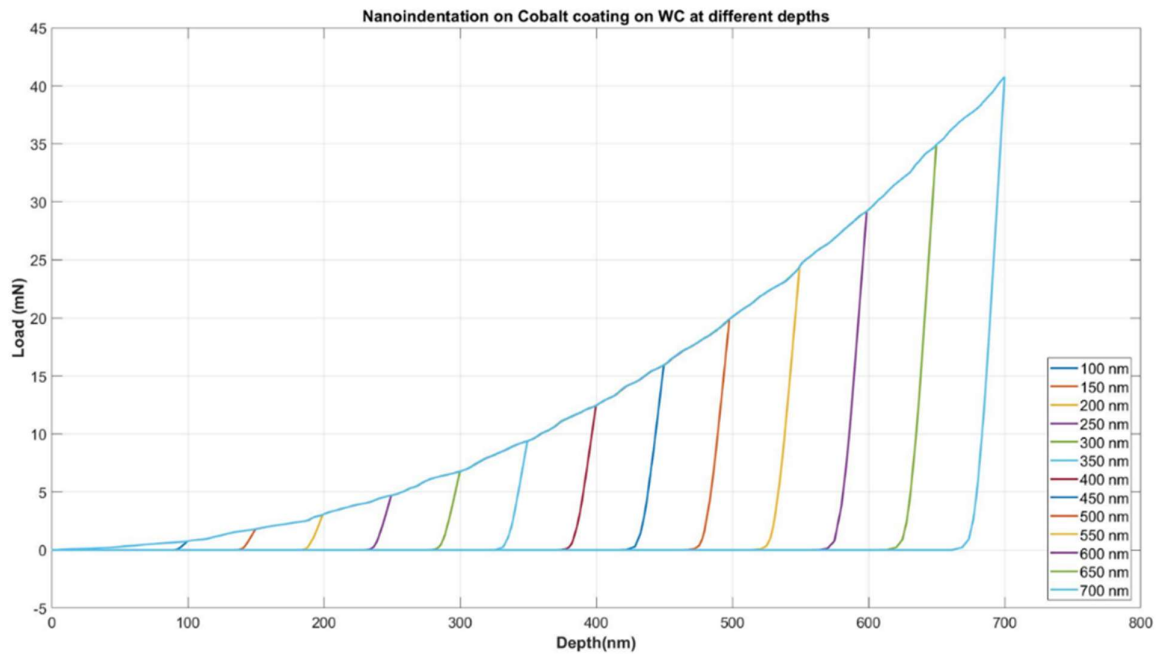

Figure 35. Indentation load curves for the different maximum indentation depths for the cobalt-coated WC.
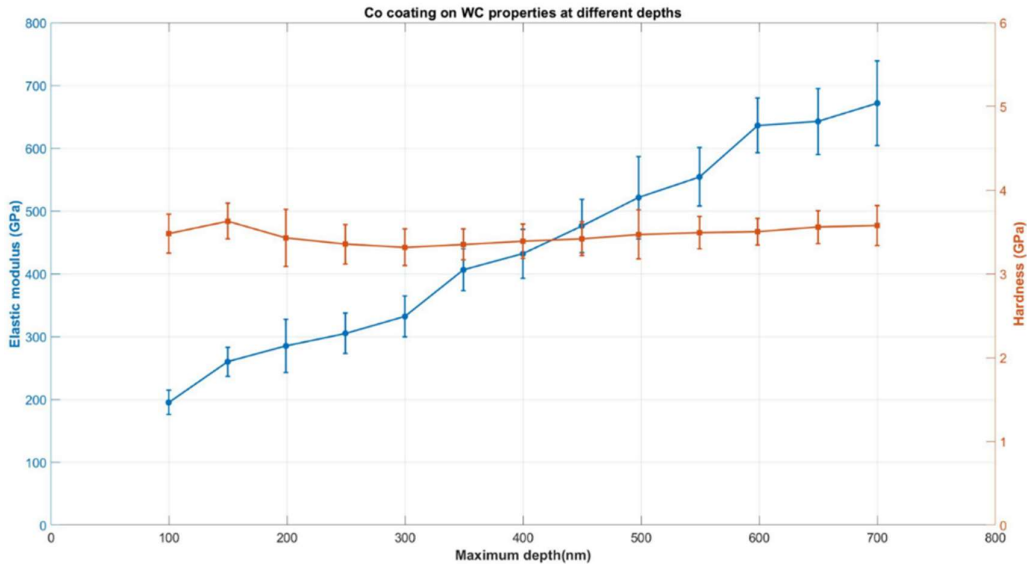
Figure 36. Elastic modulus (in blue) and hardness (in orange) values as function of maximum indentation depth on the cobalt-coated WC.

The steep increase in elastic modulus after 300 nm signals the likely onset of WC substrate influence on the results. As the cobalt coating is 2 µm thick, this result agrees with the accepted rule of thumb that film properties can be successfully measured without significant substrate influence with indentations depths up to a 10-15% of coating thickness. As explained in the State of the Art, this was also checked by Lichinchi et al. when running simulations on thin films.[32] Consequently, these results agree with both the experimental and numerical works that have been previously conducted on the subject.

On the other hand, it is not possible to see any substrate influence in the hardness values. This could be due to the fact that there is no portion of the indenter that is actually in contact with the substrate. Nonetheless, this does not explain why there is no influence through the load transfer between the coating and the substrate. In order to assess this aspect, the cross-sections of the sample are shown in Figure 37 for all of the simulations performed on this system. Notice that at 350 nm there is a fine orange zone at the film-substrate interface, meaning that the maximum stresses within the model are found there. This zone becomes larger in size with deeper indentations, showing that the substrate is indeed loaded. However, the stresses developed do not exceed the 2.5 GPa, while its yield stress was set as 8 GPa, hence being insufficient for the onset of plastic flow in the substrate. A certain degree of substrate influence could perhaps be achieved when indenting at greater depths. Indeed, this was attempted but the strain in the film was so extreme that it resulted in numerical divergence.
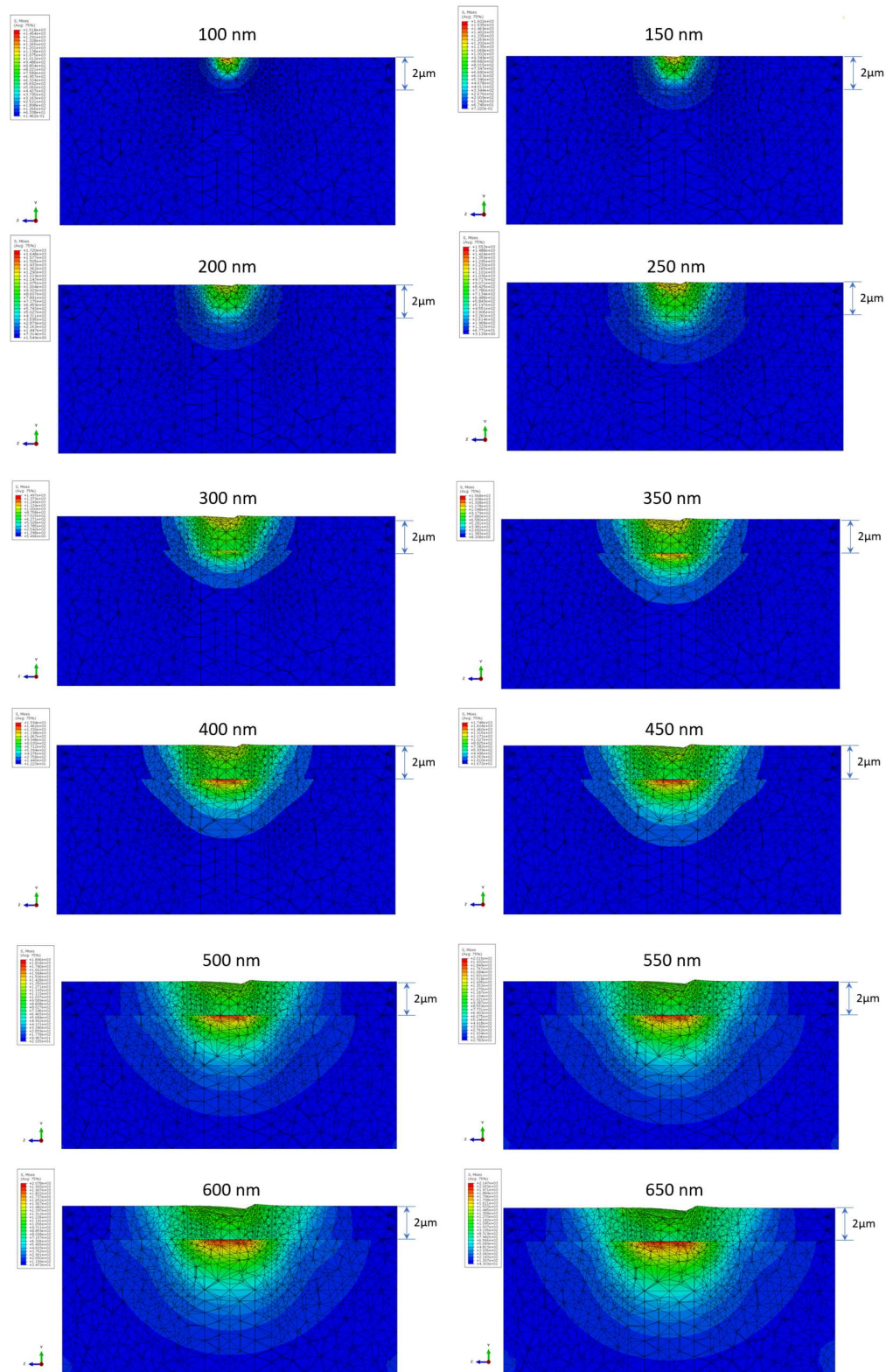
UNIVERSITAT POLITÈCNICA DE CATALUNYA
BARCELONA**TECH**
Escola d'Enginyeria de Barcelona Est

Figure 37. Cross-section of the cobalt-coated tungsten carbide substrate system at different indentation depths. Notice the size of the Von Mises stress with respect to the coating size.

UNIVERSITAT POLITÈCNICA DE CATALUNYA
BARCELONA**TECH**
Escola d'Enginyeria de Barcelona Est

A similar study was performed on a tungsten carbide film deposited over a cobalt substrate, the results of which are shown in Figure 38. The first difference with the curves obtained for the cobalt substrate is the magnitude of the load required by the indenter to penetrate the surface. Reason for this could be the greater elastic modulus of the reinforcement phase. Also, the loading step of the curves has a lower curvature compared to the ductile film previously shown, which could be connected with the lack of hardening behavior in the material law used for describing the plasticity of the carbide.
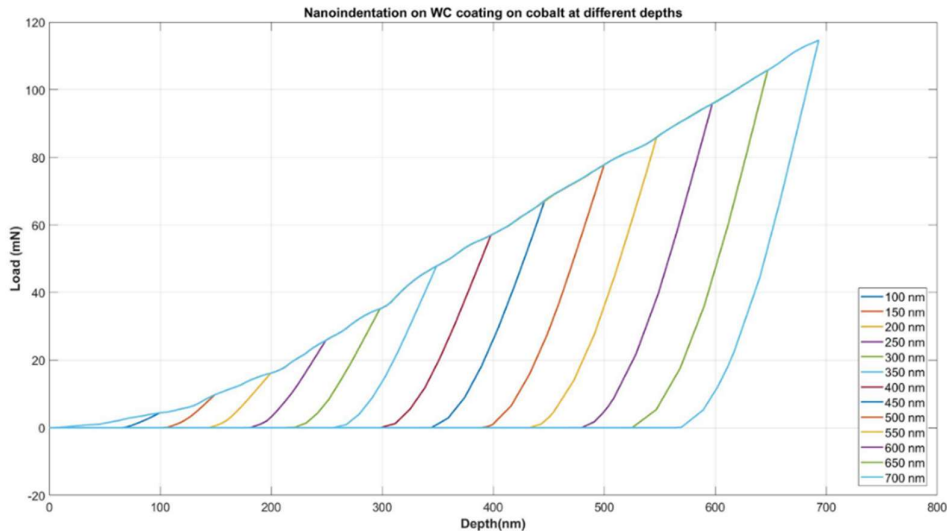
Figure 38. Nanoindentation load curves at different maximum depths on the WC-coated cobalt substrate.

Hardness and Young's modulus values were extracted from these curves and are plotted against maximum indentation depth in Figure 39. The elastic modulus lies in the range from 500 to 600 GPa until depths of 600 nm, after which a slight tendency towards lower values can be appreciated. Therefore, there seems to be little substrate influence in the results. Nonetheless, the evolution of hardness values with increasing indentation depth displays a substantially different and stronger trend. Hardness shows a steady and clear decrease after 350 nm, falling from 22 to 13 GPa. Notice that the first fall within the depth range of 100 to 150 nm is not taken into account as these depths are similar in magnitude to radius of the indenter tip (50 nm).

The evolution of hardness and elastic modulus with indentation depth on the hard coating follows the opposite trend as seen in the case of the cobalt coating. A possible explanation could be found in the stress distribution beneath the surface, which is shown in Figure 41 (see page 46). It can be seen that even at low indentation depths (around 300 nm) a considerable volume of the substrate is stressed. Given that the loads required to strain the carbide are considerably high, the substrate is subjected to large stresses well above their yield strength. This can be seen better in Figure 40, where the hard coating has been removed from the simulation output, so that the lower stresses that would be otherwise hidden by the larger values may be seen. Consequently, the

UNIVERSITAT POLITÈCNICA DE CATALUNYA
BARCELONA**TECH**
Escola d'Enginyeria de Barcelona Est

44

material beneath the coating is flowing plastically (Figure 40b), hence making it easier for the indenter to furtherly penetrate the surface. Notice from Figure 41 that the coating starts to bend after an indentation depth of 350 nm, revealing that the advance of the indenter is not due to carbide strain but rather to substrate yielding. As for the behavior of the elastic modulus, it could owe to the fact that until large indentation depths are reached, there is not a volume of substrate involved that is large enough to overcome the considerably larger magnitude of the carbide Young's modulus.
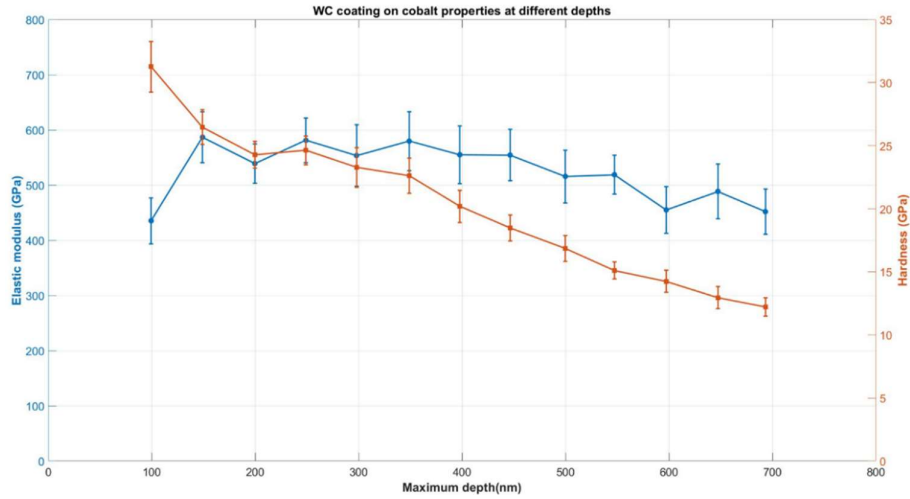
Figure 39. Elastic modulus (in blue) and hardness (in orange) values as function of maximum indentation depth on the WC-coated cobalt substrate.

a)
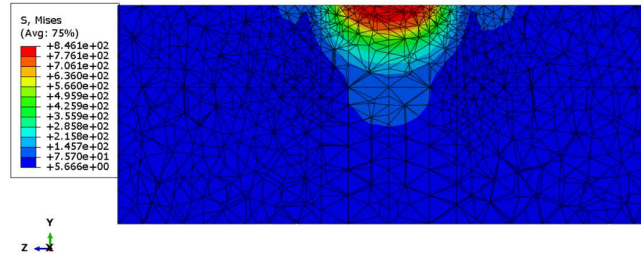
b)
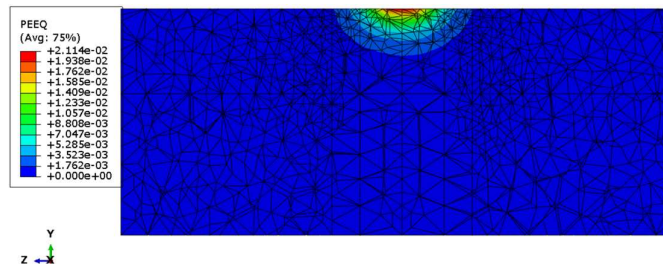
Figure 40. a) Stress and **b)** plastic strain distribution on the cobalt substrate at an indentation depth of 300 nm.
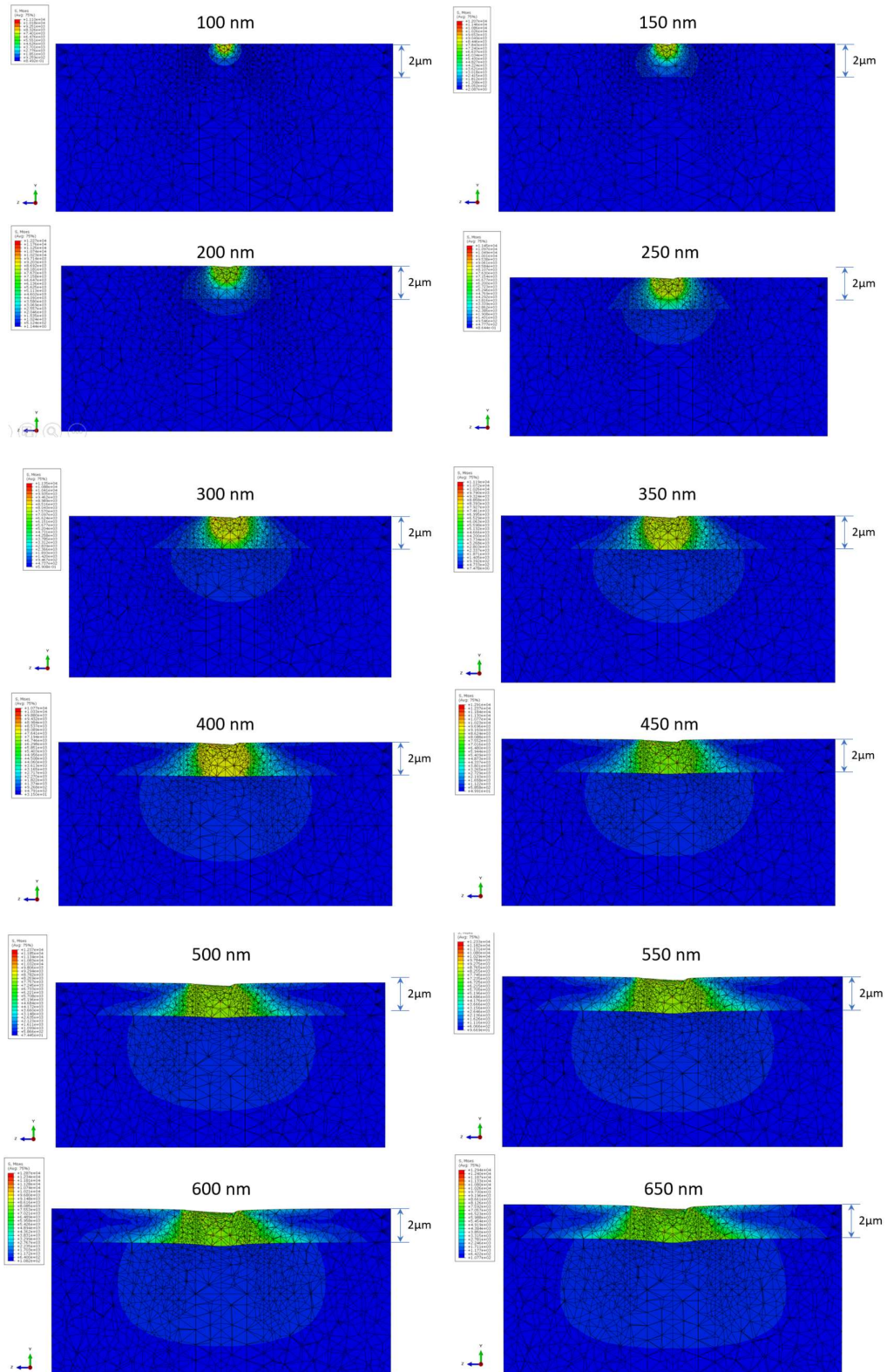
Figure 41. Cross-section of the cobalt substrate coated with tungsten carbide at different indentation depths.

Last but not least, elastic modulus values have been compared to the input parameter in order to assess how accurate the results are. It is not possible to do the same analysis with hardness values, because these values are not an input parameter. However, these results can be compared to experimental values taken from literature.[20] As a consequence, the obtained hardness data in both simulations are within experimental range. However, the hardness output on the cobalt coating seems to be in the lower limit of the experimental range. Reason for this could be the plastic curve used, since it was measured on pure cobalt, hence not accounting for constraining effects that in reality arise, as it was explained in the Literature Review. Moreover, crystal orientation was not considered in any possible way in these simulations, whereas it plays a significant role in the cited paper.

4.2.2.   Particle simulation at different indentation depths

The last verification step towards the ultimate model (i.e., the simulation of indentations on semispherical portions of a tomography embedded in an elastic matrix) comprised of nanoindentation simulations at increasing maximum depths on solid particles made of either cobalt or tungsten carbide embedded in the reciprocal hardmetal component (henceforward the *matrix*). Two meshes differing in matrix size (5.74 or 11.48 µm) were tested. To begin with, load curves as a function of corrected penetration depth on the cobalt particle embedded in a 'shorter' carbide matrix are shown in Figure 42. The maximum indentation depth was 450 nm because further values resulted in excessively large strains on the cobalt, thus preventing the simulation from converging to a final result.
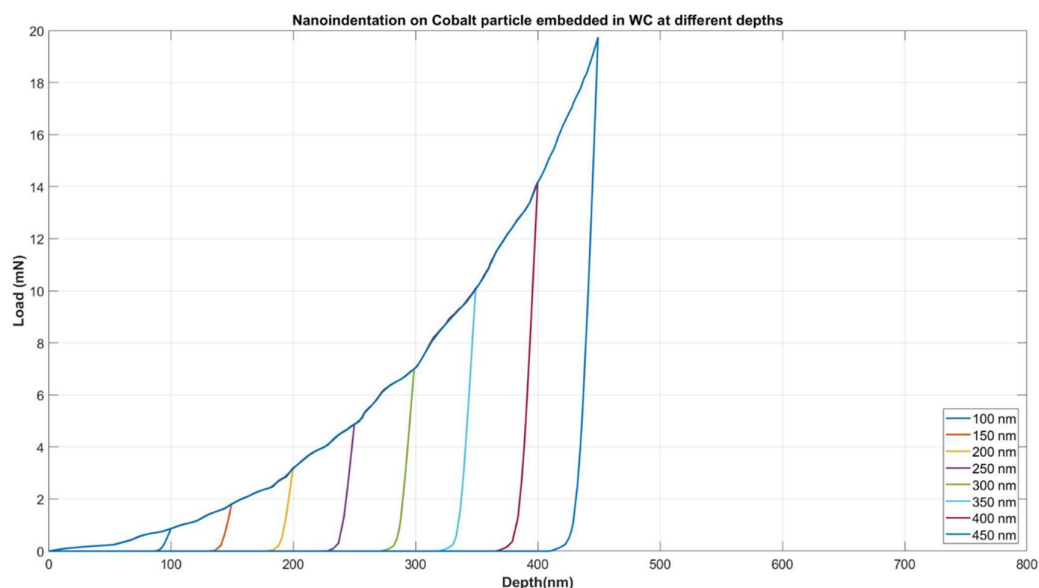

Figure 42. Indentation load as a function of corrected indentation depth at different maximum penetrations on the cobalt particle embedded in a 'shorter' carbide matrix.

Hardness values obtained in the nanoindentation of cobalt particles embedded in a 'shorter' carbide matrix are presented in Figure 43. The results do not show any differences to what was already obtained in both the homogeneous and coating analyses. It can be appreciated that hardness values start to rise after an indentation depth of 250 nm, which could mean that the substrate is exerting an influence on the results. A similar trend is also present in the elastic modulus at the same depth, as shown in Figure 44. Therefore, the rule of thumb regarding substrate influence after penetration depths greater than 10-15% is once again verified, as the particle is 2 µm in radius.
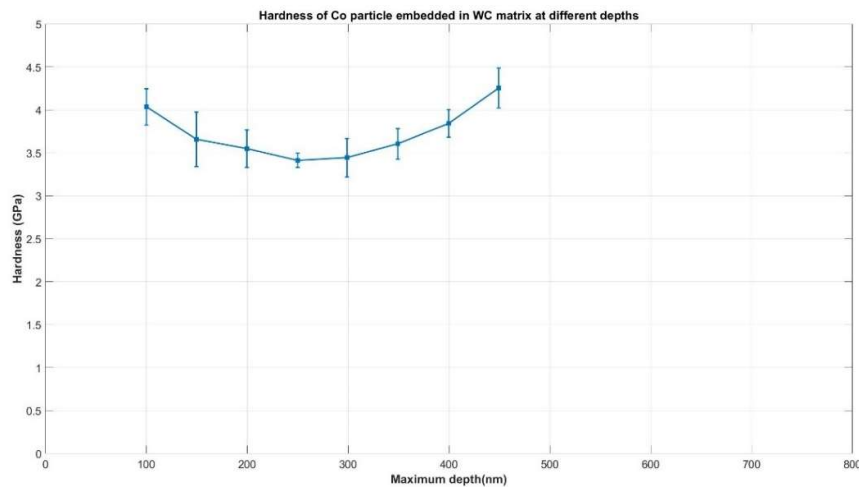

Figure 43. Hardness values obtained for the cobalt particle embedded in a 'shorter' WC matrix.
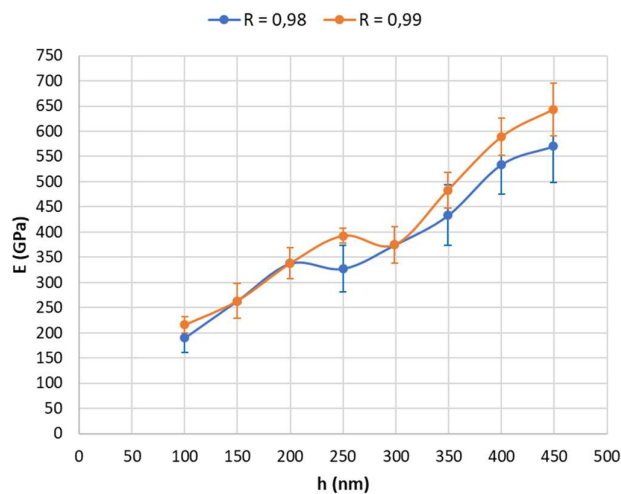

Figure 44. Elastic modulus of the cobalt particle embedded in a 'shorter' tungsten carbide matrix considering two R-square criteria.

As for the elastic modulus results, two estimation criteria based on R-squared value for the linear fit at the unloading stage are shown in Figure 44. In both cases, the results seem to be quite high, as the Young's modulus at an indentation depth of 200 nm is around 337 GPa regardless the

criterium used, while the input value was 230 GPa. Furthermore, the modulus at high indentation depths for an R-squared of 0.99 is 650 GPa, which is 50 GPa in excess of the input elastic parameter for the tungsten carbide. Therefore, the difference between the output and the input parameters does not seem to be related to the fitting criteria adopted.

A similar analysis was performed on a tungsten carbide particle embedded in a 'shorter' cobalt matrix. The results of these simulations are shown in Figure 46. In this case, the software could perform simulations at greater indentation depths, which could owe to the fact that the tungsten carbide has a substantially lower plasticity, thus resulting in smaller plastic strains, which makes the numerical convergence much easier. Two main aspects are quickly noticeable when comparing this graph to the one exposed in Figure 42, namely higher load values and a change in curvature. The former was clearly expected, given that the tungsten carbide is substantially harder and stiffer than the cobalt. The change of curvature, whose turning point seems to be at 300 nm of maximum indentation depth (green curve), could be an early sign of substrate influence.
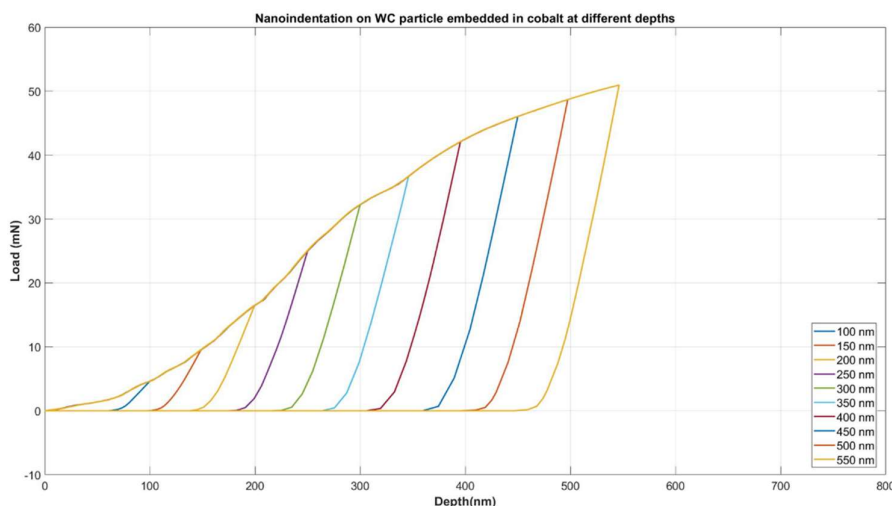

Figure 45. Indentation load as a function of corrected indentation depth at different maximum penetrations on the WC particle embedded in a 'shorter' cobalt matrix.

Hardness and elastic modulus results for this set of simulations are shown in Figure 46 and Figure 47 respectively. Hardness shows a continuous fall from 32 to 7 GPa, although there is a variation in slope after 200-250 nm, which could mean that the first two data points might be related to the influence of the indenter tip shape, while the softening after 200-250 nm could be due to the effect of the cobalt matrix. The elastic modulus data expose a similar trend, as the datum points in the range of 100 to 250 nm are within error range at around 550-600 GPa, but a clear softening down to 300 GPa is noticed at penetration depths greater than 250 nm. Nevertheless, both hardness and elastic modulus values at great depths are still higher than the corresponding cobalt values, hence verifying the stiffening trend that was already seen in the inverse analysis.
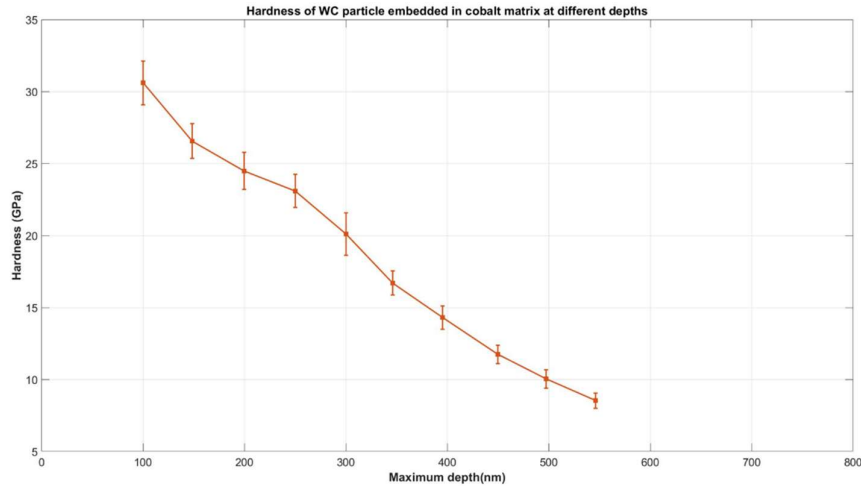
UNIVERSITAT POLITÈCNICA DE CATALUNYA
BARCELONA**TECH**
Escola d'Enginyeria de Barcelona Est

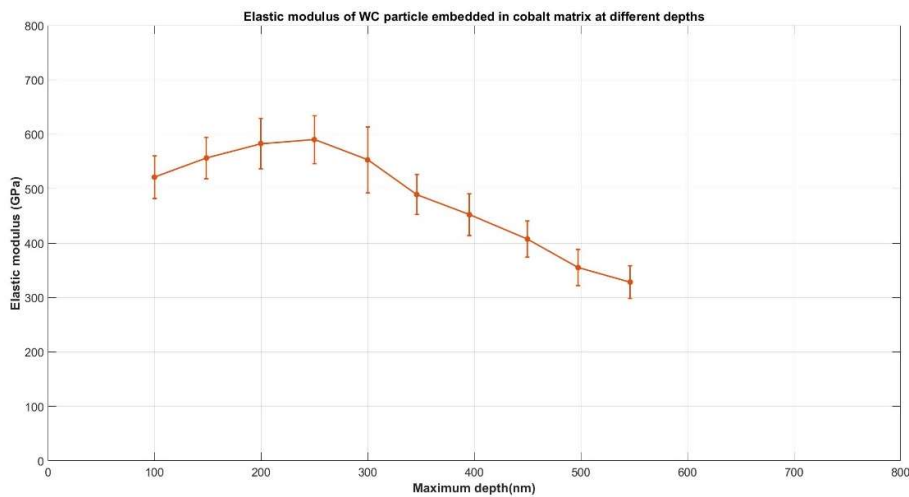**Figure 46.** Hardness values obtained for the WC particle embedded in a 'shorter' Co matrix.

Figure 47. Elastic modulus of the WC particle embedded in a 'shorter' cobalt matrix.

A better understanding of the situation can be achieved by analyzing the stress distributions at different penetration depths and comparing them with the coating results at equivalent depths, as depicted in Figure 48. The stress in the gray areas is out of scale (the threshold was set at 100 MPa and 500 MPa in the cobalt and tungsten carbide particles respectively), as it would otherwise conceal the results in the less stressed areas that are of interest. In the case of the particle analyses, it can be noticed that the stresses in the vicinity of the matrix lower boundary are at least an order of magnitude greater than in the corresponding coating case. Given that the displacement constraints in the matrix are set in its lower boundary, the fact that there are stressed areas in its surroundings could imply that the boundary condition is actually exerting an influence in the results. In fact, as the whole test is displacement-controlled, this influence may translate in higher indentation loads for the same displacement compared to the coating case, thus increasing the stiffness of contact (S), which in turn results in greater elastic modulus values.
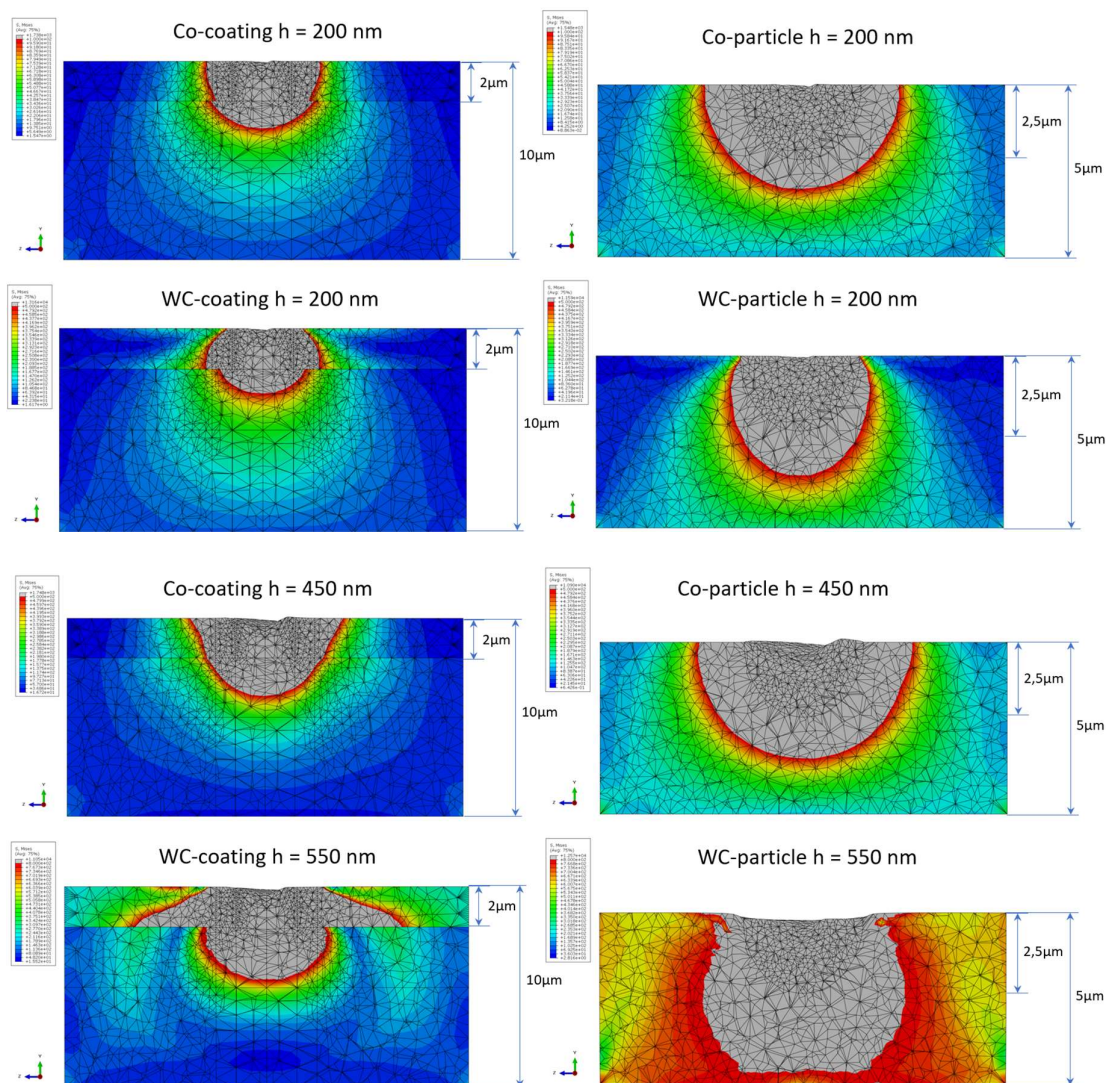
Figure 48. Comparison between stress distributions obtained on the coating system (left) and the ones obtained on the particle embedded in the 'shorter' mesh (right).

These conclusions led to the analysis of larger matrixes, so that the constrained areas were not subjected to stresses that could imply a larger contact stiffness as explained above. Then, a similar analysis was performed using samples consisting of particles (either WC or Co) surrounded by a complementary matrix which was 11,48 µm height. Figure 49 shows the P-h curves obtained by simulating the nanoindentation of cobalt particles. These results are quite similar to the ones depicted in Figure 42 both in curve shape and magnitude. Therefore, the use of a 'shorter' matrix does not necessarily increase the indentation load as it was previously thought. Meanwhile, the corresponding hardness values are shown in Figure 50. These results show little differences to what was already obtained for the 'shorter' matrix analysis. For example, hardness starts to increase after an indentation depth of 250 nm, which could mean that the substrate is exerting an influence on the results.
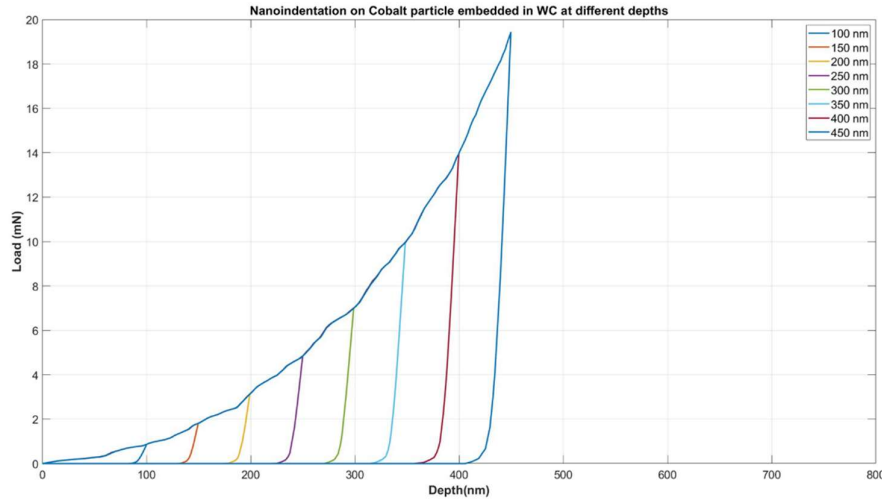
UNIVERSITAT POLITÈCNICA DE CATALUNYA
BARCELONA**TECH**
Escola d'Enginyeria de Barcelona Est

Figure 49. Indentation load as a function of corrected penetration depth at different maximum penetrations on the cobalt particle embedded in a 'larger' carbide matrix.
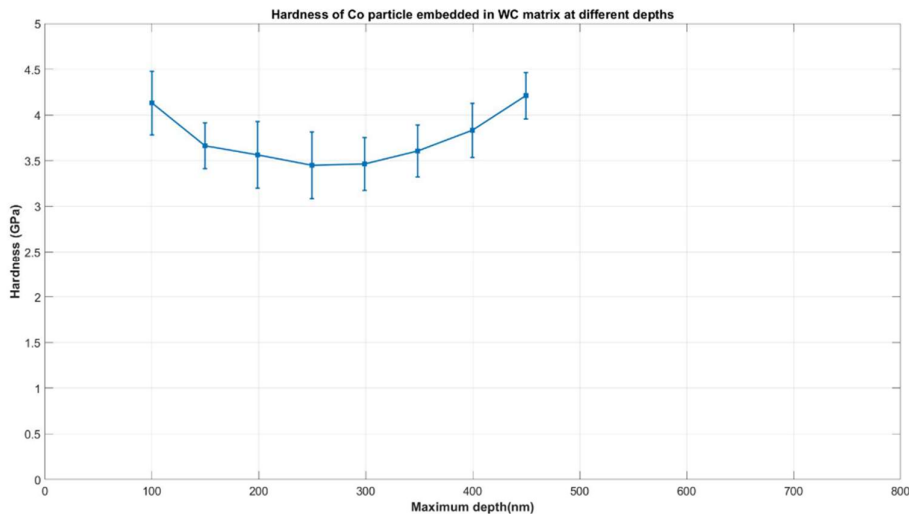

Figure 50. Hardness values at several penetration depths obtained from a cobalt particle embedded in a 'larger' WC matrix

However, there are some noticeable differences when comparing the elastic modulus data obtained by indenting the shorter and larger sample, as shown in Figure 51. In these graphs both moduli attained using two R-squared criteria are shown. The differences in the results are not clear when using a criterium of R=0.99, but it becomes more explicit when fitting the unloading curves applying a R-squared of 0.98. In this case, the results are below 300 GPa down to 250 nm, thus being consistent with the results obtained for coatings. In fact, the indentation at 200 nm is actually around the input value of 230 GPa when considering the associated error. Moreover, the results of the 'larger' matrix simulations at deeper penetrations result in lower Young's moduli than the tungsten carbide matrix input value (600 GPa) regardless the criteria, while the 'shorter' matrix outcome was above that parameter.
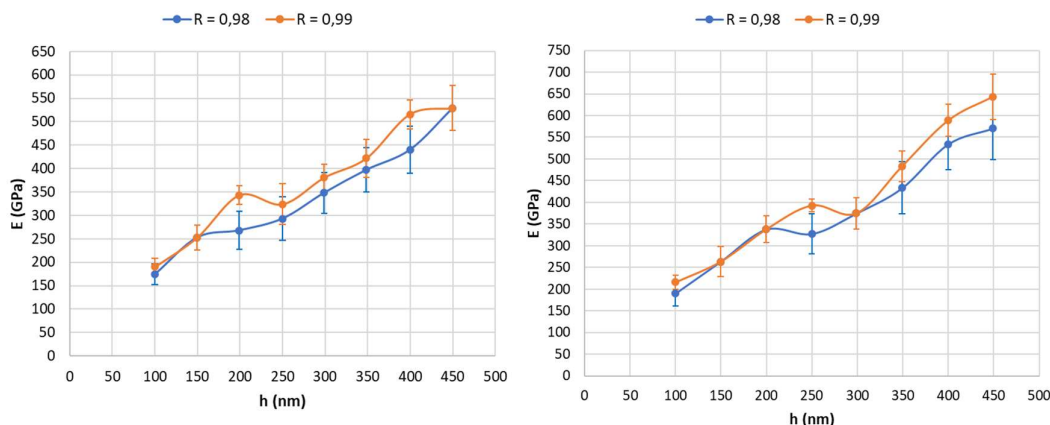
UNIVERSITAT POLITÈCNICA DE CATALUNYA
BARCELONA**TECH**
Escola d'Enginyeria de Barcelona Est

Figure 51. Elastic modulus data as a function of maximum indentation depth on a cobalt particle embedded in a 'larger' WC matrix (left) and the one obtained for a 'shorter' matrix (right).

As regards the tungsten carbide particles surrounded by a 'larger' cobalt matrix, the load curves as a function of indentation depth are presented in Figure 52. Once again, the results are quite similar to the ones obtained in the 'shorter' matrixes (see Figure 45). There are no noticeable changes in load magnitude and the curvature seems to follow the same trend. In addition, hardness data depicted in Figure 53 shows little differences with the results that were previously obtained and presented in Figure 46. For example, hardness at 550 nm depth is around 7 GPa in both cases. Given that there are data points at deeper penetrations, it is now possible to appreciate hardness values near to 5 GPa, which are in the range of the cobalt hardness so far estimated.
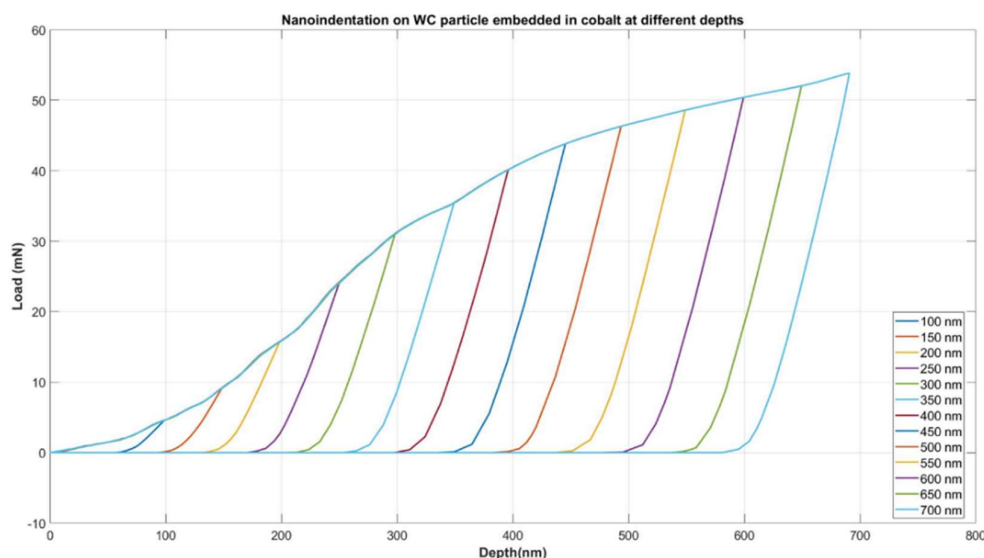

Figure 52. Indentation load as a function of corrected indentation depth at different maximum penetrations on the tungsten carbide particle embedded in a 'larger' cobalt matrix.
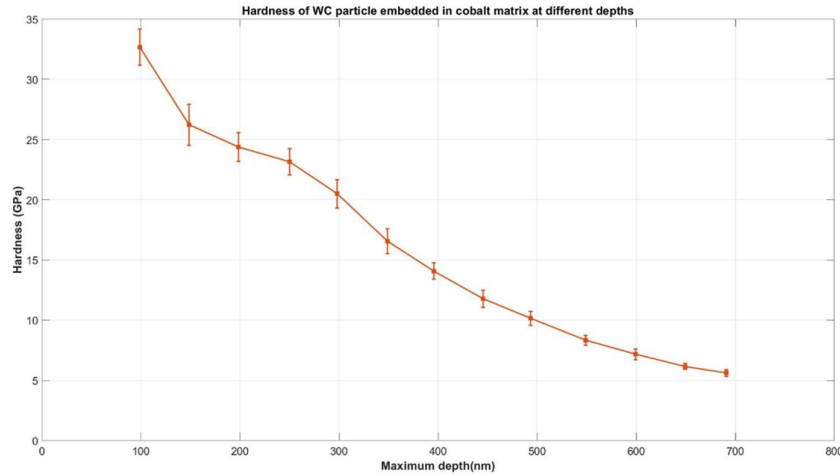
UNIVERSITAT POLITÈCNICA DE CATALUNYA
BARCELONA**TECH**
Escola d'Enginyeria de Barcelona Est

Figure 53. Hardness data obtained from indenting a WC particle surrounded by a 'larger' Co matrix.

Meanwhile, the elastic modulus registered on the simulation of WC particles show a clear improvement when using a 'larger' matrix compared to the 'shorter one'. Figure 54 contains elastic moduli at different penetrations calculated using the two R-squared criteria previously detailed, although there does not seem to be substantial differences in the results obtained with either criterium. However, Young's moduli at deep penetrations are much closer to the input value of 230 GPa, thus supporting the fact that in the 'shorter' matrix there were boundary effects that exerted an influence in the results. For instance, at 550 nm deep the elastic modulus in the WC particle embedded in a 'shorter' matrix was around 350 GPa, while in the 'larger' case it lies in the vicinity of 250 GPa, which is much closer to the input parameter. Lastly, the onset of softening due to substrate influence seems to be after 250 nm, which can also be seen in the hardness evolution with increasing indentation depth as shown before in Figure 53.
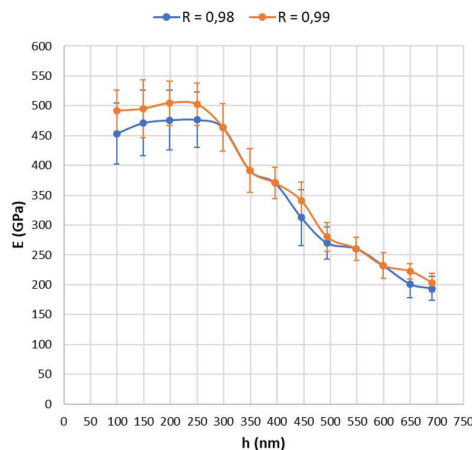

Figure 54. Elastic modulus of the WC particle embedded in a 'larger' Co matrix.

The stress field in the larger-matrix samples was also plotted at different depths and compared to the equivalent coating analysis, as it can be seen in Figure 55. As it was done in Figure 48, an upper limit of 100 MPa and 500 MPa was set for both Co and WC particles respectively. There is a fairly good agreement between the two set of simulations at a given depth, despite the fact that at deeper penetrations there are differences in the stress distributions that are related to the variances in shape between the particle and the coating. The stress propagation in the particle model is much symmetric, as it can be expected when considering the overall geometrical symmetry. Moreover, stresses in the larger matrix were much lower than in the 'shorter' one, which could again be a boundary effect. Indeed, the lower boundary surroundings in the embedded-particle model seem to be free of stresses even at indentations of great magnitude.
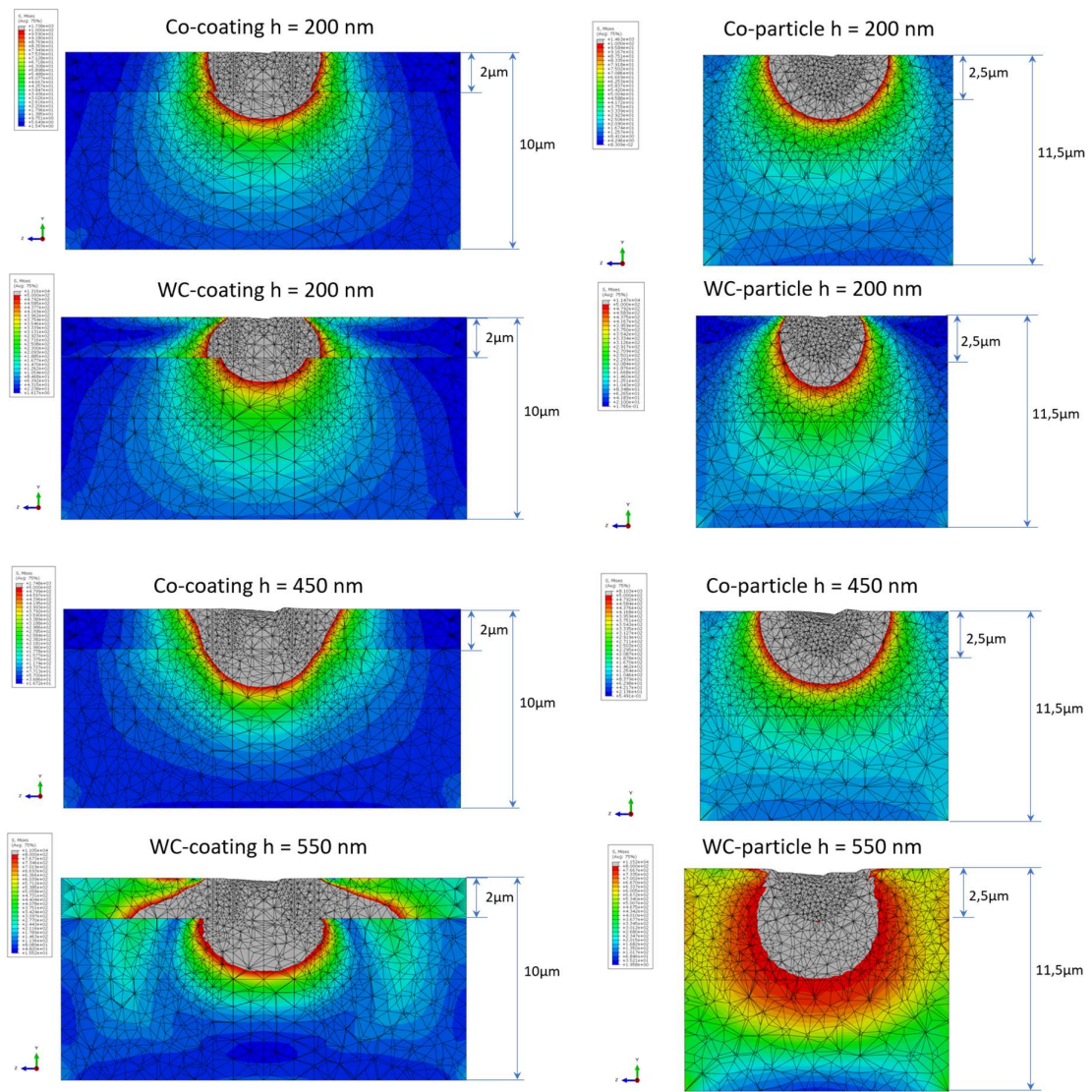

Figure 55. Comparison between stress distributions obtained on the coating system (left) and the ones obtained on the particle embedded in the 'larger' mesh (right).

UNIVERSITAT POLITÈCNICA DE CATALUNYA
BARCELONA**TECH**
Escola d'Enginyeria de Barcelona Est

To conclude, the use of a large mesh is highly recommended for the following simulations involving a domain embedded in a larger matrix. Indentations down to maximum penetrations of 250 nm do not show substrate influence neither in hardness nor in elastic modulus values. Elastic modulus data can vary considerably with the R-squared criterium used for its calculation. It seems that results obtained using a criterium of R=0.98 are more consistent with the input parameters, which could be due to a greater number of data points involved in the calculation. Hence, a smaller numerical step should be used in further calculations so that there are more data points at all indentation stages. The proposed model also works fairly well when applied to coated systems and the results yielded are comparable with previous publications. In addition, the stress distribution in the particle model is much more symmetric than in the coating model.

4.3. Adjustment of material models to the microstructure

4.3.1. Use of Co plastic curve without considering Hall-Petch effect

A great advantage of the FEM simulations is the possibility to plot stress and strain distributions on the sample. Figure 56 depicts the Von Mises stress distribution in the cobalt phase within some of the samples carved out of the tomography upper surface. It can be seen that a considerable portion of the phase is under high stresses, as the green regions are well within the plastic range (around 900 MPa). On the contrary, their WC complements shown in Figure 57 present more limited stress distributions. In addition, the stresses are one order of magnitude higher than their counterparts in the cobalt phase, which seems logical as the Young's modulus of the tungsten carbide is much higher than the binders'.
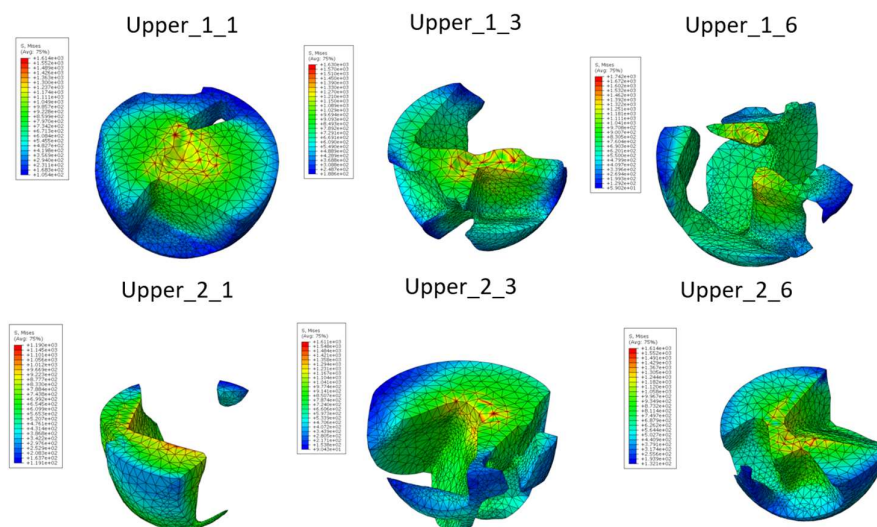

Figure 56. Portions of the cobalt phase displaying a color map of Von Mises stress distribution obtained when the maximum load was applied.

UNIVERSITAT POLITÈCNICA DE CATALUNYA
BARCELONA**TECH**
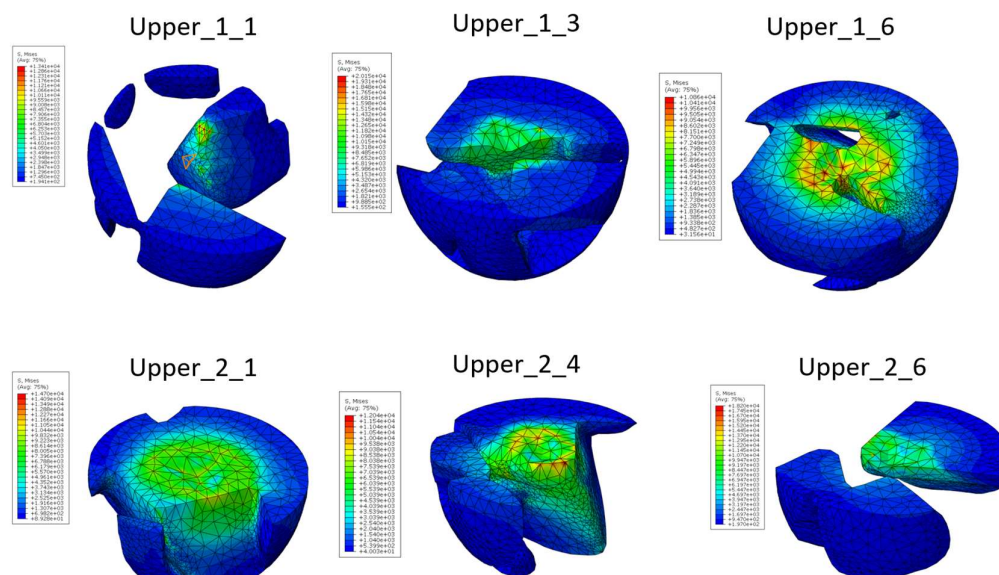Escola d'Enginyeria de Barcelona Est

Figure 57. Portions of the tungsten carbide phase displaying a color map of Von Mises stress distribution obtained when the maximum load was applied.

A similar analysis considering the plastic strain distribution was performed over the same samples, as presented in Figure 58 and Figure 59. It is possible to notice a clear indentation footprint, especially when the contact occurred mainly on one of the phases (e.g. on the cobalt of sample Upper_1_1 and on the WC phase of Upper_2_1). As for the magnitude of the plastic strain, it is substantially higher in the binder regions than in the reinforcement, as expected.

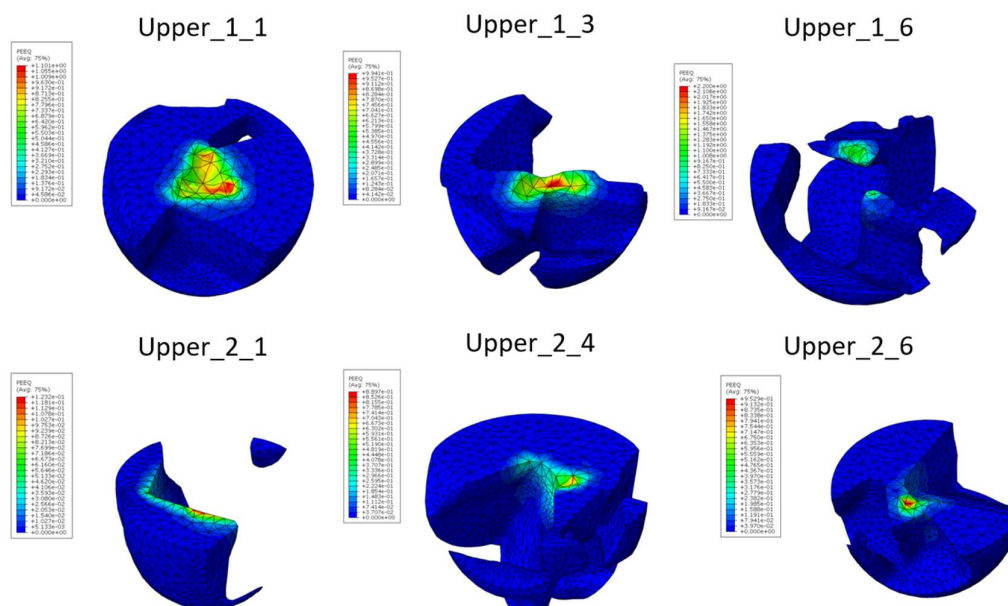

Figure 58. Portions of the cobalt phase displaying a color map of equivalent plastic strain distribution obtained when the maximum load was applied.
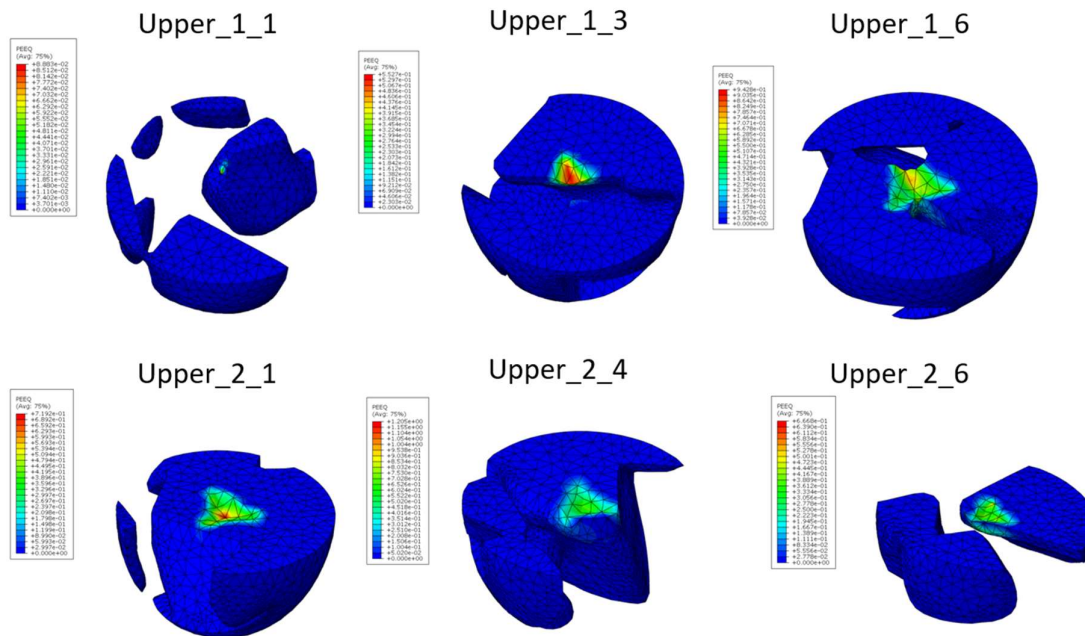
UNIVERSITAT POLITÈCNICA DE CATALUNYA
BARCELONA**TECH**
Escola d'Enginyeria de Barcelona Est

Figure 59. Portions of the tungsten carbide phase displaying a color map of equivalent plastic strain distribution obtained when the maximum load was applied.

Figure 60 shows the *P-h* curves obtained for the tomography domains embedded in the matrix of average properties. In this case, the plastic model used for modelling the cobalt behavior remained unchanged from previous analysis. It can be appreciated that there is a great variation in the maximum load achieved, as it oscillates between 3 and 16 mN. Given the difference in phase arrangement, this dispersion in value seems reasonable, as the indenter can be either in contact with a tungsten carbide or with a cobalt portion or with a domain comprising of both of the constituents.

a)

UNIVERSITAT POLITÈCNICA DE CATALUNYA
BARCELONA**TECH**
Escola d'Enginyeria de Barcelona Est
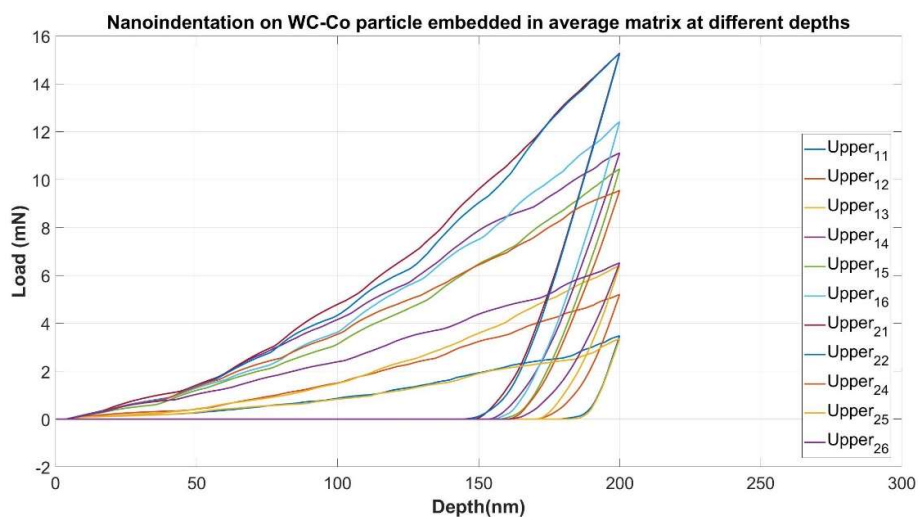
b)

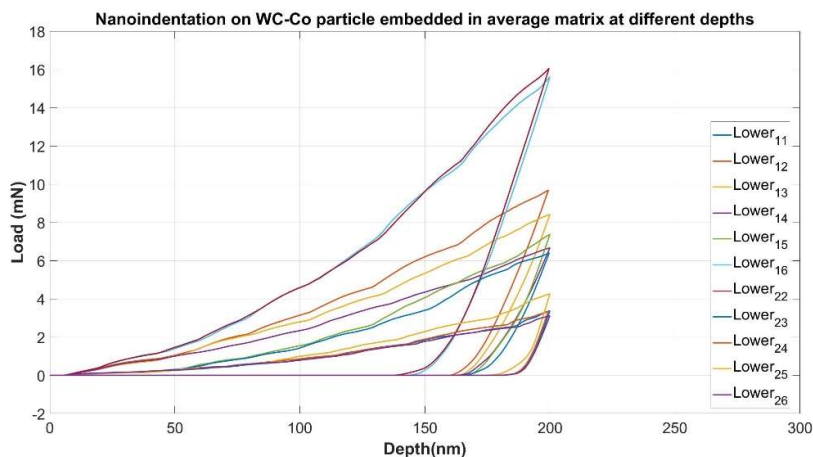**Figure 60.** Load curves as a function of maximum penetration for the samples taken from the **a)** upper and **b)** lower faces of the tomography.

Elastic modulus and hardness values were extracted using the same algorithm as in the case of coating and homogeneous particles. However, in this case the results correspond to a unique maximum depth, which is why the data was statistically processed in histograms as shown for the Young's moduli in Figure 61. Notice that the distribution seems to be shifted to lower-magnitude moduli, in particular around 300 GPa, although there is a significant fraction that is near 500 GPa, meaning that in those cases there was more tungsten carbide present and vice versa. Moreover, 10% of the data points are close to 250 GPa. Not only does this mean that cobalt is likely to be a dominant phase in the embedded domain, but it also shows that the whole model is working properly as the results are close to the input parameter (230 GPa). The same analysis could be done on the opposite side of the distribution, which seems to depict a fair modelling of the carbide elastic modulus. Lastly, the data presented was calculated using an R-squared criterium of 0.98, as it had previously shown to be the most reliable.
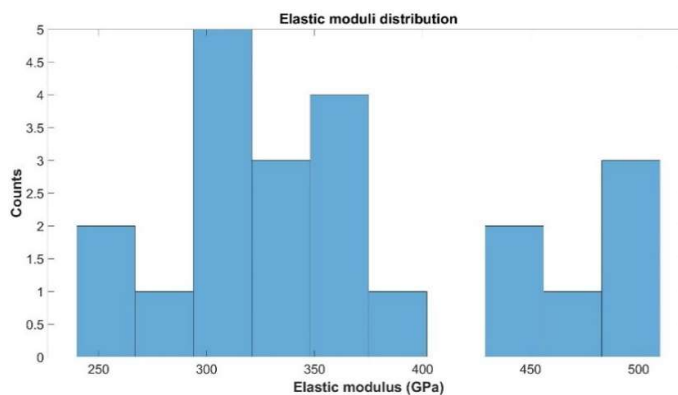

Figure 61. Statistical distribution of elastic modulus values resulting from the P-h curves obtained from the upper and lower portions of the tomography.

UNIVERSITAT POLITÈCNICA DE CATALUNYA
BARCELONA**TECH**
Escola d'Enginyeria de Barcelona Est

59

The analogous statistical distribution for hardness values is shown in Figure 62. A clear shift towards low hardness values in between 3 and 5 GPa can be seen, showing a similar trend as in the case of the elastic modulus. There is also a significant number of samples around 7.5 GPa, followed by a 14% of data points that laid in the vicinity of 22 GPa. Comparing these results to a distribution that was experimentally obtained by Roa et al.[19] and shown in Figure 63, it can be noticed that the numerical output is too much shifted to the lower spectrum. This could be due to the fact that the number of simulations is too low, so that the sampling is not representative enough. Besides, the plastic model used does not consider the strengthening effect exerted by the Hall-Petch mechanism that is experimentally verified. Finally, the highest hardness values obtained in the simulations fall short to the extreme ones encountered in reality (around 30 GPa), although in reality this could be due to less favorable crystal orientations that result in a large Schmid's factor, while the simulation does not account for crystallographic orientations.
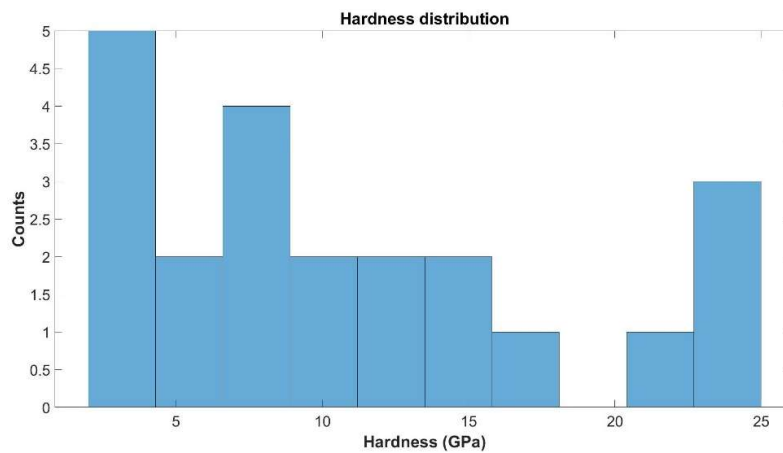

Figure 62. Statistical distribution of hardness values resulting from the P-h curves obtained from the upper and lower portions of the tomography.
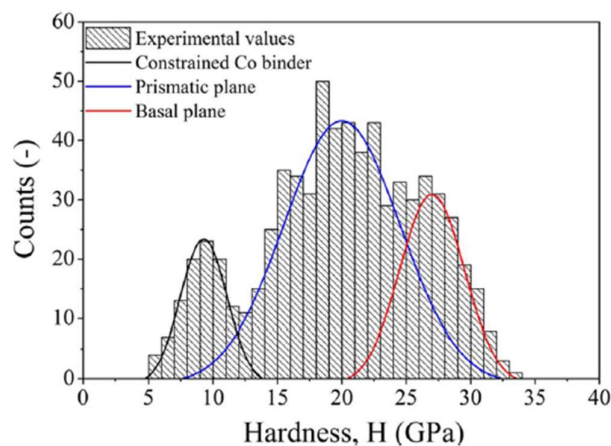

Figure 63. Hardness distribution experimentally measured on thick cobalt binder by Roa et al.[19]

UNIVERSITAT POLITÈCNICA DE CATALUNYA
BARCELONATECH
Escola d'Enginyeria de Barcelona Est

4.3.2. Consideration of Hall-Petch effect

In order to get a hardness distribution that better resembles the one that was experimentally measured, the plastic model in the cobalt phase was changed. Therefore, the plastic curve was shifted to a higher yield strength obtained by applying a Hall-Petch approximation. The P-h data attained using this model is presented in Figure 64. A slight shift towards higher load values is appreciated when comparing this outcome to the curves depicted in Figure 60. For instance, the lowest value of maximum load is now well above 4 mN, whereas it was around 3 mN when the original plastic curve was used. Besides, a great variation in these peak forces is found in this case, thus reinforcing the hypothesis that it is likely related to phase arrangement.

a)
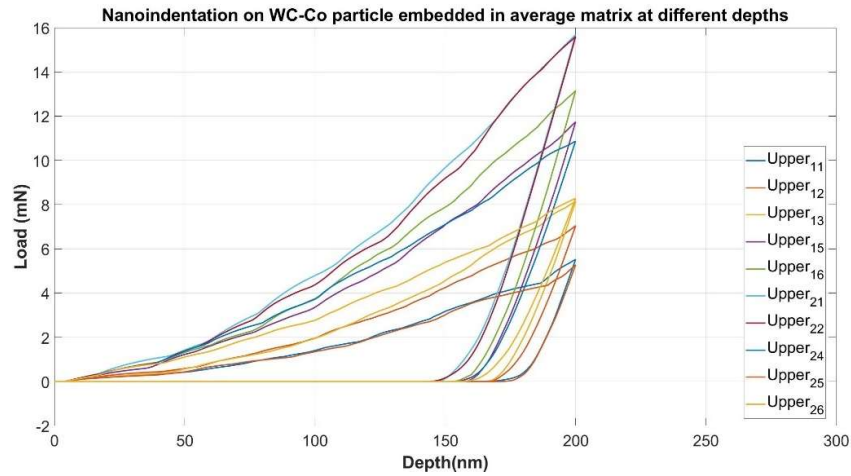
b)

Figure 64. Load curves as a function of indentation depth on samples taken from the **a)** upper and **b)** lower faces of the tomography considering the Hall-Petch strenghtening.

UNIVERSITAT POLITÈCNICA DE CATALUNYA
BARCELONA**TECH**
Escola d'Enginyeria de Barcelona Est

61

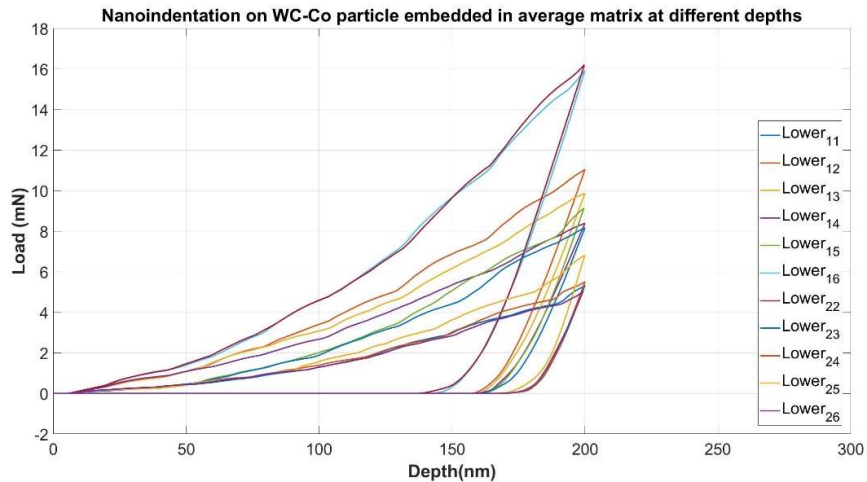Elastic modulus data was obtained from the P-h curves and plotted in the histogram shown in Figure 65. The results are quite similar to the ones calculated using the original plastic curve, which seems reasonable as the only difference is in the plastic model, hence it should not affect the elastic unloading step. However, there are subtle differences as presented in Figure 66, where the values attained using both plasticity models are depicted, while the percentual difference between them is plotted with a yellow line. The differences vary up to more than 12% and it seems that the highest variances occur in samples with a lower Young's modulus, which is reasonable as in these samples there is more cobalt, hence the changes in the plasticity model have a greater impact.

Figure 65. Statistical distribution of elastic modulus values resulting from the P-h curves using a modified plastic curve with a Hall-Petch model.
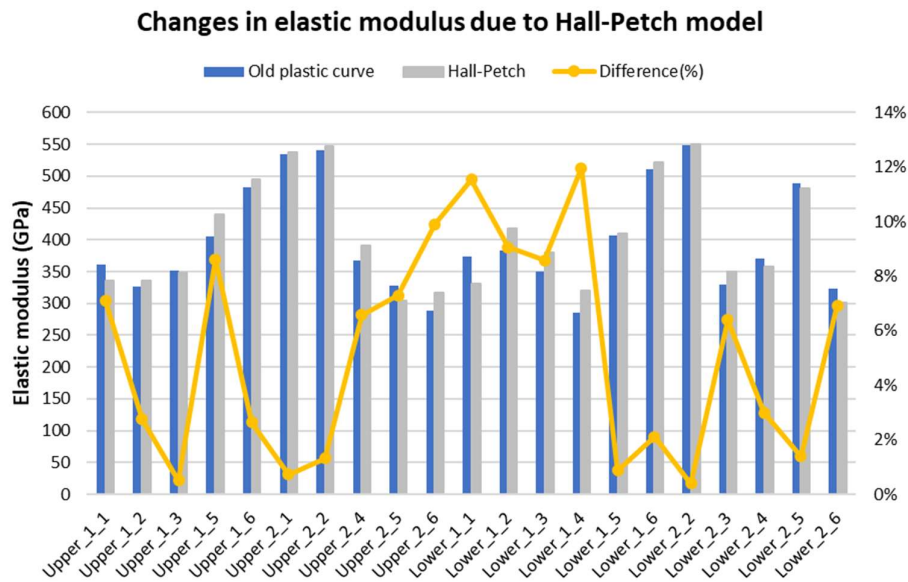
Figure 66. Comparison between the Young's modulus values obtained with and without Hall-Petch modification. The yellow line indicates the percentual difference.

UNIVERSITAT POLITÈCNICA DE CATALUNYA
BARCELONA**TECH**
Escola d'Enginyeria de Barcelona Est

Hardness was also calculated and the resulting distribution is plotted in Figure 67. At first glance, this output seems quite similar to the results attained by means of the original plastic curve (see Figure 62, on page 60). Nevertheless, hardness data are shifted towards higher values, as the introduction of the Hall-Petch strengthening has raised the minimum hardness from the range between 3 and 5 GPa to a window of 6 to 8 GPa. Maximum hardness data increases a little bit from 22.5 to 24 GPa, although it is more concentrated in this value than in the previous case. Despite this shift to higher hardness values, the statistical distribution does not fulfill the trend that is experimentally observed.
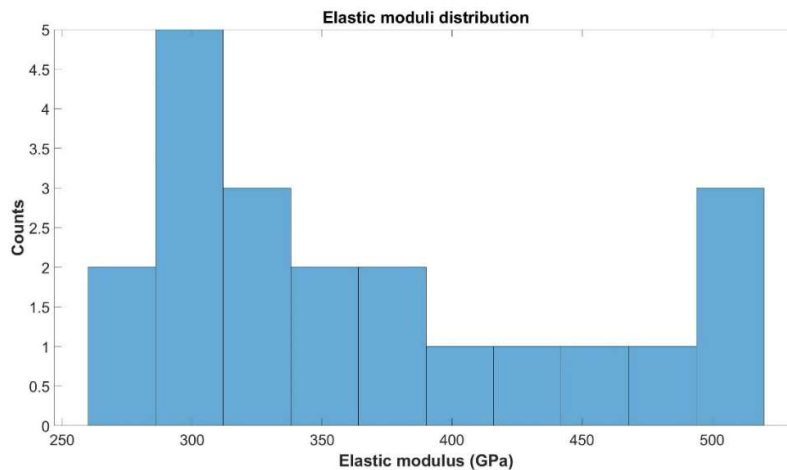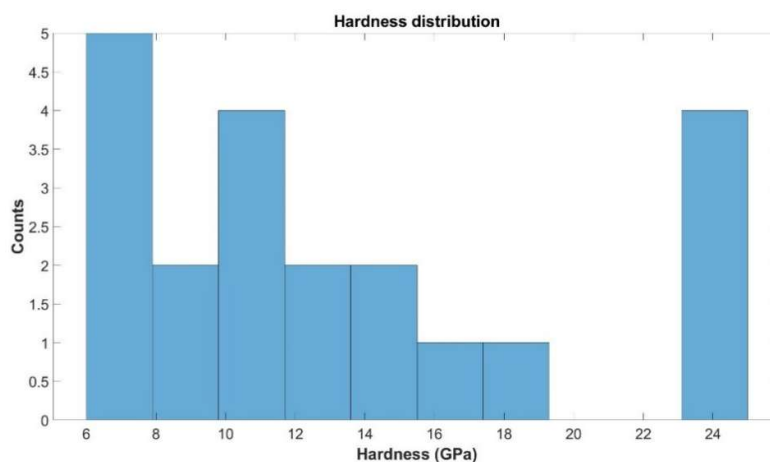

Figure 67. Statistical distribution of hardness values resulting from the P-h curves using a modified plastic curve with a Hall-Petch model.

The differences between the two models were analyzed in the same way as the variations in elastic moduli. Figure 68 shows the hardness values attained using either the original plastic curve or the one modified with the Hall-Petch strengthening. The percentual difference is once again expressed using a line, which exhibits that the use of the Hall-Petch model increases hardness values up to 70%. The largest impact is again more evident in softer samples, which could be due to a larger cobalt fraction in the tomography domain. Given that the introduced modification affected only the binder phase, it is reasonable that the larger variations occur in samples where it is the dominant component.

In summary, the simulation output is considerably sensitive to the plasticity model applied to the cobalt phase. The introduction of Hall-Petch strengthening exerts an important influence on the cobalt domains by making them substantially harder. However, the statistical distribution does not agree with the experimental outcome, as the majority of the simulated results are much softer.

Figure 68. Comparison between the hardness outcome obtained with and without Hall-Petch modification. The yellow line indicates the percentual difference.

4.3.3. Crystal plasticity model with Hall-Petch shift

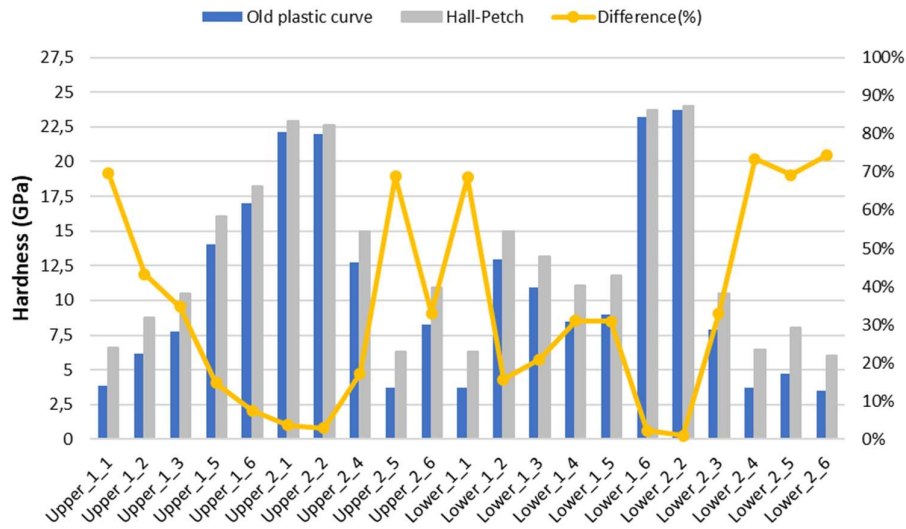Plastic behavior was finally modeled using a crystal plasticity subroutine. The resulting load curves as a function of indentation depth are presented in Figure 69. An overall but slight increase in maximum indentation load is appreciated when comparing these curves with their Hall-Petch counterparts shown in Figure 64. For example, the lowest value of maximum indentation load with the crystal plasticity model is around 6 mN, while the lowest output of the previous model was well below that value. A similar behavior is observed in the highest values of the maximum load, which go beyond 16 mN in the crystal plasticity model, but falls short to that value when a Hall-Petch-strengthened plastic curve is used, although it remains close.

The elastic moduli corresponding to each curve were calculated using the 0.98 R-squared criterium and are shown in Figure 70 as a statistical distribution. In this case, the results are more distributed than in the two previous studies, as there are more domains within intermediate values in the window of 350 – 400 GPa. It seems that this shift to middle magnitudes has occurred at the expense of the lower moduli, since the count in the vicinity of 300 GPa has fallen from 5 to 3. Meanwhile, the number of high-modulus samples has remained unchanged, as well as the domains comprising mostly of cobalt. Given the low quantity of data points and the slight shifts observed, the elastic modulus data gives insufficient information to draw any conclusions. Nonetheless, the crystal plasticity model should have little effect on the elastic behavior.

UNIVERSITAT POLITÈCNICA DE CATALUNYA
BARCELONATECH
Escola d'Enginyeria de Barcelona Est
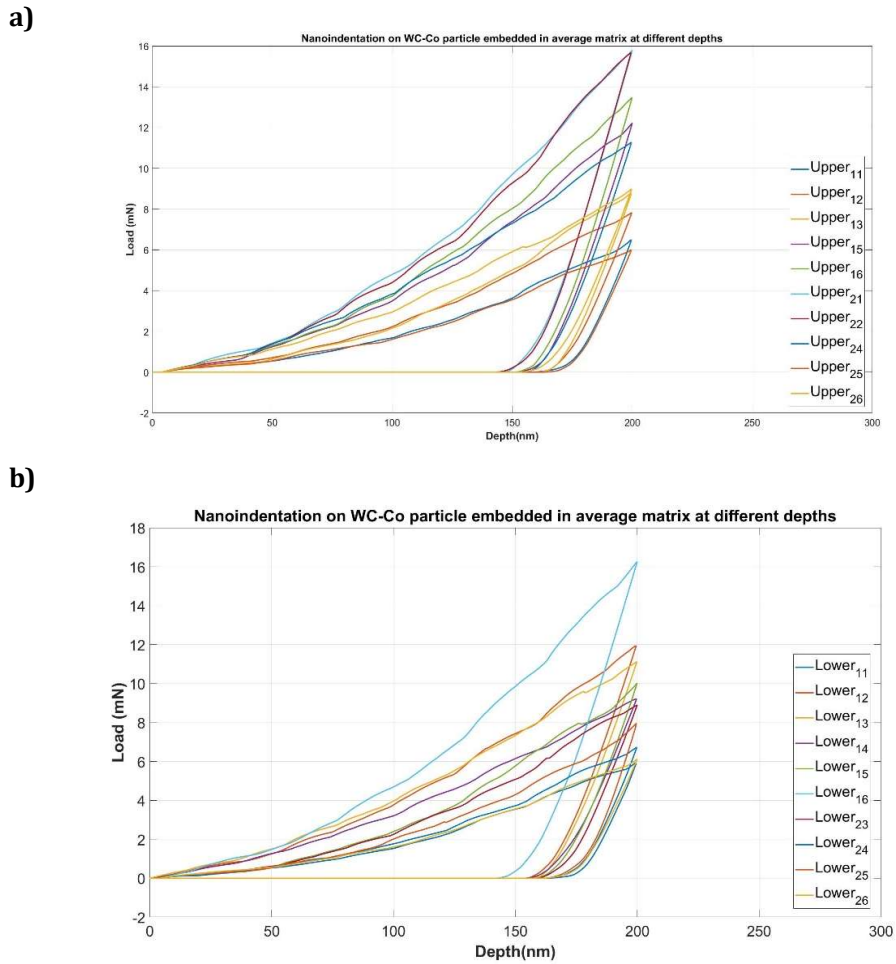
a)

b)

Figure 69. Load curves as a function of indentation depth on samples taken from the **a)** upper and **b)** lower faces of the tomography modelled with a crystal plasticity.
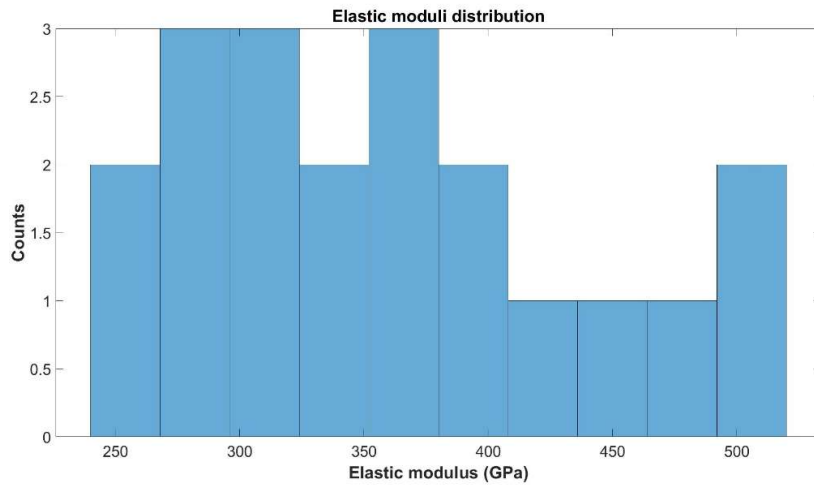

Figure 70. Elastic moduli distribution attained using a crystal plasticity model.

UNIVERSITAT POLITÈCNICA DE CATALUNYA
BARCELONA**TECH**
Escola d'Enginyeria de Barcelona Est

The hardness response to the variation in the plastic model can be appreciated in Figure 71. At first glance, there has been a shift in the lower end of the distribution towards higher values if compared to the outcome of the previous models. Consequently, the minimum hardness value was 8 GPa, while in the original and Hall-Petch cases were 3 and 6 GPa respectively. Besides, the data obtained cover almost the entire hardness spectrum up to 26 GPa, which is the hardest value so far attained. However, the maximum counts remain at the lowest hardness values as it has occurred in the previous cases.

On the other hand, in this distribution there are some subtle differences to the two preceding ones. The majority of data points fall at values higher than 10 GPa, which was a boundary value attributed to the cobalt phase in the analysis performed by Roa et al.[19] Hence, it could be assumed that higher hardness values account for some sort of carbide influence. As the majority of the samples are harder than 10 GPa, the probability of the indenter encountering a carbide phase is higher than finding mere cobalt. Therefore, the trend that is experimentally found and shown in Figure 63 (see page 60) is somewhat kept by the simulations using a crystal plasticity model. Nevertheless, it would be interesting to run a greater number of simulations on other locations to verify this analysis.
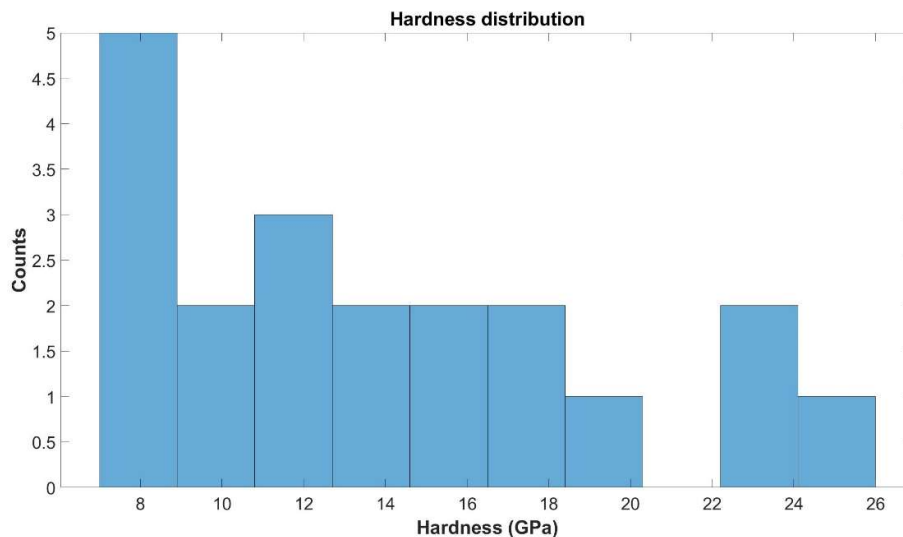
Figure 71. Hardness distribution attained using a crystal plasticity model.

Experimental data supplied by another member of the CIEFMA group was compared to the simulated results, as exposed in Figure 72. Given that there is a large dispersion in simulated outcomes, sample 'Lower_1_6' was chosen as the comparison champion, because it is the most similar curve. Then, the resulting P-h curves attained with the three plastic models are plotted. Initially, the simulated curves and the experimental one fit well with one another. However, the experimental curve departs from the rest with increasing tip displacement, since it shifts to higher load values. Moreover, the experimental hardness value for this sample was 27 GPa, which is out

of the experimental scale. Nevertheless, this was to be expected because the tungsten yield strength was defined using the Tabor rule considering a hardness of 25 GPa. Meanwhile, the similarity between the three models owes to the fact that the tungsten carbide is the dominant phase in this domain, as it can be appreciated in Figure 73. Hence, the plastic model applied to the cobalt phase exerts little influence in the results.
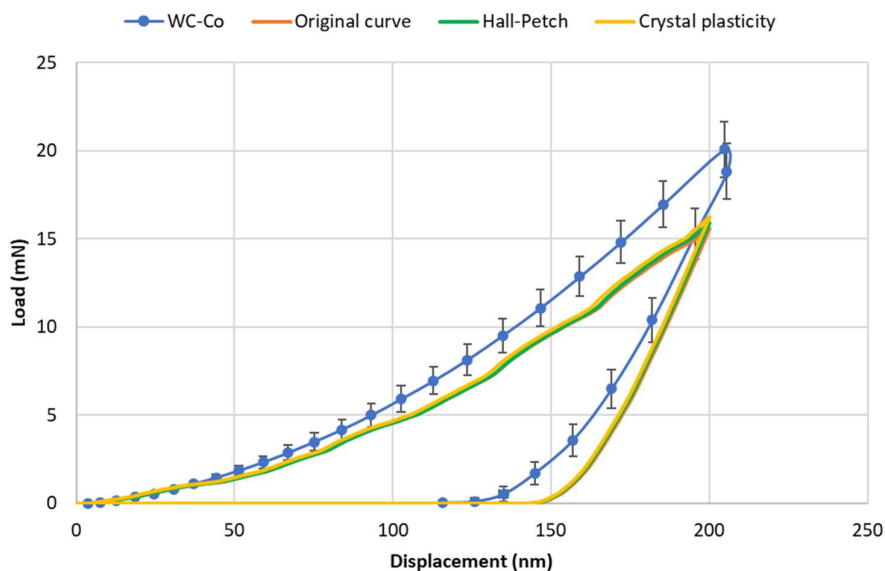
Figure 72. Comparison between experimental data and simulated curves.
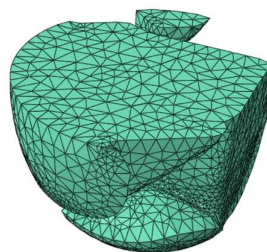
Figure 73. Tungsten carbide within the domain 'Lower_1_6'.

Figure 74 presents the hardness results simulated by means of the three plastic models: the original plastic curve, the modified one with the Hall-Petch model and the crystal plasticity also corrected with Hall-Petch. Firstly, samples get undoubtedly harder as the plastic model becomes more complex, namely by considering grain border strengthening or dislocation glide and subsequent entanglement. Furthermore, the percentual differences between the models are shown with three lines. It is clear that the hardest domains present little variations that are below 10%, whereas the softer ones differ more than 120% when comparing the crystal plasticity to the original plastic curve. However, the impact is much lower when the data between the Hall-Petch-

modified curve and the crystal plasticity model are contrasted, since the differences are not higher than 30% and normally oscillate around 20%.
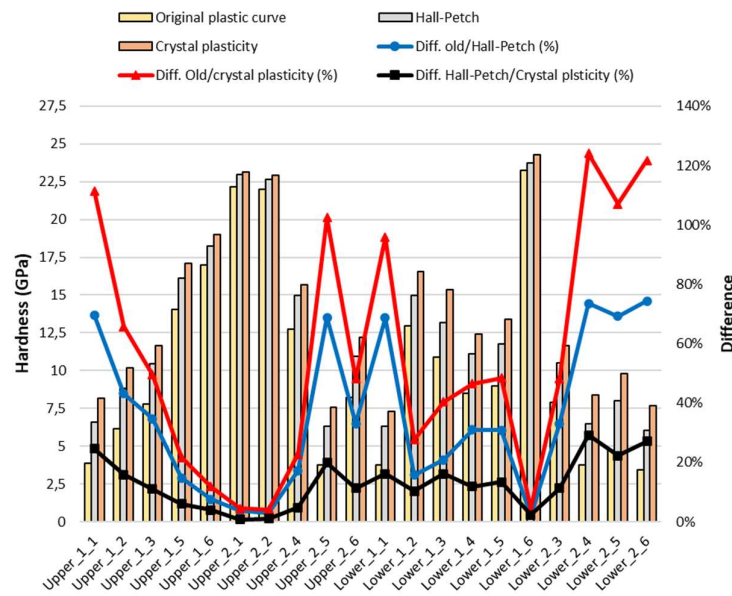
Figure 74. Comparison between the hardness values resulting from the different plasticity models.

A similar analysis was performed with the elastic modulus data attained using the three plasticity models, as presented in Figure 75. As expected, the differences are noticeably lower compared to hardness results. In addition, the greatest variations occurred in softer domains, which is coherent as explained above. However, there is not a clear trend in the evolution of the Young's moduli with the plastic models. For instance, there are samples like 'Lower_1_1', where the crystal plasticity output is higher than the others, but there are also samples where the opposite effect is appreciated (see domain 'Lower_1_4').

Lastly, the relative error considering R-squared criteria of 0.98 and 0.99 were contrasted for every sample and plastic model. The graphics involved in this analysis are shown in Figure 76. Hardness errors lay well below 10% regardless the model and R-squared criteria. Given that the error is obtained from the contact stiffness and then propagated to the calculated magnitudes, it is reasonable that the error in the hardness value is low, as the contact stiffness has an indirect effect on the calculus of hardness. Meanwhile, the errors in the elastic moduli are slightly higher, reaching a peak of 12%. In both magnitudes, the use of an R-squared criterium of 0.98 results in higher errors, which is also sensible due to the larger error magnitude associated to the slope of the linear fitting, i.e. the contact stiffness. Moreover, the error tends to be reduced the more complex the plasticity model becomes, although there some minor exceptions.

UNIVERSITAT POLITÈCNICA DE CATALUNYA
BARCELONA**TECH**
Escola d'Enginyeria de Barcelona Est
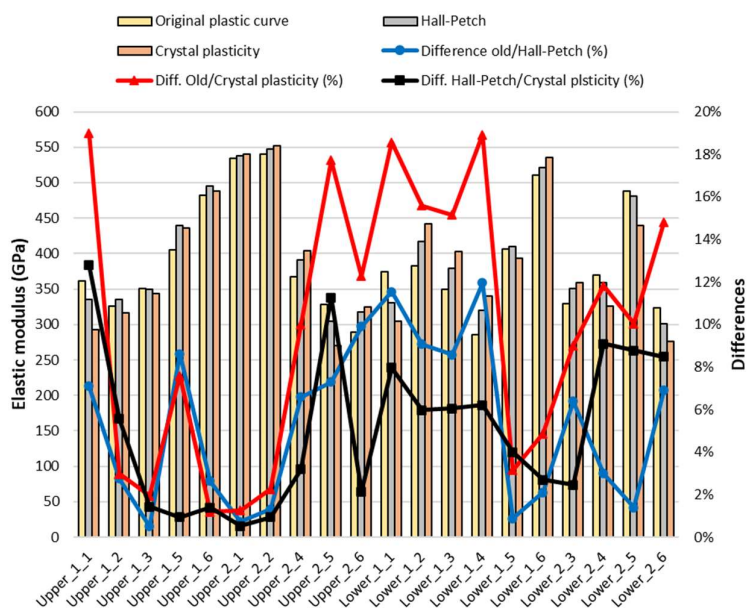
Figure 75. Comparison between the Young's moduli obtained with the different plasticity models.
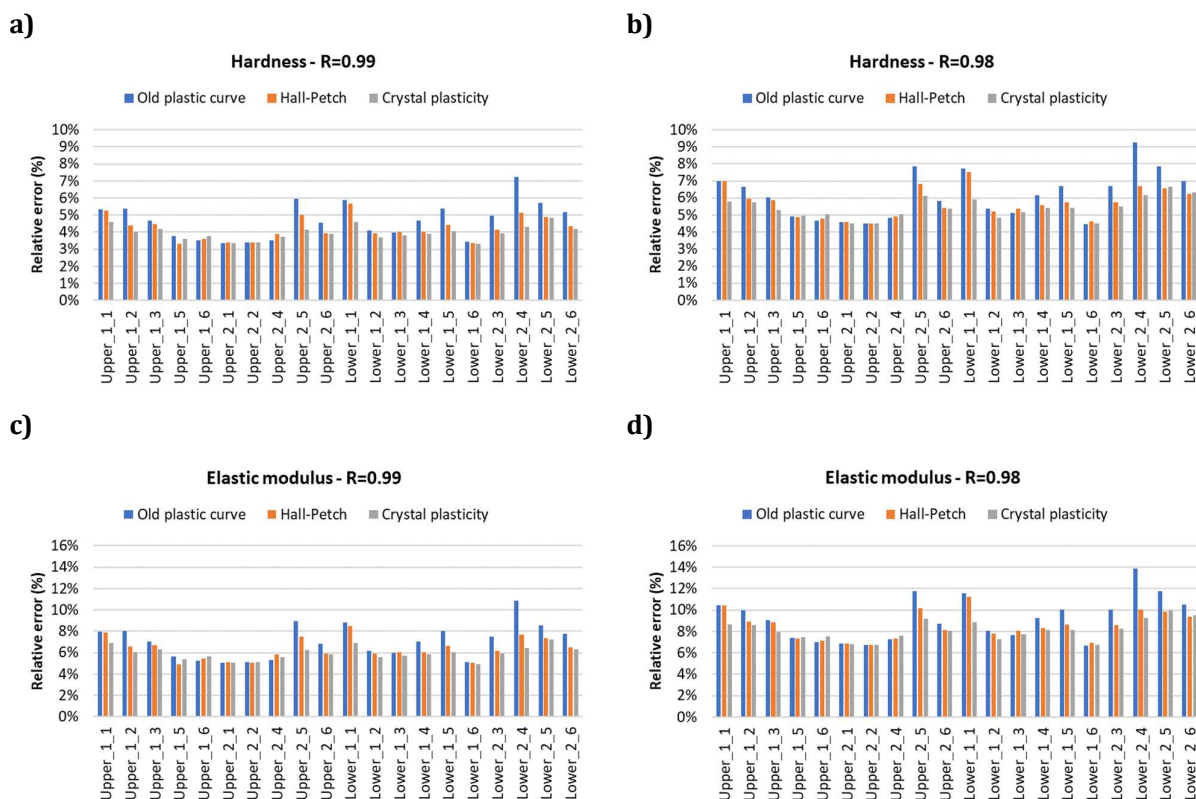
Figure 76. Hardness and Young's modulus error analysis for the domains considering different plastic models and two R-squared criteria.

To conclude, the use of a crystal plasticity model has resulted in higher hardness values and a consequent distribution that is more similar to the one experimentally found. However, a greater number of simulations should be performed in order to confirm and enhance the trend. In addition, the elastic moduli found are within the expected range and the crystal plasticity model does not changes this range, despite changing the distribution to a very limited extent. The errors within the three plasticity models are well within engineering range (less than 15%) and there is a tendency towards error reduction when the model becomes harder. All in all, the developed model can successfully sustain a complex model as the crystal plasticity one, plus yielding more reliable results.

UNIVERSITAT POLITÈCNICA DE CATALUNYA
BARCELONATECH
Escola d'Enginyeria de Barcelona Est

Conclusion

Nanoindentation tests on hardmetals were replicated in a numerical model within a commercial software for finite element analysis. What is more, it was possible to simulate the indentation of a real microstructure obtained from a tomography. No such accomplishments have been found in current literature, as artificial microstructures consisting in the extrusion of 2D images are usually used.[48], [49] Moreover, plastic deformation has been considered in the tungsten carbide phase, which is also novel as it is common practice to consider it an elastic material.

Different material models have been used to model the plastic behavior of the binder phase. It has been thus proved that this choice plays a major role in the results and their accuracy when compared to experimental data. In fact, using a material model that does not account for Hall-Petch effect within the cobalt has led to poorer results. Hence, the theory that this hardening effect is actually happening in reality is hereby supported. Another interesting aspect of the project was the use of a complex plasticity model that accounts for dislocation motion and entanglement, which in fact has yielded the output that best fits the experimental data.

The simulation of nanoindentation was developed following a cautious step-by-step procedure. Such wariness owed to the fact that the model should ultimately sustain complex microstructures, so there should not be any doubt concerning fundamental aspects like contact or boundary effects. Indeed, the latter feature presented problems at an intermediate stage of the project, although it was successfully identified and overcome. Moreover, tripping over boundary effects has in fact shown that there is some stiffening associated with it, which casts some doubts on how proper it is to model the carbide influence on the binder phase with a boundary condition.[36]

Unsuccessful attempts to indent right over the whole meshed tomography were performed. In spite of the fact that other simulations have been done on such a system,[14] nanoindentation was never studied in such a configuration. Simulating this test results in complex geometrical issues that may hinder the convergence to a solution, especially in the case of a Berkovich indenter. This is why conic tips with equivalent surface are normally used in literature for modeling indentation. Therefore, the fruitful usage of the Berkovich indenter in the present work is a positive outcome that may go unnoticed, as it is in itself a singularity in the Art. Furthermore, the approach of cutting tomography domains and their subsequent embedment in a larger matrix is also a strategy that might be of good use in the future.

There are some improvements that could be done to the material models used in this project. For example, the use of plastic curves is discouraged when the strains exceed the data range, as

UNIVERSITAT POLITÈCNICA DE CATALUNYA
BARCELONA**TECH**
Escola d'Enginyeria de Barcelona Est

the software keeps the last value and uses it as an ideal elastoplastic. Therefore, the plastic curve could have been modeled with a Hollomon or Johnson-Cook approach which are supported by ABAQUS. The main advantage of using these models instead of a plastic curve is that it keeps the hardening effect beyond the experimental data range. Nevertheless, such effect would actually be an extrapolation which is also discouraged. As a consequence, the main improvement that could be done in the current project would be the introduction of damage. This approach would be the most realistic one, as it would imply that after the strain range data is surpassed the material would break. However, it was decided not to follow this method because of the restricted time-span to deliver this master final project. Hence, it is left as a recommendation for future projects in the area.

Despite having studied different material models in the binder phase within the real microstructure, there is still a lot to be done. More samples should be studied in order to enhance the material properties distributions, as only 24 have been studied (sometimes even less as there were a couple of non-converging models). Accomplishing this would require more tomographies, so that the excessive overlapping is avoided. Then, hardmetal microstructures with different carbide size could also be simulated. On the other hand, the successful use of the crystal plasticity model encourages the application of even more complex models.

To conclude, it was possible to simulate nanoindentation tests on a real three-dimensional microstructure. The numerical model was also developed and enhanced in many different ways, for example, by defining the sample and element size, the material models to be used, contact properties, etc. As for the model accuracy, its output was contrasted to experimental results, which has proved that the above-mentioned parameters are at least reasonable. Further improvements can be made, either by using more complex material models or by adding failure criteria. In addition, more simulations should be done on new tomographies, so that the statistical distributions are improved. All in all, the present project has shown what is possible and what is challenging, plus suggesting some lines of improvement for future work.

Project cost

The costs involved in the project are mainly related to the licenses of the software used, the equipment, i.e. the desktop computer and the personal and supervision time. A brief disclosure of the cost involved in the project is presented in Table 6. Notice that the computer cost is quite relevant (roughly 25% of the cost). This is because the simulations require high computational power, which translates into powerful processors and large internal memory and disk capacities.

Table 6. Project cost summary.

Item	Unit cost	Quantity	Subtotal
ABAQUS License	4.500 €	1	4.500 €
Avizo License	3.000 €	1	3.000 €
Equipment	6.000 €	1	6.000 €
Supervision	100 €/h	18	1.800 €
Own	30 €/h	750	22.500 €
		TOTAL	**37.800 €**

UNIVERSITAT POLITÈCNICA DE CATALUNYA
BARCELONA**TECH**
Escola d'Enginyeria de Barcelona Est

References

[1]   L. Prakash and K. U. T. A. S, *Fundamentals and General Applications of Hardmetals*, vol. 1. Elsevier Ltd, 2014.

[2]   H. M. Ortner, P. Ettmayer, and H. Kolaska, "The history of the technological progress of hardmetals," *Int. J. Refract. Met. Hard Mater.*, vol. 44, pp. 148–159, 2014.

[3]   D. MacIsaac, G. Kanner, and G. Anderson, "Basic physics of the incandescent lamp (lightbulb)," *Phys. Teach.*, vol. 37, no. 9, pp. 520–525, 1999.

[4]   C. M. Fernandes and A. M. R. Senos, "Int . Journal of Refractory Metals and Hard Materials Cemented carbide phase diagrams : A review," *RMHM*, vol. 29, no. 4, pp. 405–418, 2011.

[5]   J. M. Tarragó, "Damage tolerance of cemented carbides under service-like conditions," Universitat Politècnica de Catalunya, 2016.

[6]   H. E. Exner, "Physical and chemical nature of cemented carbides," *Int. Met. Rev.*, vol. 24, no. 1, pp. 149–173, 1979.

[7]   T. W. Penrice, "Alternative Binders for Hard Metals," vol. 5, no. 1, pp. 35–39, 1987.

[8]   S. Lay, C. H. Allibert, M. Christensen, and G. Wahnstr, "Morphology of WC grains in WC – Co alloys," vol. 486, pp. 253–261, 2008.

[9]   A. Duszová and R. Halgaˇ, "Nanoindentation of WC – Co hardmetals," vol. 33, pp. 2227–2232, 2013.

[10]   B. Roebuck and E. A. Almond, "The Influence of Composition , Phase Transformation and Varying the Relative F . C . C . and H . C . P . Phase Contents on the Properties of Dilute Co-W-C Alloys," vol. 66, pp. 179–194, 1984.

[11]   J. M. Tarragó, D. Coureaux, Y. Torres, F. Wu, I. Al-dawery, and L. Llanes, "Int . Journal of Refractory Metals and Hard Materials Implementation of an effective time-saving two-stage methodology for microstructural characterization of cemented carbides," vol. 55, pp. 80–86, 2016.

[12]   V. K. Sarin and T. Johannesson, "On the Deformation of WC–Co Cemented Carbides," *Met. Sci.*, vol. 9, no. 1, pp. 472–476, 1975.

[13]   B. Roebuck and E. A. Almond, "Deformation and fracture processes and the physical metallurgy of WC-Co hardmetals," *Int. Mater. Rev.*, vol. 33, no. 1, pp. 90–112, 1988.

[14]   E. Jiménez-Piqué *et al.*, "Focused ion beam tomography of WC-Co cemented carbides," *Int. J. Refract. Met. Hard Mater.*, vol. 67, no. January, pp. 9–17, 2017.

[15]   J. García, V. C. Ciprés, A. Blomqvist, and B. Kaplan, "Cemented carbide microstructures : a review," *Int. J. Refract. Met. Hard Mater.*, vol. 80, no. December 2018, pp. 40–68, 2019.

[16]   V. Richter and M. V. Ruthendorf, "On hardness and toughness of ultrafine and

nanocrystalline hard materials," *Int. J. Refract. Met. Hard Mater.*, vol. 17, no. 1, pp. 141–152, 1999.

[17]   J. Bonneville and B. Escaig, "Cross-slipping process and the stress-orientation dependence in pure copper," *Acta Metall.*, vol. 27, no. 9, pp. 1477–1486, 1979.

[18]   J. J. Roa *et al.*, "Intrinsic hardness of constitutive phases in WC-Co composites: Nanoindentation testing, statistical analysis, WC crystal orientation effects and flow stress for the constrained metallic binder," *J. Eur. Ceram. Soc.*, vol. 35, no. 13, pp. 3419–3425, 2015.

[19]   J. J. Roa *et al.*, "Hall-Petch strengthening of the constrained metallic binder in WC–Co cemented carbides: Experimental assessment by means of massive nanoindentation and statistical analysis," *Mater. Sci. Eng. A*, vol. 676, pp. 487–491, 2016.

[20]   J. J. Roa, P. Sudharshan Phani, W. C. Oliver, and L. Llanes, "Mapping of mechanical properties at microstructural length scale in WC-Co cemented carbides: Assessment of hardness and elastic modulus by means of high speed massive nanoindentation and statistical analysis," *Int. J. Refract. Met. Hard Mater.*, vol. 75, no. April, pp. 211–217, 2018.

[21]   W. C. Oliver and G. M. Pharr, "Nanoindentation in materials research: Past, present, and future," *MRS Bull.*, vol. 35, no. 11, pp. 897–907, 2010.

[22]   G. M. Pharr and W. C. Oliver, "Measurement of thin film mechanical properties using nanoindentation," *Mrs Bull.*, vol. 17, no. 7, pp. 28–33, 1992.

[23]   M. G. Gee, B. Roebuck, P. Lindahl, and H. Andren, "Constituent phase nanoindentation of WC / Co and Ti (C , N) hard metals," *Mater. Sci. Eng. A*, vol. 209, pp. 128–136, 1996.

[24]   V. Bonache, E. Rayón, M. D. Salvador, and D. Busquets, "Nanoindentation study of WC-12Co hardmetals obtained from nanocrystalline powders: Evaluation of hardness and modulus on individual phases," *Mater. Sci. Eng. A*, vol. 527, no. 12, pp. 2935–2941, 2010.

[25]   N. Cuadrado, D. Casellas, L. Llanes, I. Gonzalez, and J. Caro, "Effect of crystal anisotropy on the mechanical properties of WC embedded in WC-Co cemented carbides," *Proceedings of the Euro International Powder Metallurgy Congress and Exhibition, Euro PM 2011*, vol. 1. 2011.

[26]   G. Möbus and B. J. Inkson, "Nanoscale tomography in materials science," *Mater. Today*, vol. 10, no. 12, pp. 18–25, 2007.

[27]   M. D. Uchic, L. Holzer, B. J. Inkson, E. L. Principe, and P. Munroe, "Three-Dimensional Beam Tomography," *MRS Bull.*, vol. 32, no. May, pp. 408–416, 2007.

[28]   D. N. Dunn, A. J. Kubis, and R. Hull, "Quantitative three-dimensional analysis using Focused Ion Beam microscopy," in *Introduction to Focused Ion Beams*, Boston: Springer US, 2005, pp. 281–302.

[29]   R. W. Clough, "Finite Element Method After Twenty-Five Years - a Personal View.," *IEE Conf. Publ.*, vol. 1, 1979.

[30]   M. Turner, R. Clough, H. Martin, and J. Topp, "Stiffness and deflection analysis of comlex

UNIVERSITAT POLITÈCNICA DE CATALUNYA
BARCELONA**TECH**
Escola d'Enginyeria de Barcelona Est

strucutres," *J. Aeronaut. Sci.*, no. 23, pp. 805–23, 1956.

[31] J. Fish and T. Belytschko, *A first course in finite elements*, vol. 45, no. 06. John Wiley & Sons Inc., 2008.

[32] M. Lichinchi, C. Lenardi, J. Haupt, and R. Vitali, "Simulation of Berkovich nanoindentation experiments on thin films using finite element method," *Thin Solid Films*, vol. 312, no. 1–2, pp. 240–248, 1998.

[33] N. A. Sakharova, J. V. Fernandes, J. M. Antunes, and M. C. Oliveira, "Comparison between Berkovich, Vickers and conical indentation tests: A three-dimensional numerical simulation study," *Int. J. Solids Struct.*, vol. 46, no. 5, pp. 1095–1104, 2009.

[34] T. Csanádi, D. Németh, and F. Lofaj, "Mechanical Properties of Hard W-C Coating on Steel Substrate Deduced from Nanoindentation and Finite Element Modeling," *Exp. Mech.*, vol. 57, no. 7, pp. 1057–1069, 2017.

[35] H. Debski and T. Sadowski, "Modelling of the damage process of interfaces inside the WC/Co composite microstructure: 2-D versus 3-D modelling technique," *Compos. Struct.*, vol. 159, pp. 121–127, 2017.

[36] D. Linder, M. Walbrühl, J. Agren, and A. Borgenstam, "International Journal of Solids and Structures Indentation behavior of highly confined elasto-plastic materials," vol. 194, pp. 69–78, 2020.

[37] I. Borgh *et al.*, "On the three-dimensional structure of WC grains in cemented carbides," vol. 61, pp. 4726–4733, 2013.

[38] J. A. Knapp, D. M. Follstaedt, S. M. Myers, J. C. Barbour, and T. A. Friedmann, "Finite-element modeling of nanoindentation," *J. Appl. Phys.*, vol. 85, no. 3, pp. 1460–1474, 1999.

[39] D. E. Vlachos, Y. P. Markopoulos, and V. Kostopoulos, "3-D modeling of nanoindentation experiment on a coating-substrate system," *Comput. Mech.*, vol. 27, no. 2, pp. 138–144, 2001.

[40] Y. Liu, B. Wang, M. Yoshino, S. Roy, H. Lu, and R. Komanduri, "Combined numerical simulation and nanoindentation for determining mechanical properties of single crystal copper at mesoscale," *J. Mech. Phys. Solids*, vol. 53, no. 12, pp. 2718–2741, 2005.

[41] M. Karimpour, D. S. Balint, K. A. Rzepiejewska-Malyska, A. Szerling, J. Michler, and J. Lin, "An inverse method for extracting the mechanical properties of the constituent materials of a multilayer from nanoindentation data," *Comput. Mater. Sci.*, vol. 68, pp. 384–390, 2013.

[42] M. Liu, C. Lu, K. A. Tieu, C. T. Peng, and C. Kong, "A combined experimental-numerical approach for determining mechanical properties of aluminum subjects to nanoindentation," *Sci. Rep.*, vol. 5, no. August, pp. 1–16, 2015.

[43] G. Marchiori *et al.*, "Optimizing thickness of ceramic coatings on plastic components for orthopedic applications: A finite element analysis," *Mater. Sci. Eng. C*, vol. 58, pp. 381–388, 2016.

[44]   S. Rezaei *et al.*, "A novel approach for the prediction of deformation and fracture in hard coatings: Comparison of numerical modeling and nanoindentation tests," *Mech. Mater.*, vol. 117, no. July 2017, pp. 192–201, 2018.

[45]   E. B. Marin, "On the Formulation of a Crystal Plasticity Model," 2006.

[46]   A. Karimzadeh, S. S. R. Koloor, M. R. Ayatollahi, A. R. Bushroa, and M. Y. Yahya, "Assessment of Nano-Indentation Method in Mechanical Characterization of Heterogeneous Nanocomposite Materials Using Experimental and Computational Approaches," *Sci. Rep.*, vol. 9, no. 1, pp. 1–14, 2019.

[47]   E2546-07, "Standard Practice for Instrumented Indentation Testing," *ASTM B. Stand.*, vol. 1, no. December, pp. 1–23, 2007.

[48]   U. A. Ozden, K. Jiang, A. Bezold, and C. Broeckmann, "Mesoscale simulation of fatigue crack propagation in artificial WC-Co microstructures," *World PM 2016 Congr. Exhib.*, 2016.

[49]   A. Tahir *et al.*, "Improving WC-Co coating adhesive strength on rough substrate: Finite element modeling and experiment," *J. Mater. Sci. Technol.*, vol. 37, pp. 1–8, 2020.

Annex A

A1. Matlab script and functions

Script for homogeneous materials:

```
clc
clear all
home_dir = pwd;
num_files = 2;
file_name = 'P_vs_U.rpt';
E = zeros(num_files,1);
H = zeros(num_files,1);
for i=1:num_files
switch i
  case 1
    folder_name = ['Co'];
    v = 0.3;    %coeficiente de Poisson del material
    model_name = 'Co';
  case 2
    folder_name = ['WC'];
    v = 0.2;    %coeficiente de Poisson del material
    model_name = 'WC';
end
  cd(folder_name);
%    file_name = ['P vs U',num2str(i),'.rpt'];
  [Displacement,Force] = textread(file_name,'%f %f','headerlines',3);
  cd(home_dir);
  [E(i) , H(i)] = function_Nano_properties(Force,Displacement,v);
%    Plotting
  p(i) = plot(Displacement,Force/1000000,'DisplayName',model_name,'LineWidth',2);
  hold on
  xlabel('Depth(nm)','FontSize',18,'FontWeight','bold');
  ylabel('Load (mN)','FontSize',18,'FontWeight','bold');
  max_displacement (i) = max(Displacement);
  max_force (i) = max(Force);
  clear Force Displacement
end

cd(home_dir);
grid on
legend ('FontSize',16)
set(gca,'fontsize',16)

figure

% for i=1:num_files
```

```matlab
%    yyaxis left
%    y1 = E(i);
%    x = max_displacement(i);
%    o(i) = plot(x,y1,'o');
%    ylabel('Elastic modulus (GPa)','FontSize',18,'FontWeight','bold');
%    yyaxis right
%    y2 = H(i);
%    q(i) = plot(x,y2,'p');
%    ylabel('Hardness (GPa)','FontSize',18,'FontWeight','bold');
%
%    xlabel('Maximum depth(nm)','FontSize',18,'FontWeight','bold');
%    title('Material properties at different depths')
%    hold on
%    cd(home_dir);
% end

tiledlayout(2,1)
x = categorical({'Co','WC'});
% Top bar graph
ax1 = nexttile;
y1 = E;
b=bar(x,y1);
b.FaceColor = 'flat';
b.CData(2,:) = [0.8500 0.3250 0.0980];
ylabel('Elastic modulus (GPa)','FontSize',18,'FontWeight','bold');
xlabel('Materials','FontSize',18,'FontWeight','bold');
title('Elastic Moduli for different materials')
hold on

% Bottom bar graph
ax2 = nexttile;
y2 = H;
c=bar(x,y2);
c.FaceColor = 'flat';
c.CData(2,:) = [0.8500 0.3250 0.0980];
ylabel('Hardness (GPa)','FontSize',18,'FontWeight','bold');
xlabel('Materials','FontSize',18,'FontWeight','bold');
title('Hardness for different materials')

hold on
cd(home_dir);
```

Script for tomography domains:

```matlab
clc
clear all
home_dir = pwd;
num_files = 24;
file_name = 'P_vs_U.rpt';
```

```
E = zeros(num_files,1); H = zeros(num_files,1); S = zeros(num_files,1); R = zeros(num_files,1);
dE = zeros(num_files,1); dH = zeros(num_files,1);
max_displacement = zeros(num_files,1); max_force = zeros(num_files,1);

v = 0.25; %Coeficiente de Poisson del COMPOSITE
k = 1;
%Opens Upper face data
for i=1:2
    for j=1:6
        folder_name = ['\Upper-face_',num2str(i),'_',num2str(j)];
        model_name = ['Upper_',num2str(i),'_',num2str(j)];
        temp_dir = [home_dir,'\Upper_side',folder_name];
        cd(temp_dir);
        [Displacement,Force] = textread(file_name,'%f %f','headerlines',3);
        cd(home_dir);
        [E(k) , H(k), S(k) , R(k) , dE(k) , dH(k)] = function_Nano_properties(Force,Displacement,v);
        %   Plotting
        p(k) = plot(Displacement,Force/1000000000,'DisplayName',model_name,'LineWidth',2);
        hold on
        xlabel('Depth(nm)','FontSize',16,'FontWeight','bold');
        ylabel('Load (mN)','FontSize',16,'FontWeight','bold');
        xlim([0 800]);
        title('Nanoindentation on WC particle embedded in cobalt at different
depths','FontSize',24,'FontWeight','bold')
        max_displacement (k,1) = max(Displacement);
        max_force (k,1) = max(Force);
        clear Force Displacement
        k = k+1;
    end
end

cd(home_dir);
grid on
legend ('FontSize',16)
set(gca,'fontsize',16)

figure

for i=1:2
    for j=1:6
        folder_name = ['\Lower-face_',num2str(i),'_',num2str(j)];
        model_name = ['Lower_',num2str(i),'_',num2str(j)];
        temp_dir = [home_dir,'\Lower_side',folder_name];
        cd(temp_dir);
        [Displacement,Force] = textread(file_name,'%f %f','headerlines',3);
        cd(home_dir);
        [E(k) , H(k), S(k) , R(k) , dE(k) , dH(k)] = function_Nano_properties(Force,Displacement,v);
        %   Plotting
```

```
    p(k) = plot(Displacement,Force/1000000000,'DisplayName',model_name,'LineWidth',2);
    hold on
    xlabel('Depth(nm)','FontSize',16,'FontWeight','bold');
    ylabel('Load (mN)','FontSize',16,'FontWeight','bold');
    xlim([0 800]);
    title('Nanoindentation    on    WC    particle    embedded    in    cobalt    at    different
depths','FontSize',24,'FontWeight','bold')
    max_displacement (k,1) = max(Displacement);
    max_force (k,1) = max(Force);
    clear Force Displacement
    k=k+1;
  end
end

figure

% yyaxis left
% y1 = E;
% x = max_displacement;
% o = plot(x,y1,'-o','MarkerEdgeColor','#0072BD','MarkerFaceColor','#0072BD');
o                                                                              =
errorbar(max_displacement,E,dE,'Marker','o','MarkerFaceColor','#D95319','MarkerEdgeColor','#
D95319','Color','#D95319','LineWidth',2);
title('Elastic    modulus    of    WC    particle    embedded    in    cobalt    matrix    at    different
depths','FontSize',24,'FontWeight','bold');
ylabel('Elastic modulus (GPa)','FontSize',16,'FontWeight','bold');
xlabel('Maximum depth(nm)','FontSize',16,'FontWeight','bold');
ylim([0 800]);
xlim([0 800]);
hold on
grid on

figure

% yyaxis right
% y2 = H;
% q = plot(x,y2,'-s','MarkerEdgeColor','#D95319','MarkerFaceColor','#D95319');
q                                                                              =
errorbar(max_displacement,H,dH,'Marker','s','MarkerFaceColor','#D95319','MarkerEdgeColor','#
D95319','Color','#D95319','LineWidth',2);
ylabel('Hardness (GPa)','FontSize',16,'FontWeight','bold');
xlabel('Maximum depth(nm)','FontSize',16,'FontWeight','bold');
title('Hardness    of    WC    particle    embedded    in    cobalt    matrix    at    different
depths','FontSize',24,'FontWeight','bold');
ylim([0 35]);
xlim([0 800]);
set(gca,'fontsize',16)
grid on
```

UNIVERSITAT POLITÈCNICA DE CATALUNYA
BARCELONATECH
Escola d'Enginyeria de Barcelona Est

82

```
hold on
cd(home_dir);
```

Function 'Nano_properties':

```
function [E , H , S , Rf , DE , DH] = function_Nano_properties (P , U ,nu)
% E es el módulo elástico H es la dureza
% P is the load vector and U is the displacement one in pN and nm respectively
% nu is the Poisson's coeficient of the sample under study
[max_value,index] = max(P(:));
j = 1;
for i=index:length(P)
    Linear_x (j) = U(i);
    Linear_y(j) = P(i);
    j = j+1;
end
mdl = fitlm(Linear_x,Linear_y);
R0 = mdl.Rsquared.Ordinary;
while R0<=0.99
    Linear_x(end) = [];
    Linear_y(end) = [];
    mdl = fitlm(Linear_x,Linear_y);
    R0 = mdl.Rsquared.Ordinary;
end
Rf = R0;

S = mdl.Coefficients{2,1}/1000; %Unloading stiffness in N/m
DS = mdl.Coefficients{2,2}/1000; %Dispersion in the S value; [DS]= N/m
SRel = DS/S; %Relative error

hc = U(index) - 0.75* max_value/(S*1000);%[hc] = nm
hcRel = SRel;

A = 24.5 * (hc / 1e9)^2; %Contact area in m2
ARel = 2 * hcRel;

Eff = sqrt(pi)*S/(2 * sqrt(A)); %[Eff] = Pa
EffRel = SRel + ARel;  %[EffRel] = Pa

E = (((1000000000 / Eff)-((1-0.07^2)/1140))^(-1))*(1-nu^2); %[E] = GPa
DE = EffRel * E;  %Dispersion in the E value in GPa

H = (max_value/A)/(1000000000*1000000000000);  %[H] = GPa
DH = H*ARel;    %Dispersion in the H value in GPa
end
```